

INFORMATION TO USERS

This manuscript has been reproduced from the microfilm master. UMI films the text directly from the original or copy submitted. Thus, some thesis and dissertation copies are in typewriter face, while others may be from any type of computer printer.

The quality of this reproduction is dependent upon the quality of the copy submitted. Broken or indistinct print, colored or poor quality illustrations and photographs, print bleedthrough, substandard margins, and improper alignment can adversely affect reproduction.

In the unlikely event that the author did not send UMI a complete manuscript and there are missing pages, these will be noted. Also, if unauthorized copyright material had to be removed, a note will indicate the deletion.

Oversize materials (e.g., maps, drawings, charts) are reproduced by sectioning the original, beginning at the upper left-hand corner and continuing from left to right in equal sections with small overlaps. Each original is also photographed in one exposure and is included in reduced form at the back of the book.

Photographs included in the original manuscript have been reproduced xerographically in this copy. Higher quality 6" x 9" black and white photographic prints are available for any photographs or illustrations appearing in this copy for an additional charge. Contact UMI directly to order.

U·M·I

University Microfilms International
A Bell & Howell Information Company
300 North Zeeb Road, Ann Arbor, MI 48106-1346 USA
313/761-4700 800/521-0600

Order Number 1355277

**The selection and synthesis of a coating for the stabilization of
water splitting photoelectrodes**

Uslu, Canan, M.S.

Rice University, 1993

Copyright ©1993 by Uslu, Canan. All rights reserved.

U·M·I
300 N. Zeeb Rd.
Ann Arbor, MI 48106

RICE UNIVERSITY

**The Selection and Synthesis of A Coating For The
Stabilization of Water Splitting Photoelectrodes**

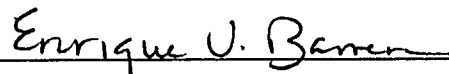
by

Canan Uslu

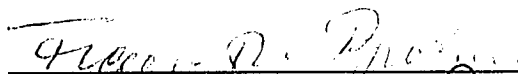
A THESIS SUBMITTED
IN PARTIAL FULFILLMENT OF THE
REQUIREMENTS FOR THE DEGREE

Master of Science

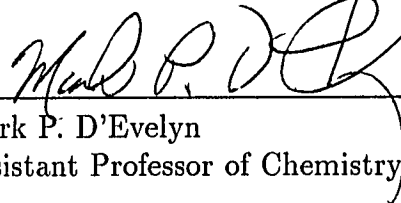
APPROVED, THESIS COMMITTEE:



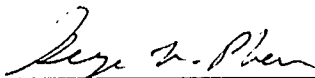
Enrique V. Barrera, Chairman
Assistant Professor of Materials Science



Franz R. Brotzen
Professor Emeritus of Materials Science



Mark P. D'Evelyn
Assistant Professor of Chemistry



George M. Pharr
Professor of Materials Science

Houston, Texas

April, 1993

Copyright

by

Canan Uslu

1993

The Selection and Synthesis of A Coating For The Stabilization of Water Splitting Photoelectrodes

Canan Uslu

Abstract

The objective of this work was to select and process an electrically insulating thin film suitable for the photoelectrodes used in solar to chemical energy conversion where the current flow would occur by quantum tunneling. A number of aluminum oxide coatings with various processing parameters were deposited onto silicon to explore the relationships between the deposition variables and the performance of the electrodes in 1 N H_2SO_4 aqueous solution subjected to visible light. Optical, surface topographical and chemical information was combined with the photoelectrochemical (PEC) evaluations.

The oxide thin films deposited by ultra high vacuum (UHV) reactive evaporation technique possessed 70 - 90% transmittance in UV-visible light range (190-800 nm). Their optical transmittance (τ) and the open-circuit photopotentials (V_{oc}) were found to depend on the deposition variables. The film growth on single crystal Si occurred from initially oriented islands and clusters, to a coalesced amorphous film as the atomic coverage increased. The surface compositions and depth profiles showed clean and uniform films. It was found that the oxide films can improve the open-circuit photovoltage of silicon and also act as anti-reflection (AR) coatings on Si. The photocurrent in the cell was obtained by quantum tunneling as it increased with the applied potential. It is observed that the photocurrent peak occurs at a potential which is eleven times higher than that for uncoated Si.

TO MY PARENTS

Acknowledgments

This work was completed with the help of many people whose help, guidance and support I gratefully acknowledge. I would like to thank Hakim Bensaoula who provided very valuable experience with surface spectroscopies at the Space Vacuum Epitaxy Center, University of Houston.

I am indebted to Dr. Leyla Conrad, who took the time to lead me through my first steps in UHV systems.

I also express my cordial thanks to Dr. Abdelhak Bensaoula, Dr. Paul Ingles, Dr. Naomi Halas and Dr. Norman Hackerman for using their equipment.

My thanks also go to my advisor, Dr. Barrera, for his help and his confidence in my ability to successfully complete this project and also to Dr. Brotzen, Dr. Pharr and Dr. D'Evelyn for serving in my thesis committee.

I also wish to take this opportunity to thank Dr. Yildiz Bayazitoglu for her encouragement and valuable ideas in life and education.

My hearty thanks go to Robin Rawles for her help in obtaining the SEM micrographs. I would also like to acknowledge the many individuals who sincerely shared their technical experiences with me, especially, Dr. Alfred Griffin, Dr. Margot Wasz, Sandra Hernandez, Dr. Daniel Callahan, Bruce Brinson, Dr. Milan Bartos, John Sims, Wayne Howell and Joe Gesenhues.

Finally my special thanks are for Ted Hardwicke for sharing many of those ups and downs with continuous support and encouragement, and most of all making life more meaningful than ever.

Contents

Abstract	iii
Acknowledgments	v
List of Illustrations	viii
List of Tables	xii
1 Introduction	1
2 Theoretical Background	3
2.1 The Mechanism of the Photoelectrochemical Process	3
2.2 Energy Level Diagram of a PEC Cell	9
2.3 Materials Aspects of PEC Cells	13
2.3.1 Semiconductor Material Requirements for the PEC Cells . . .	13
2.3.2 Protective Coatings For the PEC Cells	16
3 Thesis Proposal	21
3.1 A Review on the Protective Coatings	21
3.2 Proposed Electrode Model	23
3.2.1 Absorption and Transmission Properties	24
3.2.2 Electrical Conduction in Insulating Films	29
3.2.3 Long Term Stability of the Oxides	34
3.2.4 Chemical Analysis of the Surface Films	37
3.2.5 Summary	57
4 Experimental Considerations	58

4.1	Anode Preparation	58
4.1.1	Reactive Evaporation Technique	60
4.1.2	System Description	62
4.1.3	Coating Process	66
4.2	Surface Morphology	68
4.3	Optical Measurements	71
4.4	Surface Chemical Analysis	72
4.5	PEC Measurements	74
5	Results And Discussions	79
5.1	Transmission Spectra of the Model Electrodes	79
5.2	Surface Morphology of the Semiconductor Electrodes	86
5.3	Surface Chemistry of the Electrodes	93
5.4	PEC Measurements	105
5.4.1	Photopotentials in the Cell	105
5.4.2	Photoactivity of the Electrodes	112
5.4.3	Long Term Stability of the Electrodes	121
5.5	Summary of the Results	124
6	Conclusions	127
A	Deposition Configuration	129
B	AES Depth Profiles	130
B.1	Al-oxide film on sample 6	130
B.2	Al-oxide film on sample 8	131
	Bibliography	132

Illustrations

2.1	A photoelectrolysis cell.	3
2.2	The energy relations within a semiconductor placed in a solution containing three electrolytes.	4
2.3	Double layers at the n-type semiconductor (solid)/liquid interface for a very dilute solution.	5
2.4	The effects of illumination on an n-type semiconductor in a redox electrolyte.	7
2.5	The minimum conditions for water decomposition with zero potential application.	8
2.6	CB, VB energies and E_g values of several semiconductors.	9
2.7	Energy level diagram for a photoelectrolysis cell.	11
2.8	Possible positions of the decomposition energy levels relative to the band edges.	15
2.9	Properties of an ideal photoelectrode system, in terms of surface, bulk coating and interfacial properties.	18
3.1	Optical absorption constant, α , as a function of photon energy.	25
3.2	Spectral distribution curves related to the sun.	26
3.3	Transmission regions of special crystals and certain glasses.	27
3.4	The model electrode for optical transmission measurements.	28
3.5	The band model for an amorphous insulating layer over a semiconductor.	30

3.6	Comparison of the derivative spectra $dN(E)/dE$ for 3 keV electrons incident on a) oxidized Al, b) pure Al samples.	41
3.7	The process of Auger electron generation.	42
3.8	Experimental apparatus used in Auger spectroscopy.	44
3.9	Electromagnetic spectrum indicating the region used for photoelectron spectroscopy.	48
3.10	The energy spectrum of electrons from Al_2O_3	49
3.11	Schematic of the relevant energy levels for binding energy measurements.	51
3.12	Schematic of the basic apparatus used in XPS.	52
3.13	Schematic of a double pass cylindrical mirror analyzer used in photoelectron spectroscopy.	53
3.14	Al(2p) chemical shift in Al_2O_3 with respect to pure Al.	54
4.1	Al-Si phase diagram.	59
4.2	UHV chamber designed and built for the reactive evaporation process.	63
4.3	The apparatus for holding and resistively heating the substrates.	64
4.4	Oxygen leak manifold for reactive evaporation.	65
4.5	Schematic diagram of a diode-array spectrometer.	71
4.6	The holder for the photoelectrodes.	75
4.7	Experimental configuration for the PEC measurements.	77
4.8	The photoelectrolysis cell to study the performance of the coatings in an illuminated aqueous solution.	78
5.1	UV-visible transmittance of reactively evaporated Al-oxide coatings on glass slides- type 1.	80
5.2	UV-visible transmittance of reactively evaporated Al-oxide coatings on glass slides- type 2.	81

5.3	UV-visible transmittance of reactively evaporated Al-oxide thin films.	82
5.4	Dependence of the optical transmittance at 500 nm on the four main independent deposition parameters.	85
5.5	The first stages of the Al-oxide growth on an n-Si(111) surface, a) from the center, b) from the edge.	87
5.6	Two different morphologies magnified from the previous figure.	88
5.7	SEM micrograph of a 100 Å thick oxide film.	89
5.8	Structural dependence of the films on oxygen concentration.	91
5.9	SEM micrograph of a 510 Å thick oxide film.	92
5.10	Auger electron spectrum taken in-situ.	93
5.11	Auger electron spectrum taken ex-situ.	94
5.12	Auger electron depth profile (405 Å oxide on n-Si(111)).	96
5.13	Relative film composition as a function of depth.	96
5.14	Stoichiometry of the film as a function of depth.	97
5.15	A typical wide-scan XPS spectrum from the electrode surfaces.	98
5.16	Short-scan XPS spectrum of O(KLL) Auger emission from the oxide film surfaces.	99
5.17	Typical shape of Al(2p) peak from the samples analyzed.	103
5.18	Narrow scan XPS peak studied under 120 eV synchrotron radiation. .	104
5.19	Dark- and photo-corrosion potentials in the naked-n-Si(111)/1 N H_2SO_4 electrolyte system.	107
5.20	A typical photoresponse of an aluminum oxide coated p-type silicon PEC cell.	109
5.21	Dependence of photovoltage on the partial pressure of oxygen during film deposition.	110
5.22	Open circuit photopotentials as functions of the deposition parameters.	111
5.23	Current density vs electrode potential for an n-type "naked" silicon electrode in 1 N H_2SO_4 electrolyte.	112

5.24	The comparison of the photocurrent-voltage behavior of p-type electrodes under Xe illumination.	114
5.25	The photocurrent-voltage behavior of p-type electrodes under 632.8 nm illumination.	115
5.26	The effect of high oxygen pressure on the I-V behavior.	117
5.27	The effect of film thickness on the I-V behavior.	118
5.28	Photocurrent as a function of Al- oxide film thickness for n-type photoelectrodes.	120
5.29	Narrow scan spectrum after a cyclic voltammogram of 1 V limit. . . .	122
5.30	Potentiostatic oxidation photocurrent decay curve.	123

Tables

3.1	Chemical Analysis of Solids (Macrosamples- > 1 mg). Components: Major(> 5 %), Minor(0.1 to 5 %), Trace(< 0.1 %).	38
3.2	Surface Analysis of Solids	39
4.1	The Surface Cleaning Procedure Used For n-Si, p-Si Wafers	67
4.2	Samples Processed by the Reactive Evaporation Technique in UHV. .	69
5.1	Process Parameters and the Corresponding Optical Transmittance Values for the Model Electrodes	83
5.2	Stoichiometries Reported For Aluminum-Oxide.	95
5.3	Summary of XPS binding energies (in eV) from the oxide films. . . .	101
5.4	Photopotentials and photosensitivities achieved in the PEC cell containing 1 N H_2SO_4	106

Chapter 1

Introduction

Oil, natural gas and coal have fueled society and technology for many centuries. However, from an environmental and political viewpoint, these fuels are not the optimal sources. Hydrogen can be used as a clean and efficiently burning substitute for oil and other fossil fuels [54, 43], but presently, most hydrogen is produced by an hydrocarbon reaction (partial oxidation or steam reforming) [5] and electrolysis of water [14], both of which use expensive raw materials.

A third method of hydrogen production, suggested by Justi [38], in 1965, is the photoelectrolysis of water. This method is driven by the energy the earth's surface receives from the sun, an amount in the order of ca. 3×10^{24} Joules per year (or 10^4 times the world-wide yearly energy consumption [36]). Basically, a photoelectrochemical (PEC) cell is any device in which the irradiation of an electrode/electrolyte system produces a change in electrode potential if the circuit is open, or a change in the current flow if the circuit is closed. The effect can be due to irradiation of the electrode, the electrolytic solution or a photosensitive membrane in the solution. The term PEC in this work refers to a narrow-bandgap semiconductor/liquid electrolyte system.

Previous works suggest that a photoelectrode with an overall solar power conversion efficiency of around 10 % would provide a cost effective system for hydrogen production even in today's economy and even in 'nonsolar' areas [62, 29]. Even though the process seems to be simple to proceed, the major problem encountered in the PEC hydrogen production process is that the desirable semiconductor mate-

rials undergo a rapid photocorrosion and/or surface passivation when they are irradiated in aqueous solutions. This, of course, makes hole (or electron) conduction difficult and lowers the conversion efficiencies. Approaches to circumvent this problem of PEC corrosion focus on four major categories of materials [58]: a) the electrode materials themselves, b) protective coatings, c) catalysts, and d) electrolytes.

As a possible solution, various protective coatings have been deposited onto the light-harvesting semiconductor materials [58]. The long-term stability of the films, however, still remains a problem [12, 26, 34]. The experiments described in this thesis were carried out to provide some evidence on the use of aluminum oxide as a possible protective coating. The second chapter provides the theoretical background on the research of the PEC cell development. The guidelines used to achieve a thin coating with reasonable optical, chemical and electrical properties are given in the third chapter. The remainder of the thesis study will discuss the experimental procedures for the deposition of an inert layer on the semiconductor surface to inhibit electrolyte attack and the characterization of the surface and bulk properties of the electrodes for the use in photoelectrolysis.

Chapter 2

Theoretical Background

2.1 The Mechanism of the Photoelectrochemical Process

Figure 2.1 [28] shows the typical PEC cell for photoelectrolysis. Basically, the majority carrier flows through the electrical load to the metallic electrode and drives an electrochemical reaction. The minority carrier flows to the semiconductor surface driving another electrochemical reaction. Metals are often of limited usefulness in photoelectrochemical(PEC) cells because the charge carriers immediately cascade back down when they are photoexcited to a higher energy state. However, for semiconductors, electron transfer can only take place in the conduction band (CB) energy region; hole transfer can take place in the valence band (VB) energy region. Which of these processes will occur depends on the particular redox system in relation to the electrode material [37].

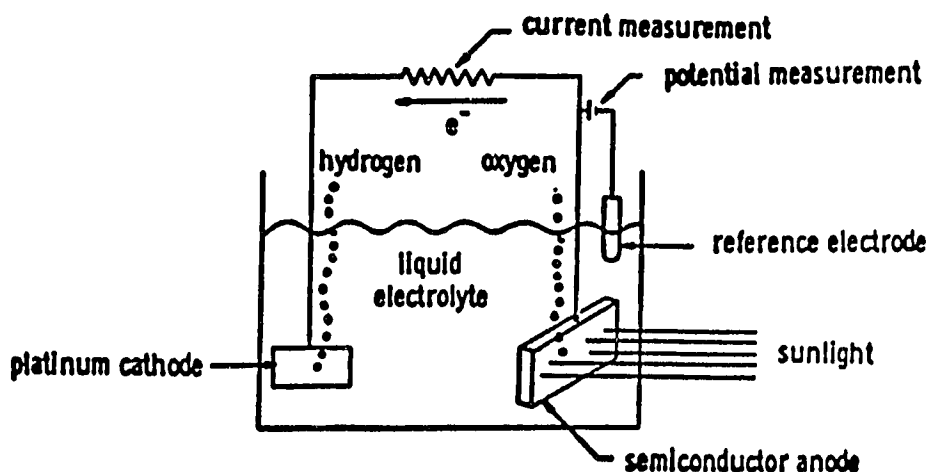


Figure 2.1: A photoelectrolysis cell.

Electron transfer can occur between two states, one empty and one filled, of similar energy. Figure 2.2 [37] indicates the relative position of the redox Fermi level (E_F) in relation to the CB (shown as E_c) and VB (shown as E_v) of a semiconductor.

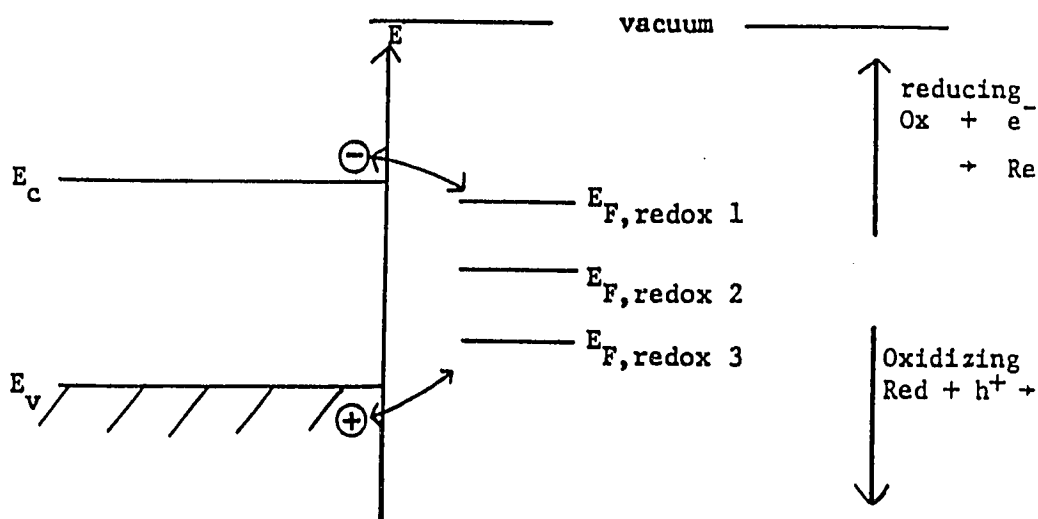


Figure 2.2: The energy relations within a semiconductor placed in a solution containing three electrolytes.

At equilibrium, the Fermi levels of holes and electrons within a material are equivalent. When such a semiconductor is placed in a redox solution; the chemical potential, E_F , of the semiconductor differs from that of the redox couple in solution E_{redox}^o (standard electrode potential). In order to re-establish equilibrium, a flow of charge occurs in the form of ion accumulation in the solution at the electrode and electron accumulation (p-type) or electron depletion (n-type) in the semiconductor. A strong local electric field results and the CB and VB bend. A high barrier to charge flow exists at the interface which may be considered as three capacitors (double layers) in series: the space-charge region within the semiconductor, the Helmholtz layer composed of adsorbed ions, and the solution diffuse double layer. In Figure 2.3 [49], the dashed line through the liquid indicates the variation in potential energy of a unit

negative charge, as determined only by the double layer voltages, as it moves from the CB of the solid into the solution. These double layers control the electrical and chemical properties of the interface.

Corresponding to these three double layers, there are four regions of excess charge. In the space charge region, the charge is in the form of uncompensated impurities or trapped holes or electrons, or possibly in the form of mobile holes or electrons very near the surface. Helmholtz double layer is formed by the charged planes on the two sides of the Helmholtz region. One plane is at the solid surface and the charge is in surface states or at the location of adsorbed ions. The other plane is called the "outer Helmholtz plane" (ohp) which is the position of closest approach of mobile ions. At the ohp, the charge arises from ions that drift up to the surface, attracted by the excess charge in or on the semiconductor. Gouy region, where the field near the surface separates the positive from the negative ions, is thought together with the

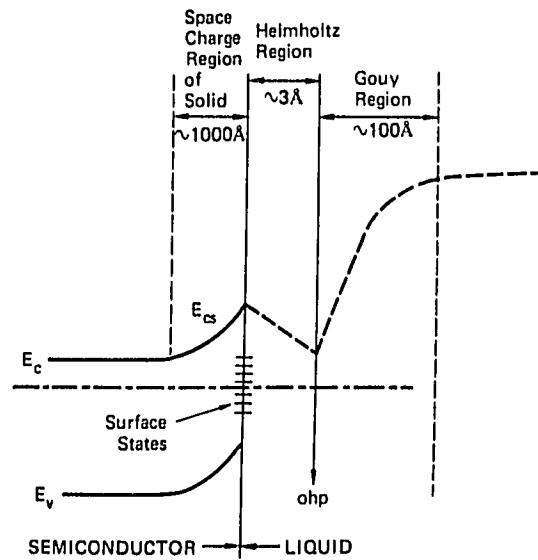


Figure 2.3: Double layers at the n-type semiconductor (solid)/liquid interface for a very dilute solution.

countercharge in the Helmholtz region and in the solid.

If a positive potential is applied to the n-type semiconductor in the solution, the Fermi level would be lowered further with respect to $E_{F,redox}$ and the band bending would increase; with a strong enough potential, tunneling from $E_{F,redox}$ into the CB may begin. If such a semiconductor (say, n-type) is illuminated with photons of energy greater than its band gap (E_g), electron-hole pairs are generated in the depletion layer. They are driven apart by the electric field at the interface. The excitons generated beyond the depletion layer are essentially lost through recombination. Therefore, the space charge region should extend farther into the bulk than the penetration depth of the light for the optimal operation. This charge separation process sets up a counter field which shifts the CB and VB up to E'_c and E'_v as shown in Figure 2.4(b) [37]. The field is at its maximum under open-circuit condition and it is called the open-circuit photovoltage ($V_{oc} = E'_F - E_F = E_{photo}$). If a counter electrode is immersed in the same solution, the photovoltage can drive a current which can perform electrolysis.

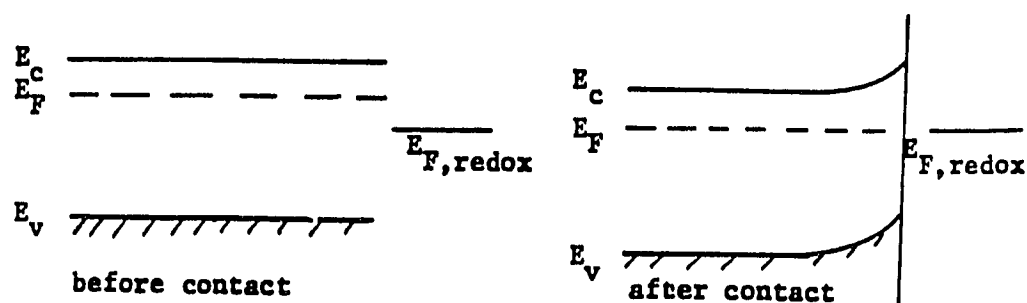
Illumination breaks the equilibrium distribution of holes and electrons and the Fermi levels for holes and electrons (E_{pF} and E_{nF} , respectively) are no longer coincident. The increase in the electron and hole concentrations (Δn and Δp , respectively) changes the chemical potentials for holes and electrons at the electrode under steady-state illumination by ΔE_{pF} and ΔE_{nF} , respectively. The new potentials which are called the quasi-Fermi energies are given by [37]:

$$E'_{nF} = E_{nF} + \Delta E_{nF} \quad (2.1)$$

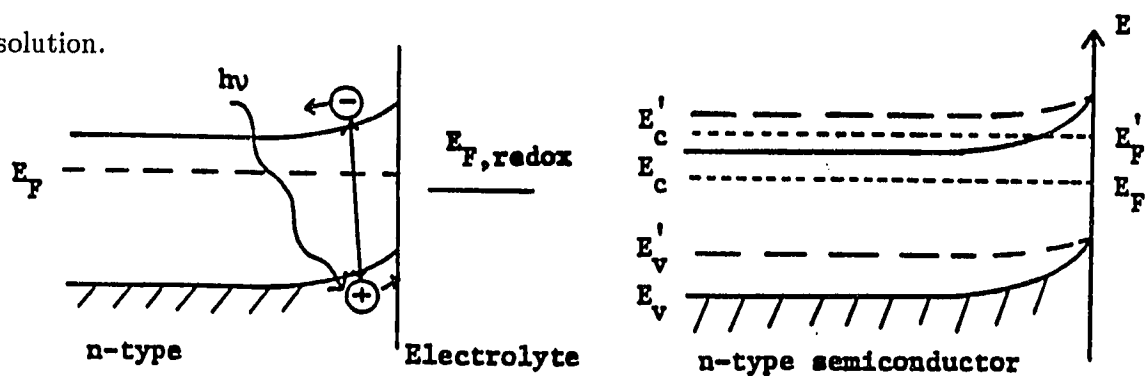
where

$$\Delta E_{nF} = kT \ln\left(\frac{n_o + \Delta n}{n_o}\right) \approx kT \ln\left(\frac{\Delta n}{n_o}\right)$$

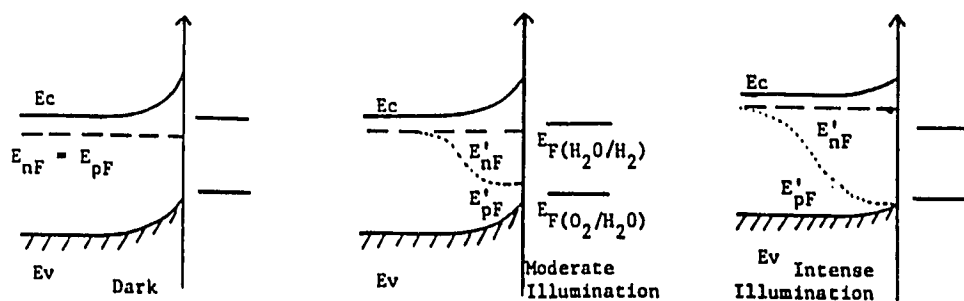
if $\Delta n \gg n_o$.



a) The Fermi level within an n-type semiconductor before and after immersion in a redox solution.



b) The strong field at the interface separates the charges produced upon illumination (on the left). The photovoltage is the change in the Fermi level during illumination. E'_c and E'_v are the conduction and valence bands under illumination.



c) The quasi-Fermi levels in an n-type semiconductor at the electrolyte interface under various light intensities.

Figure 2.4: The effects of illumination on an n-type semiconductor in a redox electrolyte.

$$E'_{pF} = E_{pF} + \Delta E_{pF} \quad (2.2)$$

where

$$\Delta E_{pF} = kT \ln\left(\frac{p_o + \Delta p}{p_o}\right) \approx kT \ln\left(\frac{\Delta p}{p_o}\right)$$

if $\Delta p \gg p_o$. The changes in Fermi level are the largest for the minority carriers. The equations above state that under illumination the chemical potentials of holes and electrons differ substantially. The minimum energy requirement to split water is a difference in these Fermi levels equal to the decomposition voltage of water. The Fermi level of electrons should be above the water/hydrogen redox potential ($E_{F(H_2O/H_2)}$) and the Fermi level of holes should be below the water/oxygen couple ($E_{F(O_2/H_2O)}$). As illustrated in Figure 2.5 [37], the minimum energy required for decomposition at 25°C is :

$$\Delta E = E_{F(H_2O/H_2)} - E_{F(O_2/H_2O)} = 1.23 \text{ eV} \quad (2.3)$$

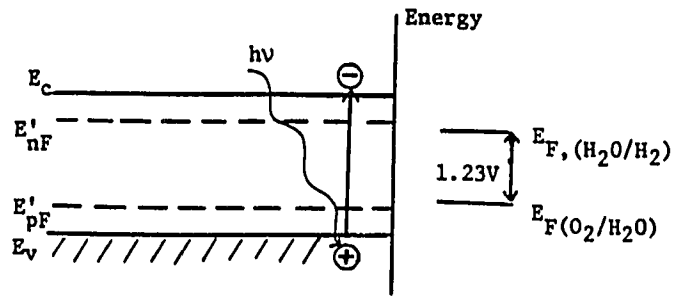


Figure 2.5: The minimum conditions for water decomposition with zero potential application.

Since the band gap always exceeds the difference in Fermi levels between holes and electrons, the band gap of the semiconductor should exceed the difference in redox levels by 0.4 - 0.6 eV [37]. Also illumination must be intense enough to split the quasi-Fermi levels of holes and electrons (E'_{nF} , E'_{pF}) as shown in Figure 2.4(c). The divergence in Fermi levels will be small in the bulk of the semiconductor and large at the interface. The maximum photovoltage will be the flat band potential (V_{fb}).

2.2 Energy Level Diagram of a PEC Cell

Aside from determining the band gap, the energy band positions relative to the energy levels in the electrolyte also determine the biasing requirements for the chemical producing cells. In Figure 2.6 [42], the redox potentials of water are indicated as reference. Only the materials in the first group (to the left of Si) are in principle able to drive photodissociation of water in the absence of an applied external potential.

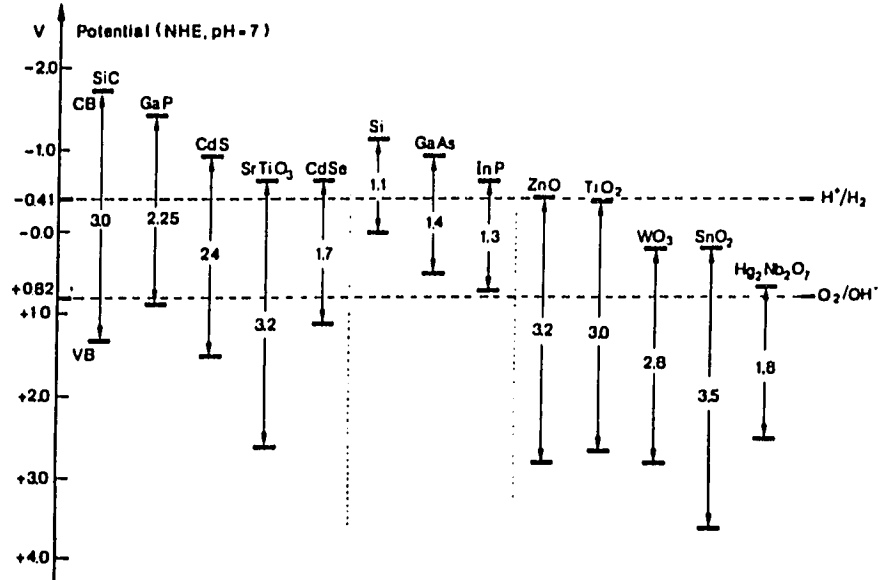


Figure 2.6: CB, VB energies and E_g values of several semiconductors.

The minimum potential required to drive the electrolysis reaction is the free energy for the dissociation of water into H_2 and O_2 , plus the intrinsic overpotentials which are determined by the band gap of the semiconductor, the flatband potential and the redox potential of the electrolyte acceptor state. The voltage supplied by the semiconductor-electrolyte junction and the external bias must be sufficient to overcome these potentials, plus additional IR losses due to current flow through the semiconductor, electrolyte and interfaces [53].

For operation under short circuit conditions, the conduction band (CB) must intercept the interface so that a depletion layer exists. Thus, for an n-type semiconductor the electron affinity must be smaller than the cathodic redox potential in the electrolyte as measured from the vacuum level. Conversely, for a p-type semiconductor the valence band (VB) should intercept the interface below the anodic redox potential in the electrolyte.

The operation of chemical producing PEC cells drive two irreversible electrochemical couples, one of which takes place at the anode and the other at the cathode. This results in a net chemical change in the electrolyte. The net amount of energy stored is the difference between the two couples. The relationship between the electron affinity (EA) and the flatband potential (V_{fb}) is illustrated in Figure 2.7 [28] where the energy levels are shown for zero external bias.

The width of the depletion layer is a function of the applied potential as in a normal Schottky barrier. The flatband potential, V_{fb} is the position of the original Fermi level in the semiconductor when the depletion layer goes to zero width (no band bending) measured relative to whatever reference electrode is being employed. With no depletion layer and therefore no electric field to separate the photogenerated electron-hole pair, the photocurrent should also go to zero at this potential. Differences between the onset of the photocurrents and flatband potential determined from capacitance

data ($V_{\text{applied}} \propto C_{\text{junction}}^{-2}$) indicate the existence of recombination centers or surface states within the semiconductor gap [28]. When these are absent, the photocurrent onset can be used to determine the flatband potential which in turn determines the bias requirements of a chemical producing PEC cell. The potential difference between the semiconductor band edge and the redox potential at the counterelectrode is the maximum obtainable band bending. The more negative the flatband potential for an anode material, the higher the band bending [45]. The electron affinity (or more precisely the work function) is the characteristic property of a semiconductor that determines the flatband potential when the material is immersed in an electrolyte, just as it determines the contact potential difference between the semiconductor and a metal.

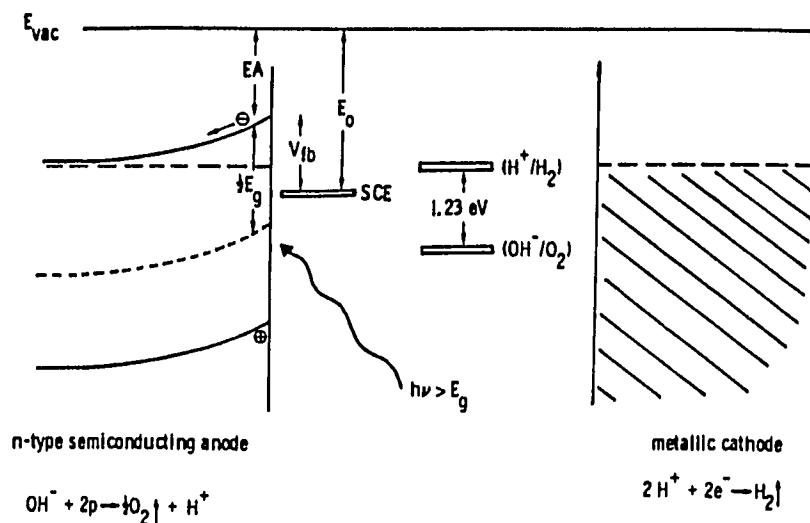


Figure 2.7: Energy level diagram for a photoelectrolysis cell.

Assume that the V_{fb} is unchanged under illumination. It determines the maximum quasi-Fermi level possible for electrons in n-type semiconductors. It is particularly useful to be able to predict V_{fb} for a potential semiconductor to evaluate its promise as a photoelectrode. This can be seen by referring to Figure 2.7. For a typical photoelectrolysis cell, the electron affinity (EA) for the semiconductor is given as :

$$EA = E_o + V_{fb} + \Delta_{fc} + \Delta_{px} \quad (2.4)$$

where E_o is a constant relating the reference electrode (saturated calomel electrode, SCE) to the vacuum level, Δ_{fc} corrects for the difference between the doped Fermi level and the bottom of the CB, and Δ_{px} is the potential drop across the Helmholtz layer due to ions absorbed on the n-type semiconductor surface. While there is some uncertainty E_o can be taken as 4.75 eV for the SCE at 23°C [28]. Δ_{fc} is typically 0.1 eV for the highly doped semiconductors [28].

Bulk EA for an intrinsic semiconducting solid is given in terms of bulk electronegativity (χ_{bulk}) as shown below and the bulk electronegativity is the geometric mean of the atom electronegativities of the constituent atoms [28] :

$$EA + \frac{1}{2}E_g = \chi_{bulk} \quad (2.5)$$

If the correction term Δ_{px} is evaluated, V_{fb} can be predicted from Equation 2.4. Although a detailed understanding of ion adsorption at the semiconductor/electrolyte interface is not clear, a number of things are known [28]:

1. If the V_{fb} of the semiconductor shifts with concentration of ions in the electrolyte, then some ion species in solution are specifically adsorbing on the semiconductor surface.
2. For metal oxides in simple acids and bases, the V_{fb} shifts by 59 mV/pH unit due to specific adsorption of H^+ and $(OH)^-$.

3. The net surface charge (varied by changing concentration in solution) depends on the relative electrochemical potentials for the two adsorbing species in adsorbed states in the solution.
4. Some concentrations of ions in the solution exist at which the coverages by the two oppositely charged species are the same and thus the net surface charge is zero (point of zero zeta potential, PZZP). At this point there is no potential drop across the Helmholtz layer due to adsorbed species and therefore $\Delta_{px} = 0$. Therefore for metal oxides: $\Delta V_{fb} = (59 \text{ mV})(pH_{PZZP} - pH)$.

In practice, the flatband potential is determined by measuring the capacitance of the electrode/electrolyte interface at various frequencies and at different electrode potentials and by plotting C^{-2} as a function of electrode potential. The capacitance of the interface in an electrolyte changes with frequency, but the intercept on the potential axis is nearly the same [39].

2.3 Materials Aspects of PEC Cells

2.3.1 Semiconductor Material Requirements for the PEC Cells

For an efficient utilization of light energy, the incident photons should be totally absorbed within the space charge (electron depletion) region whose thickness depends on doping level (carrier density) and dielectric constant of the semiconductor [36, 28]. Quantum efficiency (number of electrons flowing in the cell per photon absorbed) should also be high for a PEC system.

Even when photons are completely absorbed in the depletion zone, a part of the photon energy ($E > E_g$) is lost as heat to the lattice since vibration relaxation occurs in the upper excited state before the charge transfer takes place [36]. The maximum energy conversion efficiency which directly depends on the E_g of the semiconductor is given as 7 % for TiO_2 ($E_g = 3 \text{ eV}$) and 30 % for Si ($E_g = 1.1 \text{ eV}$) [37]. Therefore,

wide band gap semiconductors (those of $E_g > 2.5$ eV) are of little practical use unless means are found to enhance their visible light response by inducing sub-band gap states.

Long term stability is the most crucial condition to be met by a semiconducting photoelectrode. It must not only be stable against chemical dissolution in the electrolyte, but also against electrochemical corrosion and photocorrosion which may form a new phase on the electrode as holes reach the surface.

Consider an n-type semiconductor electrode. A minority carrier, a hole, is attracted to the surface by the band bending upon illumination. For the chemical energy production, the holes should oxidize one species at the semiconductor and the electrons reduce another species at the counter electrode. It is clear that the rate of consumption of photoproduct holes, and of electrons in solution, must be equal. The arrival of a hole at the surface and its association with the surface atom indicate that one of the valence bonds between the surface atom and the rest of the crystal is broken. Therefore, holes in an n-type material may be considered as partially broken bonds. Any of the three reactions below can occur if the holes are very energetic, but one reaction will dominate [49] :

1. If the ions from the semiconductor are soluble when oxidized by the holes to a higher valence state, the semiconductor can dissolve.
2. When the ions from the semiconductor are insoluble, a new phase can form.
3. When the holes find it thermodynamically more favorable to react with a species in solution than to react with the semiconductor itself, the semiconductor is unchanged.

GaP is an example of either the first or the second case, depending on the nature of the solution [44]. Silicon almost always provides an example of the second case. In the case of p-type silicon, but not in the case of n-type, a very high voltage can induce

anodic dissolution [47]. Titania (TiO_2) offers an example of the third case, yet when sulfate ions are present so the titania can form a soluble complex, decomposition is observed [62]. In general, the smaller the band gap the less stable the material [47]. The possible semiconductor decomposition energy levels are shown in Figure 2.8 where ${}_nE_{decomp}$ implies the thermodynamic energy level for the electron induced corrosion relative to the hydrogen scale and ${}_pE_{decomp}$ is for the hole induced process and E_{cs} , E_{vs} are the energies of the CB, VB edges at the surface. If $E_{vs} < {}_pE_{decomp}$, holes will be corrosive and if $E_{cs} > {}_nE_{decomp}$, electrons will be corrosive. Therefore, the four possible cases are as shown :

- a) relatively stable semiconductor,
- b) instability if either electrons or holes reach the surface,
- c) instability to holes,
- d) instability to electrons.

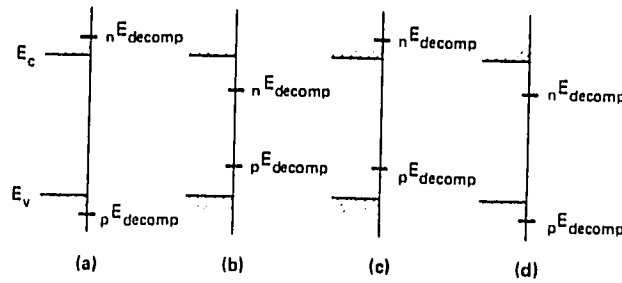


Figure 2.8: Possible positions of the decomposition energy levels relative to the band edges.

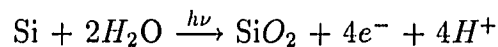
Silicon is the most widely used electrode material in PEC systems. The indirect band gap of silicon, however, necessitates the use of rather thick layers. Amorphous silicon, on the other hand, has a direct band gap transition which is more optimally matched with the solar spectrum ($E_g = 1.4$ eV vs $E_g = 1.1$ eV for crystalline Si) [58]. Although this type of cell seems to approach the performance of n-Si under comparable conditions, there is a need to determine the stability and reliability of these devices [40].

As introduced before, the rapid photocorrosion and/or surface passivation of the desirable semiconductor materials restrict their direct use under irradiation in aqueous solutions. This problem can be overcome by protecting the "light-harvesting" semiconductor electrode surfaces by suitable coatings. Therefore, the requirements for a reasonable coating material will be given next.

2.3.2 Protective Coatings For the PEC Cells

The selection of a coating (with suitable physical and chemical properties) is important to the overall photoelectrode performance, however its quantitative effect has not been resolved. The protective ability of a coating requires the isolation of the photoanode surface from the aqueous environment allowing the oxygen evolution to occur on the coating surface.

It is expected that any coating that can protect a Si surface can more than likely protect most other photoelectrode materials also. n-Si is very susceptible to oxidative passivation because an insoluble and insulating SiO_2 film continually grows on the photoanodes [4] in the presence of water through the reaction of [47]:



Therefore a stable photocurrent in the presence of aqueous electrolyte is definitive evidence that the coating performs in the desired manner.

The properties of an ideally performing electrode may be modelled as in Figure 2.9. Each of these regions shown in the figure should be optimized for a good performance. In order to be useful for solar energy conversion, the protective films on the semiconductor surface have to be transparent to most of the visible part of the solar spectrum, and also electrically conducting to allow charge transfer between the semiconductor and specific redox species in solution. The coatings should also be highly robust and adhesive in order to provide effective barrier protection to the photoelectrode for years of operation at potentially high temperatures in an aqueous electrolyte environment [62].

Various surface films such as transition metals and their oxides, sulfides and also organic polymers etc. have been coated on various type of semiconductors [23, 55, 39]. However, convincing data on long term stability is absent in all cases. The properties of the films considered most important are electrical resistivity, optical transmission, environmental stability, the chemical nature, structure and morphology of the film surface, and chemical resistance of the films. Metal and metal-like semiconducting electrode coating films can have a coverage varied from catalytic amounts (much less than a monolayer (ML)) to complete coverage and fairly thick (a few hundred angström) films. However, catalytic amounts of metal will not generally afford corrosion protection for n-type semiconductor electrodes, because of electrolyte attack through the porous overlayer. Metal overlayers will induce Schottky barrier formation at the metal-semiconductor interface if the electrostatic factors (work function-electron affinity differences) are satisfied [59]. In such cases, the electrolyte merely functions as a carrier collection medium and a constant photovoltage is developed at the metal-semiconductor interface regardless of the location of the solution (redox) potential, ("heterojunction photoelectrode"). Degenerate oxide semiconducting coatings can be a better alternative to the use of metal overlayer films which necessitates

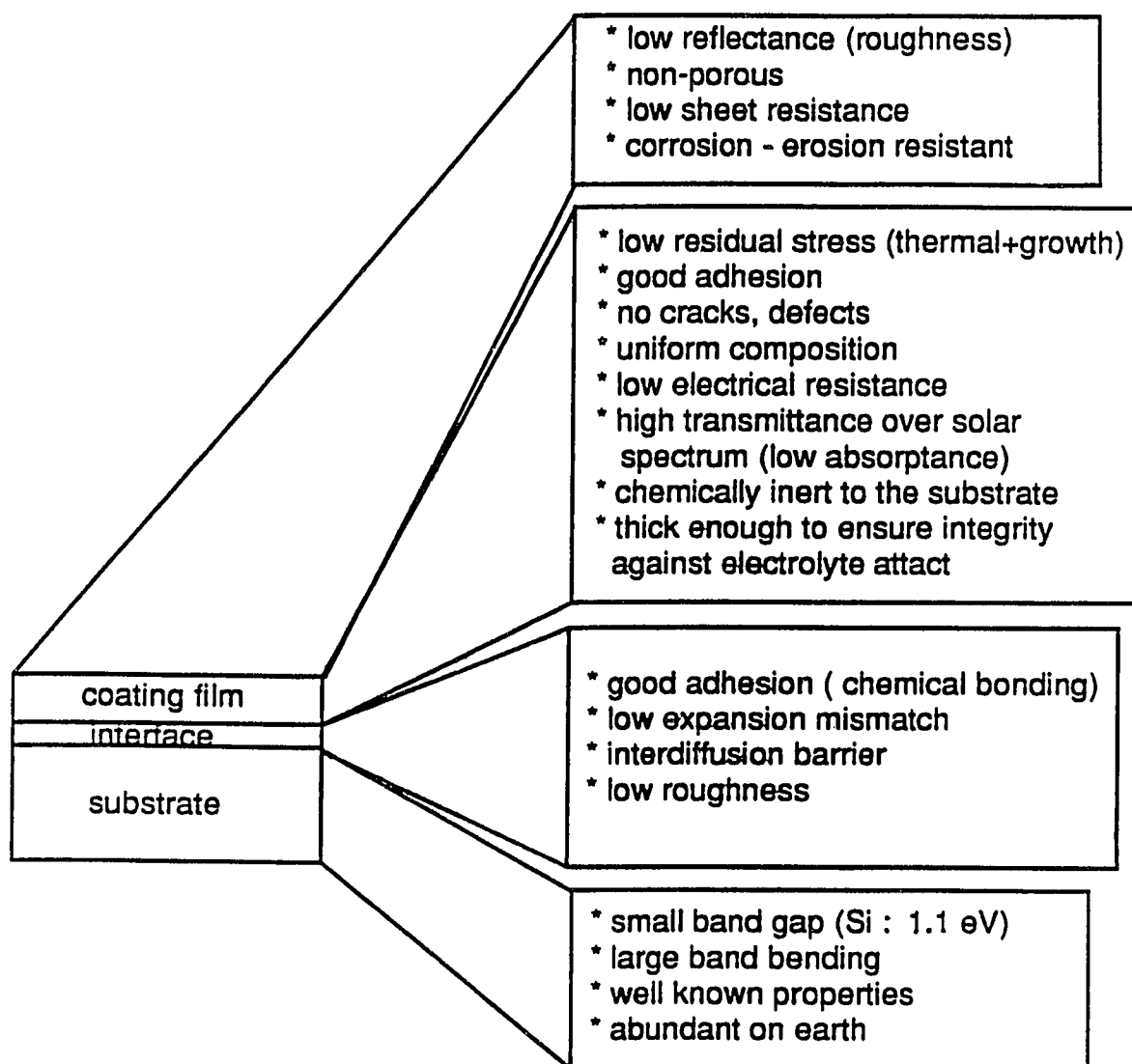


Figure 2.9: Properties of an ideal photoelectrode system, in terms of surface, bulk coating and interfacial properties.

the balancing of absorptive losses with the maintenance of adequate film thickness.

Polymers as protective coating layers have been used recently [62]. However the use of a metal underlayer might provide better adhesion, increased corrosion protection and also can enhance the charge transfer rate at the electrode- polymer-electrolyte interface [58]. Dyes as the third type of the electrode coating materials are employed for semiconductor stabilization, however somewhat contradictory results have been reported [58]. Oxides inert to the substrate may be used in coatings as a physical barrier to oxygen. The failure mechanism is diffusion of molecular oxygen through pores or cracks in the oxide coating to the substrate.

As a direct consequence of the electromagnetic theory, perfect electrical conductivity and complete transparency in any material represent a contradiction because the incoming electromagnetic wave is dissipated by heating the charge carriers. Besides this, there are numerous other sources of light loss which depend upon the film material, its structure and surface morphology [68]. Ideally one would like the thinnest possible continuous film to obtain sufficient electrical conductivity and transparency. Therefore, low substrate temperature, low deposition rate, low vapor kinetic energy (source temperature), vapor incidence normal to the substrate and charging of the substrate and incident vapor promote reduced agglomeration and early coalescence of depositions in general. However more granular and optically absorbing metallic coatings have been observed with increasing vapor incidence angle or with decreasing rate of deposition. The physical properties of the film depend on the deposition technique such as hydrolysis, pyrolysis, evaporation and sputtering, screen printing, UV-reduction of salts, vapor transport, glow discharge decomposition, etc. [68].

As transparent conductors; if the protective films are metals, their properties depend on film nucleation and initial coalescence phenomena affected by the substrate material. However, semiconducting oxide film properties depend critically upon their

oxidation state (stoichiometry) and on the nature and quantity of the impurities trapped in the film. The semiconducting oxides used have relatively high indices of refraction (e.g 2.0) and low extinction coefficient defined by the ratio of $\frac{\alpha\lambda}{4\pi}$, where α is the absorption coefficient. However, metals used have low refraction indices and high extinction coefficients.

In this chapter, the theoretical background on the photoelectrochemical processes and some practical application examples were given. The alternative electrode model will be chosen and characterized next.

Chapter 3

Thesis Proposal

3.1 A Review on the Protective Coatings

The most efficient PEC cells are made from electrocatalyzed photocathodes and protected non-oxide small band gap semiconducting photoanodes [12]. As protective coatings, conducting polymers and glasses can be applied on semiconductors. However, plastics tend to be degraded by long exposure to sunlight, while glasses are subjected to impact damage.

For use in water photoelectrolysis, n-Si electrodes have been protected from any contact with water by depositing transparent and conducting thin films of indium tin oxide [34], iron oxide [55], Pt-doped SiO_x [13], metal silicide [23], Mn-oxide [39] and Au/TFE [62].

1. Schwerzel and Spahr [62] studied conducting polymer coatings on different semiconductors. They observed that Au/TFE metallic plasma polymer film on n-Si loses its integrity (adhesion) fairly soon after water is added to the cell.
2. Nakato et al. [50] studied the effect of the Pd coated Au film evaporation speed on the photovoltaic behavior of the n-GaP electrode. A 200 Å gold film on glass plate showed 50 % light transmittance at 500 nm and 30 % transmittance at 420 nm. Fast evaporation (40 Å/s) which leads to coarse grained films allowed 25 % quantum yield under 420 nm illumination (0.1 mW/cm²) or 11 % energy conversion efficiency, or 1-2 % solar efficiency in acetate buffered 0.5 M K_2SO_4

aqueous solution of pH=4.7. The photocurrent from the samples was recorded under no external potential for an hour and it remained stable.

3. Hodes and co-workers [34] deposited successive layers of SiO_x (15 Å) and 400 Å indium tin oxide (ITO) on n-Si by spray pyrolysis. RuO_2 or Pt was deposited on ITO to electrocatalyze the Cl_2 and O_2 evolution. The stability of the electrode was shown for 65 hours of continuous illumination during Cl_2 evolution in an $[\text{Fe}(\text{CN})_6]$ redox electrolyte (pH ≥ 7).
4. Contractor et al. [13] doped the silica film (100 Å) formed on the Si surface by dispersing Pt in the film so that the resistivity of the film was reduced and thus limiting its growth. The electrode kept at 2.02 V (vs the hydrogen couple (NHE)) was shown to be stable up to ~ 100 hours, but decayed sharply after ~ 120 hours of continuous illumination during O_2 evolution in 0.5 M H_2SO_4 solution.
5. Fan et al. [23] deposited noble metals on n-Si by vacuum evaporation and heated them at high temperatures to convert the surface to metal silicides in order to evolve chlorine and oxygen. A thin coating of Ru-oxide on the silicide surface was required to ensure stability. An IrSi/n-Si electrode was stable during Cl_2 evolution for ~ 200 hrs of continuous illumination.
6. Kainthla et al. [39] deposited 200 Å uniform, continuous Mn_2O_3 on n-Si and n-GaAs by using a CVD technique. Except for a small decay in the first few hours of testing, the n-Si sample kept at 1.3 V (vs NHE) showed no decay in photocurrent for 650 hours of continuous operation in 0.5 M K_2SO_4 solution.
7. Osaka et al. [55] used electron beam deposition of 400 Å Fe film on n-Si(100) and heated the electrode to 400°C for 1 hr in 0.1 Torr O_2 atmosphere to form 750 Å Fe_2O_3 on the surface. Vacuum evaporation of a Pd layer on the oxide showed 20 % higher quantum yield in 0.2 M KOH solution, however the stability data for these electrodes was not given.

The coatings mentioned above degraded with time by either surface pinhole formation due to imperfect films, or surface insulating thin film growth or breakdown (physical disruption) of the films. Also, the current densities (1 mA/cm^2 vs 20 mA/cm^2) and time periods (1 hr vs 650 hrs) over which the stabilities have been studied change between authors. In this work, the electrolyte and the electrode structure are kept very simple to observe the effect of an oxide thin film on the passivation of the underlying semiconductor substrate. In review of these studies, it was observed that long term stability of the photoactivity should be studied further.

3.2 Proposed Electrode Model

The model substrate chosen is silicon (n-Si), mainly because of the advanced degree of technology and understanding that exist. Its small energy band gap allows more efficient conversion of the solar energy. However, silicon is very susceptible to oxidative passivation (SiO_2 formation), therefore, if the coating protects the surface, it is very likely that it can be applied on the other photoelectrode materials to serve the same purpose.

In order to be useful for solar energy conversion, the protective films would have to be transparent to most of the visible spectrum, electrically conducting to allow electron transfer between the semiconductor and specific redox species in the electrolyte, and also aqueous solution photocorrosion resistant [62]. A sufficiently thin, continuous coating of aluminum oxide is very likely to protect the n-Si single crystal surface and allow fuel production through the quantum tunneling phenomenon. Therefore, it is expected to improve the stability of photocurrent in the cell in comparison to the untreated semiconductor surface. The final composition of the oxide was attempted to be that of sapphire ($\alpha\text{-Al}_2\text{O}_3$, alpha alumina, corundum, aluminum oxide [16]).

The kinetics of a PEC hydrogen generation process is sluggish on all semiconductor surfaces in general [58]. In the cell, naked or coated n-Si serves as the photoanode where it would be possible to observe the effect of oxygen evolution on the electrode material performance and hydrogen evolution would be observed on the Pt counter electrode surface.

3.2.1 Absorption and Transmission Properties

As illustrated in Figure 2.10, for an efficient utilization of light energy, the incident photons should be totally transmitted through the protective coating to the semiconductor which should totally absorb the light in its space charge (electron depletion) region. Even though the lifetime (i.e. time required for the photogenerated (excess) carriers to diffuse to the boundary without any recombination in the semiconductor and also on the surface) is longer for the indirect gap semiconductor materials (e.g. 10^{-3} sec for Si as compared to the direct gap material GaAs with 10^{-8} sec) [11], the thickness needed to absorb most of the incident radiation is larger. The thickness of the Si wafer to be used can be calculated by the use of Figure 3.1 [11].

The critical photon frequency ($\frac{E_g}{h}$, where h is the Planck's constant) is defined as the frequency below which there is no absorption of photons by the semiconductor. The number of photons in a beam which has traversed a distance x of material with an optical absorption constant α is given by :

$$N_x = N_{x=0}(e^{-\alpha x}) \quad (3.1)$$

Therefore the thickness of a semiconductor to absorb 90 % of the incident radiation ($N_x = 0.1$ and $N_{x=0} = 1.0$) is calculated as : $\alpha x \geq 2.30$. Thus $x_{min} = 2.3/\alpha$. n-Si has an E_g of 1.1 eV which corresponds to a critical photon wavelength of $1.13 \mu\text{m}$ above which there is no absorption. As a result, a 0.36 mm (14 mils) thick Si wafer would absorb at least 90 % of the incoming radiation with $\lambda = 1.0 \mu\text{m}$ ($=1000 \text{ nm}$) or less.

The protective coating on the Si electrode should be transparent to allow the incoming light to reach the semiconductor. The transmission region of sapphire is shown in Figure 3.3 [9]. It is observed that 2 mm thick sapphire shows at least 10 % transmission at the wavelengths between 0.14-6.5 μm . This wavelength region also contains the highest energy flux of solar radiation (visible range $\lambda = 0.4\text{-}0.8 \mu\text{m}$) as shown in Figure 3.2 [11].

Sapphire which is very hard to abrade encounters not more than 3 % transmission loss when it is heated to 440°C and it transmits 55 % at 0.2 μm [9]. Although absorption is a slowly varying function of wavelength, it has an exponential dependence on film thickness. In metal oxides, absorption is due to the displacement of an outer electron in the molecule rather than charge carrier absorption [68].

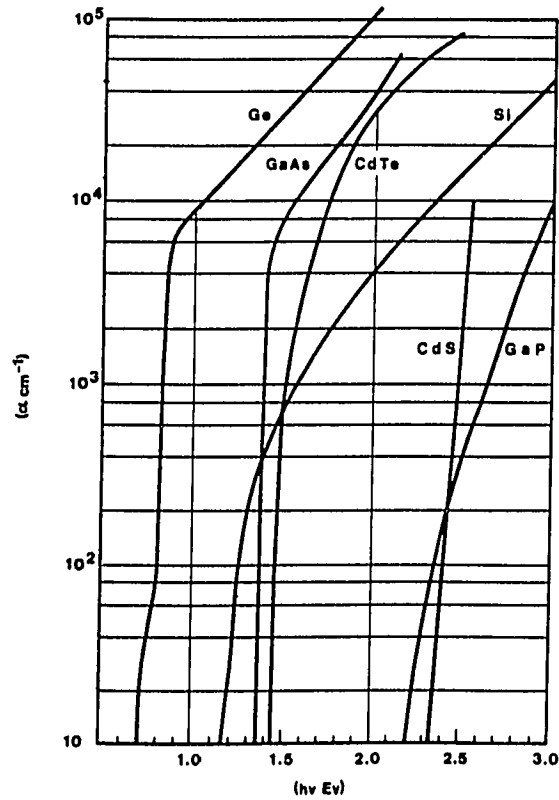


Figure 3.1: Optical absorption constant, α , as a function of photon energy.

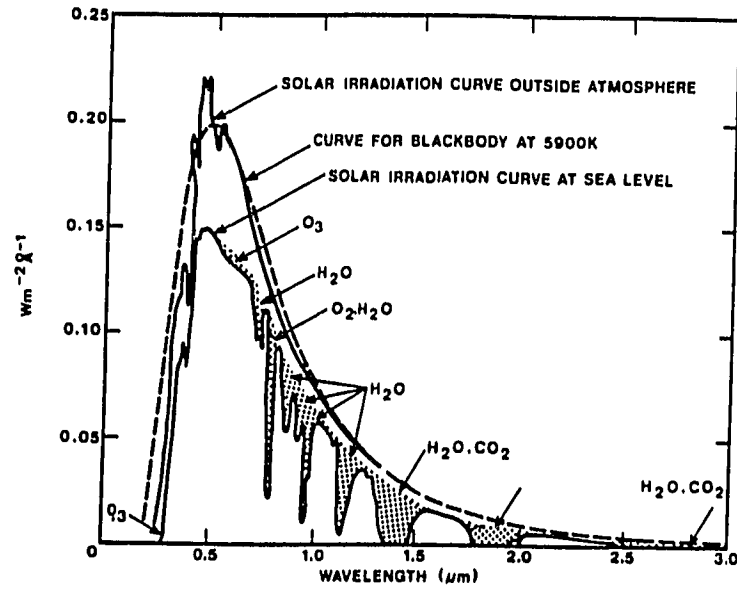


Figure 3.2: Spectral distribution curves related to the sun.
Shaded areas indicate absorption at sea level due to the atmospheric constituents shown.

Al-oxide coatings of different thicknesses will also be deposited onto quartz glass slides to study their optical properties by recording the transmission spectra. The configuration can be modelled as shown in Figure 3.4. The optical transmittance, T , of the films on transparent substrates for a normal light incidence is given by Abass et al. [1] as:

$$T = Ke^{-\alpha x} \quad (3.2)$$

where

$K = A(1-R)(1-R')$, the transmission at the absorption edge.

A = absorbance = $-\log T$

R = reflection coefficient at the air-coating interface.

$$= \frac{(n-1)^2 + k^2}{(n+1)^2 + k^2} \quad (3.3)$$

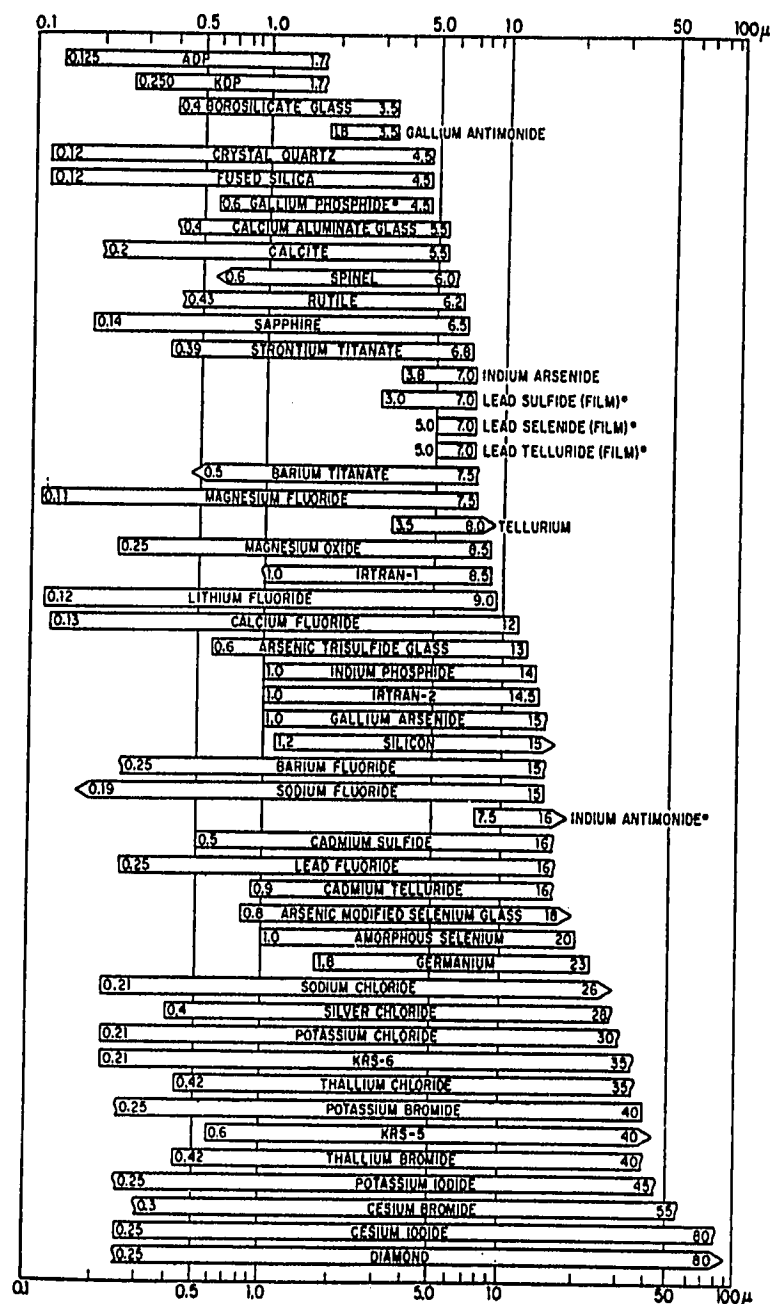


Figure 3.3: Transmission regions of special crystals and certain glasses. Materials marked with an * have a maximum external transmission of less than 10 %.

where

n = refractive index of the film.

k = extinction coefficient of the film.

R' = reflection coefficient at the coating-substrate interface.

$$= \frac{(n - n')^2 + k^2}{(n + n')^2 + k^2}$$

where

n' = refractive index of the substrate.

α = absorption coefficient.

x = film thickness.

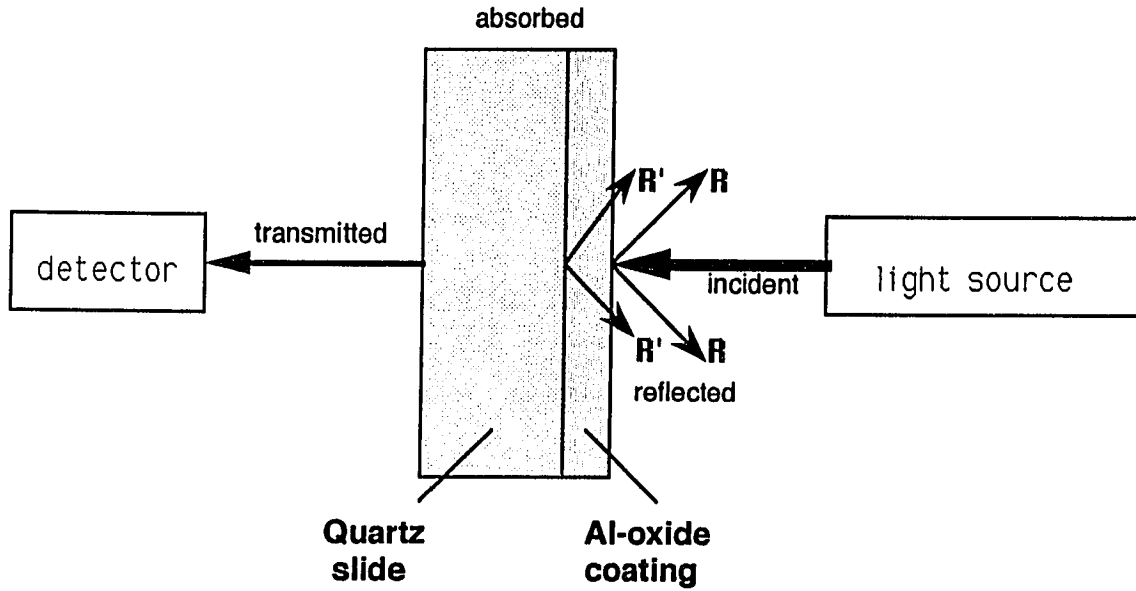


Figure 3.4: The model electrode for optical transmission measurements.

K can also be given as [27] :

$$K = \frac{16n_{air}n_{glass}(n_{film}^2 + k^2)}{[(n_{air} + n_{film})^2 + k^2][(n_{glass} + n_{film})^2 + k^2]}$$

where

n_i = refractive index.

k = extinction coefficient ($= \frac{\alpha\lambda}{4\pi}$).

The index of refraction of sapphire is around 1.8 for the region between 0.27-1.5 μm [9] and this makes it a partial anti-reflection (AR) coating on Si. Al_2O_3 has a refractive index about that of glass and thus very thin oxide films would not be easily seen on glass surfaces [35]. The wide band gap (around 7 eV) results in minimal visible light absorption in the oxide layer and thus allows most of the light to be absorbed in the oxide-semiconductor junction area. Schwerzel [62] states that 30-65 % transmittance through visible region is acceptable for a coating.

3.2.2 Electrical Conduction in Insulating Films

Al-oxide coatings on Si are expected to be amorphous as this will be elucidated in the next chapter. The energy band description of the system can be applied at least qualitatively to understand the electron transfer through the oxide layer between a semiconducting electrode and a conducting electrolyte.

The various localized levels, A through F are seen in Figure 3.5 [49] for a surface film on a semiconductor. The amorphous film with bulk defects has "bands" because there are allowed energy levels corresponding to the orbitals of the valence electrons on the anions and to the orbitals of the next excited states, when the electron is essentially on the cation. However, since each lattice site in an amorphous film is not identical with respect to its nearest-neighbor distance and orientation, the energy levels are not necessarily identical in the sense of the Pauli exclusion principle. Most of the orbitals are approximately the same, but there will always be a few that have somewhat unique bonding configurations. Some of these unique orbitals will provide

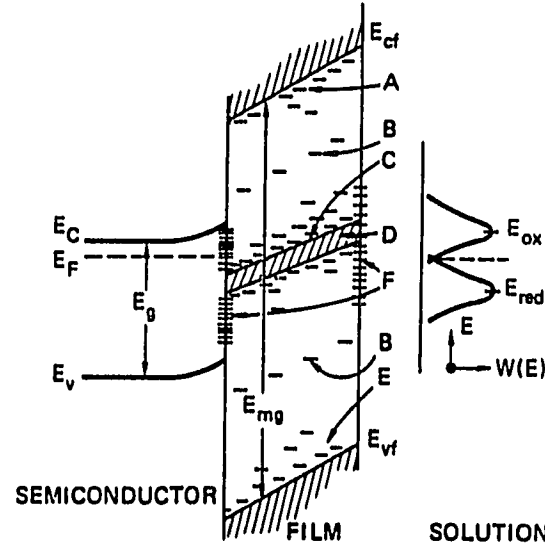


Figure 3.5: The band model for an amorphous insulating layer over a semiconductor.

the levels A and E. The energy levels A represent cation levels that have a bonding configuration resulting in a somewhat higher electron affinity than most of the cations have. The levels E represent those few valence electron orbitals where there is a lower ionization potential than most of the anions have. CB electrons at an energy higher than the top edge of the mobility gap (E_{mg}), E_{cf} , can move. They are in a region of energy where there are enough identical orbitals that there is overlap between levels, and the electron can hop from one end of the film to the other through these identical orbitals. Holes with an energy level below the bottom edge of the mobility gap, E_{vf} , can also conduct: they are in a region of energy where the orbitals overlap sufficiently for transport of the holes. The energy levels A and E are almost the same as the CB and VB energy levels respectively, but are rare enough that if an electron becomes trapped in an energy level A, or a hole in an energy level E, they can not easily hop from one site to the next across the film.

The levels D represent the possibility that an impurity band, or a narrow band associated with another oxidation state of one of the ions of the lattice, could be present with an energy level density high enough for conductance. For example, 10^{26} m^{-3} or 1 % of the atoms is enough for orbital overlap for carriers to hop from one level to the next across the film. In the case of such an impurity band, there will be localized levels above and below the band associated with atoms that do not have a typical bonding structure and so have a different energy level from the norm (level C). As in the case of A and E, again electrons or holes in these levels do not have overlapping wave functions and so can not hop from one level to the next across the film.

The possibility of energy levels for impurities or imperfections in the film that are relatively rare (say, less than 10^{24} m^{-3}) that provide traps in the material is designated as B in Figure 3.5. Two processes are necessary for conduction in such a "perfect" amorphous film. First, carriers must be injected into one of the "bands" (E_{cf} or E_{vf}) and second, the carriers must be transported across the film without being trapped.

Now, consider the states at the interface between the semiconductor and the film and the solution. These states, designated by F, between the oxide and the solution are expected to behave similarly to surface states at any semiconductor/solution interface, and are usually expected to be dominated by adsorbed ions such as H^+ and $(OH)^-$. Much more important are the states between the semiconductor and the oxide and they arise because of mismatch between the semiconductor and the film that leaves dangling bonds or other nonbonding orbitals. They may also arise because of nonstoichiometry of the oxide in a transition layer between the conductor and its oxide. They may also be due to impurities that become localized at the interface. Si/SiO₂ interface is by far the most perfect interface known and has a density of 10^{14}

$m^{-2}(eV)^{-1}$ [49]. If such interface states are in sufficient density, they will pin the Fermi level. This implies that [49]:

1. The flatband potential will shift to a higher or lower electrode potential depending on the charge on the states. Any change in electrode potential will appear across the oxide layer, so the current will be dominated by conductance through the oxide thicker than the Helmholtz double layer. Breakdown will also be controlled by the oxide, not the semiconductor.
2. They provide a charge storage location other than the Helmholtz double layer and lead to very high Helmholtz potentials.

A large number of nearly amorphous insulating materials are known which, when a high electric field is applied to thin films of the substance, exhibit current flow which increases roughly exponentially with applied voltage over many decades [46]. This electrical conduction behavior in insulators has been explained by several mechanisms [48]:

- a) direct tunneling of electrons from one metal to another (it depends least strongly on the actual microscopic structure of the insulator),
- b) injection of carriers into the CB or VB of the insulator, i.e. thermionic (Schottky) emission over a contact barrier,
- c) tunneling through the contact barrier, i.e. field emission. Processes in b and c are analogous to the corresponding emission from a metal into vacuum.

Simmons [64] has shown, on the basis of parametric calculations of the current-potential (I-V) characteristics of a tunnel structure, that at $300^\circ K$ and for a barrier thickness (s) where $s < 40 \text{ \AA}$, direct tunneling predominates. However, for $s > 40 \text{ \AA}$, either the thermionic or the tunnel mechanism can predominate, depending upon the barrier height (work function) and the applied potential. The tunnel current can also vary with temperature because of the temperature dependence of the barrier height.

According to Bashara [6], dielectric layers of less than 100 Å in thickness were required to obtain cold emission by tunneling. For the Pb- Al_2O_3 -Pb sandwich samples, the current through the oxide was 1 mA at 7 V [57]. Therefore, Pollack found that the Schottky-like behavior of current-potential is to be used for the study of Al-oxide with a thickness between 100-1000 Å and at a temperature above 250°K (−23°C). The Schottky emission expression is given as [6]:

$$J = AT^2 \exp\left(\frac{1}{kT} \left[\left(\frac{q^3 V}{4\pi \epsilon d}\right)^{\frac{1}{2}} - q\phi\right]\right) \quad (3.4)$$

where

J = current density in amps/ cm^2 .

A = Richardson constant = 120 amp/ $cm^2 K^2$.

T = temperature in degrees Kelvin.

k = Boltzmann's constant = 1.38×10^{-23} Joule/degree K.

q = electronic charge = 1.6×10^{-19} coulomb.

V = voltage applied to the anode.

$\epsilon = \epsilon_o \epsilon_r$

where

$\epsilon_o = 8.854 \times 10^{-12}$ farad/meter.

ϵ_r = relative dielectric constant.

d = dielectric thickness in meters.

ϕ = effective work function at the metal-dielectric interface, in eV.

For Al- Al_2O_3 (50 Å)-Al structure, 1 mA current was obtained at an applied voltage of 0.5 V [25]. The films showed an exponential current rise with voltage and vacuum tunneling behavior at low temperatures. For Al_2O_3 films less than 100 Å thick, the dominating conduction process was direct tunneling from one metal to the other.

3.2.3 Long Term Stability of the Oxides

Many of the oxide ceramics have strong ionic bonds. Of these Al_2O_3 has the most stable physical properties, with excellent heat and corrosion resistance [16]. Although alumina can be represented simply by the chemical formula Al_2O_3 , its nature varies considerably depending on its crystalline form, the impurities present, and the particle diameter.

Bulk aluminum mirrors with a thin but dense oxide coating were not attacked by H_2SO_4 plus H_2O for 3 months, but exposure to concentrated H_2SO_4 vapor caused some corrosion with a rate increasing sharply with temperature [35]. Al_2O_3 exhibit good thermal endurance up to $400^\circ C$, and the deposition of a layer of Al_2O_3 enhances the surface resistance of glass [21].

Since Al_2O_3 has very high heats of formation (65 kcal/eq. at $25^\circ C$), lattice energy (617.8 kcal/eq.) and bond energy (122.1 kcal/eq.), etc., the oxide lattice will not undergo a chemical or electrochemical dissolution reaction either in the absence or presence of an applied field [19]. Moreover transport through Al_2O_3 is extremely slow relative to other oxides making them desirable for oxidation protection [51].

Losses in electrochemical cells come from three sources: frictional losses (IR) which depend on the nature of ions in solution, concentration polarization which is a function of the depletion layer between electrode and solution, overvoltages which is related to the activation barriers between electrode and solution. For a high conversion efficiency, it is critical that low polarization resistance occur at both electrodes (working electrode-WE and counter electrode-CE), and that the rate of transport across the cell be rapid. This requirement implies that the spacing between electrodes be small. Pt electrode surface is used for H_2 evolution, since it has a very catalytic surface and the activation energies for processes at a Pt interface are quite low. Therefore the overvoltage for H_2 evolution is the lowest for Pt (e.g. for $0.01 A/cm^2$, $\eta_{H_2}^{Pt} = 0.035 V$,

however $\eta_{H_2}^{Au} = 0.56$ V). Normally electrochemical data should be quoted with respect to the hydrogen couple (NHE), which is defined as zero volts, but since the hydrogen couple is not convenient for day to day work, the SCE is used.

When a working electrode is immersed into a solution, and its potential is measured against a suitable reference electrode with respect to time, an open circuit potential will be achieved corresponding to the equilibrium condition between the electrode, the electrolyte and the governing reactions at the electrodes. The open circuit potential measured is known as the corrosion potential, E_{corr} . However a DC potential, V , above or below the corrosion potential is applied, a net current will be observed corresponding to oxidation reaction at the anode or the reduction reaction occurring at the cathode, depending on the polarization direction. Electrochemical systems usually require large overpotential, $\eta = (V_{appl} - E_{corr})$, to produce significant net current and take place under irreversible conditions. If an overpotential which is more positive than the corrosion potential is applied to the sample, the sample is said to have been anodically polarized and a net anodic current is induced. In the absence of any perturbations of the electrode potential, the equilibrium potential would correspond to the minimum corrosion current possible. As discussed above, if an external perturbation of the electrode potential is used to make the electrode more positive (anodic) with respect to the equilibrium potential, a net anodic current will be realized. In a passive material, a significant rise in the anodic current density should only occur once the oxide layer breaks down [30]. This occurs at the breakdown potential which may give an indication of how much work it takes to cause oxide-layer breakdown and whether or not oxide breakdown is made more spontaneous.

The samples will be investigated by monitoring electrochemical reactions. The cyclic voltammetry technique is useful in the elucidation of pitting corrosion mecha-

nisms particularly in respect of the identification of intermediates. Short-lived intermediates even can be identified with the very high sweep rates generated by modern electronic techniques. In this technique, the applied potential is varied with time (in a triangular wave form) up to a limit, while the resulting current is detected and recorded over the entire cycle of forward and reverse sweeps. The greater the separation between the peaks for forward and reverse scans, the more irreversible is the electrode process [15]. Cyclic polarization (or "pitting scan") can determine the tendency of a material to undergo surface pitting or crevicing when placed in a specific corrosive environment. The resulting current-potential plot shows how readily the material will pit. If the reverse scan traces the same path as the forward scan in the region beyond the knee (the point where the current begins to increase very rapidly as the applied potential increases) the material has little tendency to pit. The pitting is indicated by repassivation of the pits during the reverse scan, causing a lower current at each potential point than during the forward scan.

Potentiostatic experiments can also be conducted to observe the long term stability of the films. The potential applied to the specimen is kept at a constant level and resultant current is plotted against time.

3.2.4 Chemical Analysis of the Surface Films

1- General Introduction:

Auger electron spectroscopy (AES) and x-ray photoelectron spectroscopy (XPS) were used to characterize the surface oxide and the semiconductor-oxide thin film interface. Thus this section will focus on AES and XPS to give some insight on the theoretical basis and to analyze the aluminum oxide film on Si.

The analytical methods for material characterization differ mainly by the type of probe used. These probes contain electrons, neutrons, atoms, molecules, ions and photons. The surface specific techniques involve the detection of low energy electrons (5-2000 eV) which are emitted or scattered from the surface inelastically [72]. A list of commonly used chemical analysis methods is presented in Table 3.1 [7]. Core electron energy levels are assumed to be unaffected by the fact that the atom is not free but in the solid surface. And therefore the surface analysis is made by choosing the appropriate method which will give the required surface information : chemistry, structure or general texture (Table 3.2).

A-Auger Electron Spectroscopy (AES)

1-Introduction:

AES is an analytical technique which provides qualitative and quantitative surface compositional analysis by measuring the energy distribution of Auger electrons emitted during irradiation with a beam of energetic electrons. It is sensitive to the first three or four atomic layers of the specimen surface and its sensitivity at a hundredth of a ML is remarkable for some materials. One of the advantages of Auger electron spectroscopy is its sensitivity to low mass impurities (except hydrogen and helium),

**Table 3.1: Chemical Analysis of Solids (Macrosamples- > 1 mg).
Components: Major(> 5 %), Minor(0.1 to 5 %), Trace(< 0.1 %).**

Major components	Minor components	Trace components
Alpha particle spec.	Alpha particle spec.	Alpha particle spec.
Auger spectroscopy	Atomic abs./fluores. spec.	Atomic abs./fluores. spec.
Combustion&gas analy.	Auger spectroscopy	Auger spectroscopy
Electron microprobe	Combustion&gas analy.	Combustion&gas analy.
Emission spec.	Electron microprobe	Electron microprobe
EPR spectroscopy	Emission spectroscopy	Emission spectroscopy
Fluometry	EPR spectroscopy	EPR spectroscopy
Gamma ray spec.	Fluometry	Fluometry
Infrared spectroscopy	Gamma ray spec.	Gamma ray spec.
Ion microprobe	Infrared spectroscopy	Ion microprobe
Ion scattering spec.	Ion microprobe	Mass spectroscopy
Mass spectroscopy	Ion scattering spec.	Neutron activation
Molecular weight analy.	Mass spectroscopy	NMR spectroscopy
Mossbauer spec.	Neutron activation	SEM
Neutron activation	NMR spectroscopy	X-ray fluorescence spec.
NMR spectroscopy	Optical microscopy	XPS (ESCA)
Optical microscopy	SEM	
Raman spectroscopy	UV/V absorption spec.	
SEM	X-ray absorption spec.	
Thermal analysis	X-ray fluorescence spec.	
UV/V absorption spec.	XPS (ESCA)	
X-ray absorption spec.		
X-ray fluorescence spec.		
XPS (ESCA)		

Table 3.2: Surface Analysis of Solids

Chemistry	Structure	Texture
Alpha particle spec.	Electron diff.(HEED)	Optical microscopy
Auger spectroscopy	Electron diff.(LEED)	Photoemission electron microscopy
Electron microprobe	Field ion microscopy	Profilometry (stylus)
Infrared spectroscopy	TEM	SEM
Ion microprobe		Topogrofiner
Ion scattering spec.		TEM
Mass spectroscopy		
Mossbauer spec.		
XPS (ESCA)		

such as carbon or oxygen, which are common contaminants at surfaces and interfaces. In this work it will be used to find the identity of the surface, and the bulk oxide film as well as the Al-oxide/Si interface. The presence of the native oxide layer (SiO_2) at the interface is unwanted for the purposes of this work.

AES, which was first suggested by Lander [41] for surface analysis, involves ionization of core levels by an electron beam with a typical energy of 2-3 keV and detection of emitted Auger electrons of discrete energy (5-2000 eV), characteristic of different elements present in the near-surface region of the sample.

A vacuum of at least 10^{-7} Torr is required when oxidized samples are to be studied. The energy shifts in the Auger peak positions and the shape of such peaks tell about the chemical state of the element, however this requires a highly resolved signal. Metals and semiconductors are suitable for Auger analysis. Insulators may also be examined, but due to surface charging, one needs special glancing incidence of the

incoming beam to lower the penetration depth and the charging effect. Auger analysis is generally a non-destructive technique. However, in some cases, (e.g. oxides) the electron beam may cause either thermal or electron stimulated desorption of some of the components at the surface [7].

A monoenergetic electron beam incident upon a solid generates large number of secondary electrons in the sample. Of this secondary electron spectrum defined as $N(E)$, only a small fraction (10^{-5}) will be the outcome of the Auger transitions whose signal is to be separated from a large background of secondary electrons. Figure 3.6 [17] illustrates the peak shifts for sapphire with respect to pure Al.

Characteristic loss peaks whose energy depends on the incident beam energy (E_p) are observed at energies ($E_p - E_b$) where E_b is the binding energy of an atomic electron [10]. Auger peaks are superimposed on the secondary electron background and rather difficult to discern in the $N(E)$ curve because of their low intensity. The derivative of $N(E)$ is, therefore, usually taken to pinpoint such peaks.

2- Theoretical Discussion:

Figure 3.7 [24] shows the Auger process, in which the atom is left in the final state with two vacancies (or holes). For vacancies created by the incident electron, say in the K-shell, the Auger process is triggered when an outer electron such as an L_1 electron fills the hole. The excess energy released can be captured by another L_1 or an L_2 electron which then has enough energy to leave the atom with an energy given by $E_A = E_K - E_{L_1} - E_{L_1}$. The transition is called KLL (or more precisely KL_1L_1). The most probable transitions allowing the Auger phenomenon are of the type KLL or LMM. However, one must note that other possibilities are observed. The case where the filling electron comes from the same shell (i.e. transitions of the type LLM) is

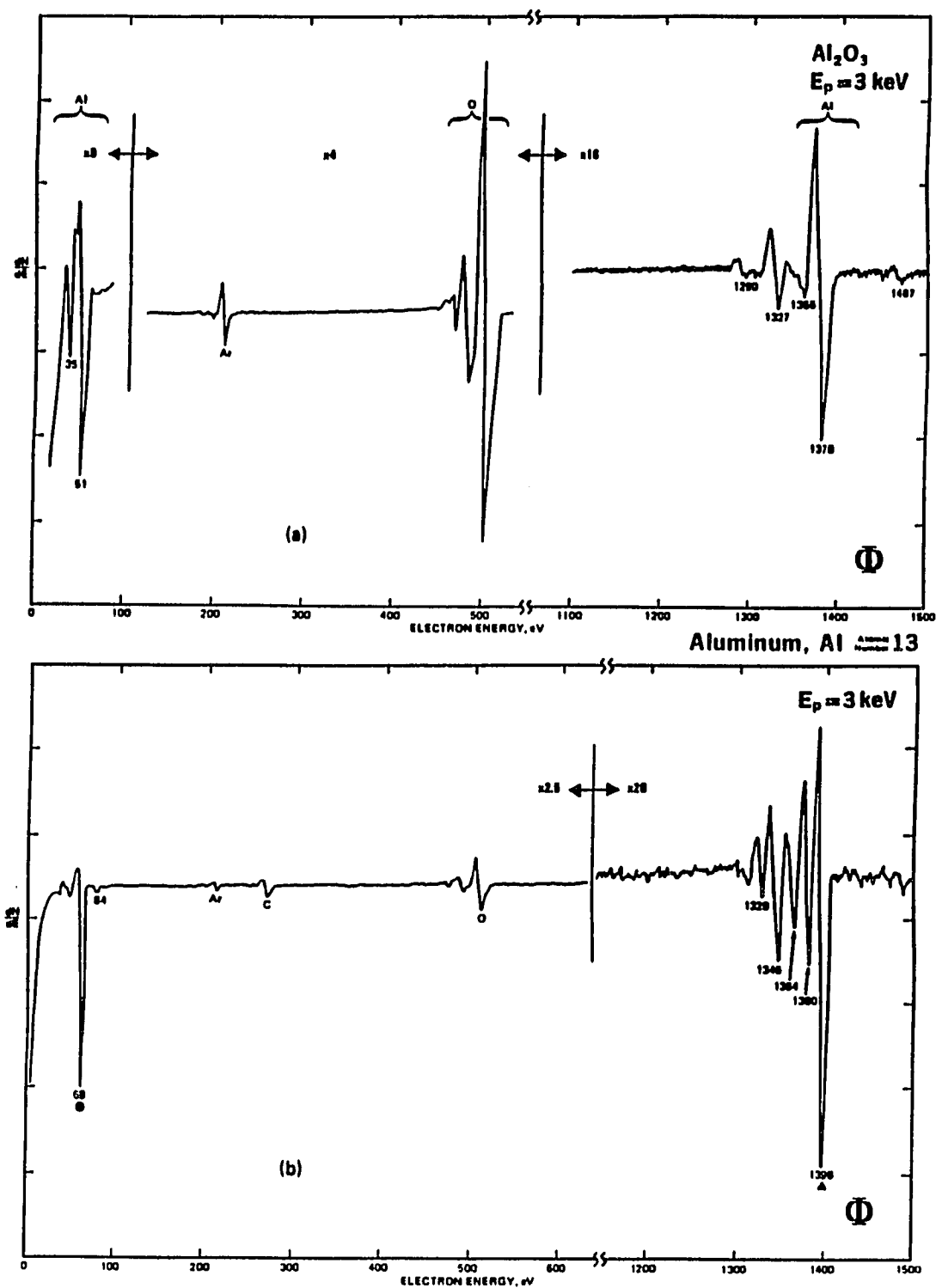


Figure 3.6: Comparison of the derivative spectra $dN(E)/dE$ for 3 keV electrons incident on a) oxidized Al, b) pure Al samples.

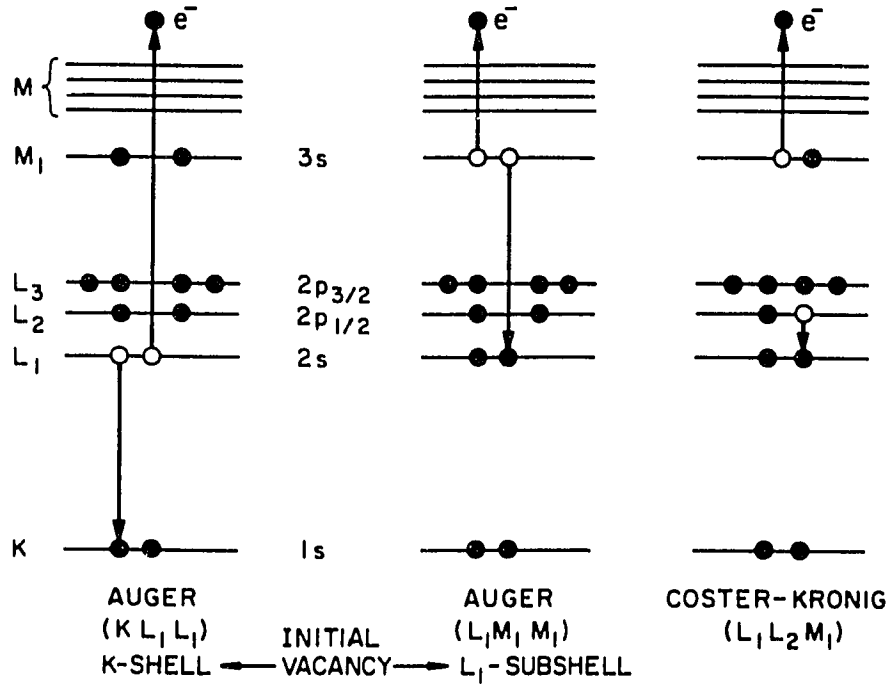


Figure 3.7: The process of Auger electron generation.

known as a Coster-Kronig transition. The transition rates are much higher than the normal Auger transitions and influence the relative intensities of the Auger lines. Auger electron energies may be calculated in principle as above, although in practice it is not always simple to identify observed Auger transitions unambiguously in terms of atomic energy levels. The observed energy $E(Z)$ of an Auger electron emitted from an atom of atomic number Z :

$$E(Z) = E_W(Z) - E_X(Z) - E_Y(Z + \omega) - \phi_a \quad (3.5)$$

where W is the shell from which an incident electron beam removes an electron, X is the shell from which an electron drops to fill the vacancy, Y is the shell from which the Auger electron is ejected, ω represents the correction for the extra positive charge of the singly ionized atom. As a first approximation, one would expect $\omega = 1$,

experimentally it ranges between $\frac{1}{2}$ and $\frac{3}{4}$ [8]. ϕ_a is the work function of the material from which the Auger analyzer is made. Auger electron energies encountered in AES range from 5 to 2000 eV. Although the exciting beam (2-3 keV) can cause emissions of Auger electrons from deep layers, these electrons will undergo subsequent inelastic scattering and thus will not contribute to the Auger peak. The observation depth is about 10-30 Å and is determined by the escape depth (the distance that electrons of a well-defined energy can travel without losing energy).

For a given incident beam current, the observed current associated with an Auger peak will depend on the Auger yield and the ionization cross section of the W shell. The Auger yield is the probability that an atom excited by removal of an inner electron deexcites by the radiationless Auger process. The Auger yield is essentially one for light elements ($Z < 15$) [31]. The ionization cross section rises rapidly from zero at the threshold where the beam energy is equal to the binding energy of the W^{th} transition level, to a maximum when the beam energy reaches 2- 3 times the binding energy, and for higher beam energies, the cross section decreases gradually [73].

The energy width of an Auger peak is generally the direct outcome of the uncertainty principle ($\Delta E = \frac{\hbar}{t}$). It is typically 10 eV (full width at half maximum-FWHM) for a transition time of 10^{-16} sec (lifetime for the hole). Broader peaks will be obtained for faster transitions or as a result of energy losses of electrons escaping from the sample. The widths of the atomic energy levels in the Auger transition increases with the increasing atomic number. For transition of the type WXV and WVV, where V denotes the valence band, the peak width will reflect the band structure of the solid. In the case of WVV transitions, the Auger peak width will be twice the width of the VB [3, 63].

The chemical environment of an atom is reflected in changes in the valence shell orbitals which in turn influence the atomic potential and the binding energy of the

core electrons. The K_{α} x-ray emission lines (due to $L \rightarrow K$ electron transition) have only small shifts with changes in the chemical environment. For KLL Auger lines, the inner shell electron ejected will display a chemical shift. Chemical shifts are evident in both AES and XPS spectra. However their interpretation is much easier in XPS since it is a one electron photoelectric process and XPS lines are narrower than Auger linewidths.

3- Instrumentation:

Electron spectroscopies are carried out under high vacuum conditions. Retarding field analyzer (RFA) and cylindrical mirror analyzer (CMA) are the two common Auger spectrometers which collect the electrons with an energy greater than the retarding voltage or with a narrow energy range ($dE/E = 0.5\%$), respectively [24]. Figure 3.8 shows the experimental apparatus equipped with a CMA which has an internal electron gun whose beam is focussed to a point on the specimen.

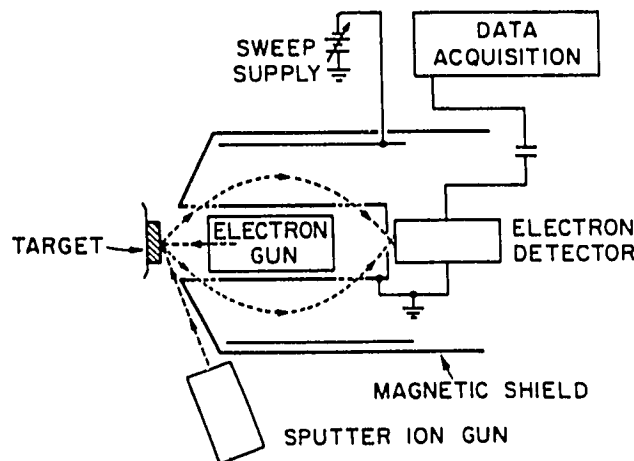


Figure 3.8: Experimental apparatus used in Auger spectroscopy.

Electrons ejected from the sample are directed to the electron multiplier. The pass energy, E , is proportional to the potential applied to the outer cylinder and the energy range of transmitted electrons is determined by the resolution.

The effect of background electrons can be reduced by electronic differentiation of the energy distribution [33]. The energy distribution has a relatively constant slope compared to the rapidly varying Auger peaks. Suppression of the background signal allows much higher gains to be used in the spectrometer electronics without overloading the amplifier. Electronic differentiation of the electron spectrum is accomplished by modulating the signal at an audio frequency and synchronously detecting the component of the spectrometer output at the modulation frequency [2]. This permits the reduction of the detection bandwidth and increases the signal to noise ratio.

Experimentally, a sinusoidal voltage ($k\sin\omega t$, $k \ll 1$) is applied to the analyzer so that the collected Auger current, $I(E)$, (10^{-11} - 10^{-12} A) is modulated in energy by $\delta E = k\sin\omega t$, where ω is the fundamental perturbing frequency of the phase sensitive detector. By monitoring the frequency while varying the applied potential to the analyzer, $N(E)$ vs E , a secondary electron spectrum is obtained. The differential energy distribution (Figure 3.6.a or b) can be obtained for the RFA by tuning the detector to the second harmonic of the perturbing frequency 2ω . As for the CMA, the differential energy distribution dN/dE is obtained by adjusting it to the perturbing frequency ω .

4- Quantitative Analysis:

Calibration of the spectrometer in terms of the amplitudes of observed Auger signals at known surface coverages for each species of interest is necessary. It is essential that the amplitude of the Auger peaks be known as a function of the surface concentration

of the emitting species. Weber and Johnson [70] verified the linearity of the intensity of the Auger signal to the surface coverage.

In most cases the method is only used for monitoring the chemical composition of clean and contaminated surfaces. The relative amount of a species on the surface is fairly simple to determine, because the emission current of Auger electrons is proportional to the number of excited atoms. If the Auger peak is Gaussian, then the peak to peak height, h_i , of the differentiated Auger line is proportional to the number of excited atoms, n_i , and this quantity is frequently used as a measure of relative surface concentrations [22]. Since the Auger current also depends on several other experimental parameters, such as the incidence angle of the primary electrons, primary beam energy, modulation voltage, etc., it is clear that the relative measurement is only applicable when all other parameters are held constant.

5- Depth Profiling:

A major use of Auger electron spectroscopy is determining the elemental concentrations in a direction normal to the surface as a function of depth of thin films and layered structures. The conventional apparatus illustrated in Figure 3.8 consists of an electron gun, a CMA assembly and a sputter ion gun to provide the layer sectioning.

A solid surface exposed to a beam of noble gas ions (Ar^+ , Ne^+ , etc.) is eroded with a sputtering rate r (cm/sec) given by [22] :

$$r = S \cdot \frac{j}{e} \cdot \frac{M}{\rho N_A} \quad (3.6)$$

where

S = sputtering yield (atoms/ion) which changes between 1-10 for the energy range commonly used 1-10 keV.

j = ion current (A/cm^2).

e = electron charge.

N_A = Avagadro's number.

ρ = density of target (g/cm^3).

M = atomic (or molecular) weight of target material.

By using $\rho = 3.96 \text{ g/cc}$, $M_{Al_2O_3} = 102 \text{ g/mole}$ in Equation 3.6, the theoretical sputtering rate for Al_2O_3 can be calculated as $(2.66 \times 10^{-4}) \text{ j S}$.

B- X-Ray Photoelectron Spectroscopy (XPS)

1-Introduction:

Photoelectron emission which was first clearly described by Einstein early in this century is now the most commonly used method to identify the atomic species at the surface of a solid by analyzing the kinetic energy of the photoelectrons.

Photons with energies of up to 10 keV interact with the atomic electrons primarily via the photon absorption process. Two sources of photons can be used : UV light for interaction with valence electrons, or x-rays for interaction with core electrons. Photon energies (10 eV-0.1 MeV) used to excite electrons of the surface atoms are shown in the energy spectrum of electromagnetic radiation (Figure 3.9). Thus the technique can be used both for chemical state studies of compounds (low energy photons) and elemental studies for composition determination (high energy photons). Photon induced spectroscopies have undergone a major advance due to the advent of

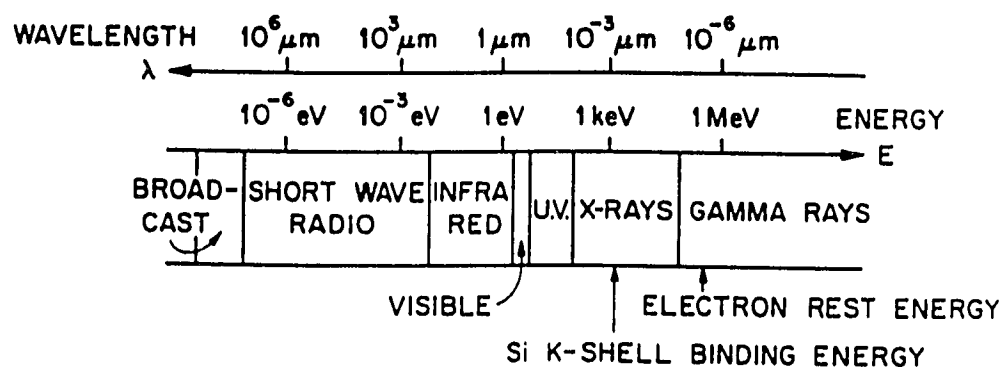


Figure 3.9: Electromagnetic spectrum indicating the region used for photoelectron spectroscopy.

electron synchrotrons which produce an intense source of monochromatic photons over a range of low energies (10 eV-50 keV).

The typical energy spectrum of x-ray excited photoelectrons generated by Mg $K\alpha$ (1.25 keV) exhibits sharp peaks and extended tails as shown in Figure 3.10 [69]. The peaks correspond to the energies of characteristic electrons which escape from solid oxide without undergoing energy loss. The higher energy tails correspond to electrons which have undergone inelastic scattering and energy loss on their outward path, thus emerging with lower kinetic energy (higher binding energy). Photoemission from p, d and f electronic states with nonzero orbital angular momentum would produce a spin-orbit doublet. The energy of the Mg $K\alpha$ radiation is sufficient to eject K-shell electrons (core electrons such as the 1s electrons) from Al_2O_3 . Therefore, the hole can be filled by an Auger process of KVV type.

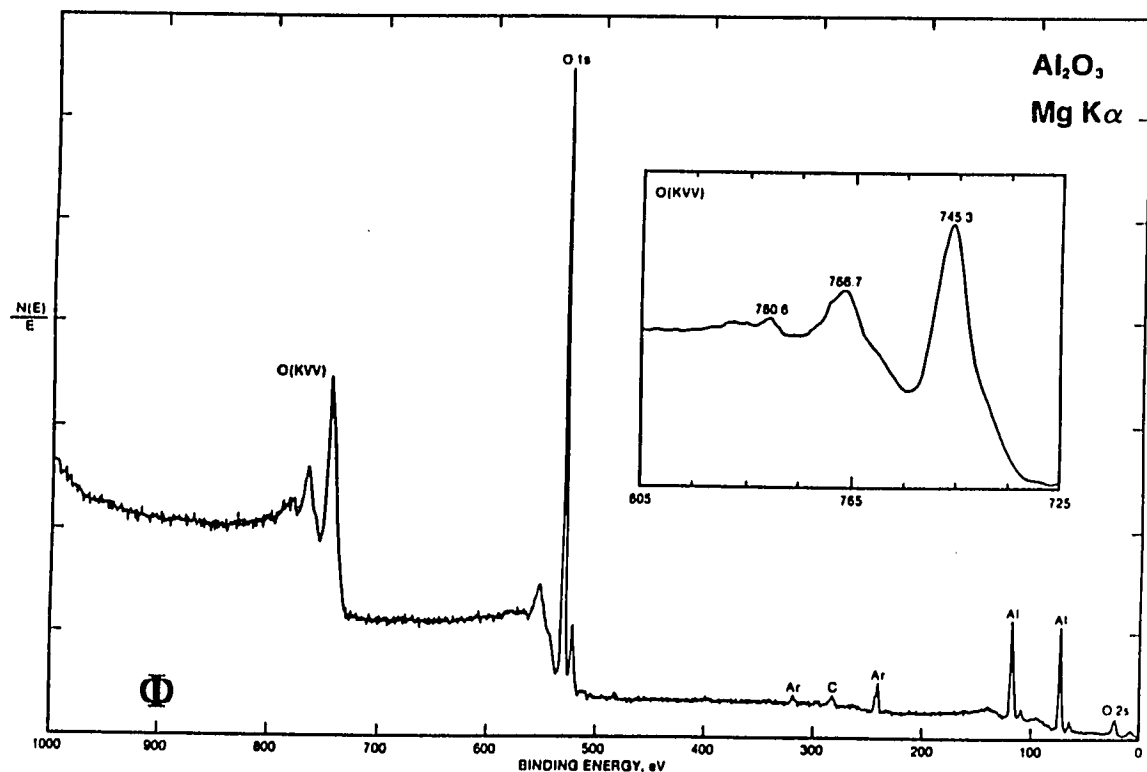


Figure 3.10: The energy spectrum of electrons from Al_2O_3 .

The energy of an Auger line is independent of the incident photon energy, while the energy of the photoelectron line varies linearly with the incident photon energy.

2- Theoretical Discussion:

The basic process in photoelectron spectroscopy is the absorption of a quantum of energy $h\nu$ (or $\hbar\omega$) and the subsequent emission of a photoelectron whose kinetic energy referenced to an appropriate zero of energy is related to the binding energy (E_B) of the electron in the target atom. In the process, the photon transfers its entire energy to the bound electron. The measurement of the energy of the escaping electron (without loss) permits the identification of the origin atom present in the sample. Energy conservation is written as :

$$\hbar\omega + E_{tot}^i = E_{kin} + E_{tot,K}^f \quad (3.7)$$

where E_{tot}^i is the total energy of the initial state, E_{kin} is the kinetic energy of the photoelectrons, and $E_{tot,K}^f$ is the final energy of the system after the ejection of an electron from the K^{th} level. The E_B of the photoelectron is defined as the energy required to remove it to infinity with a zero E_{kin} . In XPS, E_B of an electron in the K^{th} level with respect to the local vacuum level, $E_B^v(K)$ is defined as :

$$E_B^v(K) = E_{tot,K}^f - E_{tot,K}^i = \hbar\omega - E_{kin} \quad (3.8)$$

In analyzing solid samples, the conducting specimen and spectrometer housing are kept in electrical contact and thus have a common Fermi level. The resulting energy levels are given in Figure 3.11 for metallic samples. In passing from the sample surface into the spectrometer, the photoelectron energy will feel a potential equal to the difference between the spectrometer work function ϕ_{spec} and that of the sample ϕ_s . Thus, E_{kin}^1 , the electron E_{kin} created by photons of energy $h\nu$ (relative to the

vacuum level of the sample), is measured as E_{kin} inside the spectrometer analyzer:

$$E_{kin} = E_{kin}^1 - e(\phi_s - \phi_{spec}) \quad (3.9)$$

Thus the binding energy in a metallic sample may be determined relative to the common Fermi level according to :

$$\hbar\omega = E_B^F + E_{kin} + e\phi_{spec} \quad (3.10)$$

When analyzing insulating samples, one encounters difficulties brought about by the sample charging and the uncertainty in the location of the Fermi level within the band gap. One approach is to reference the energies to a well-defined feature of the electronic structure such as the VB edge which can be located in the XPS spectra. In this work, the shift from the position of the C(1s) line of unspattered inert metals (284.6 eV [69]) will be taken as equal to the static charge. Alternatively, a thin film of gold (or other metal) can be deposited on the surface and the energy scale can be defined by using one of the known Au core levels.

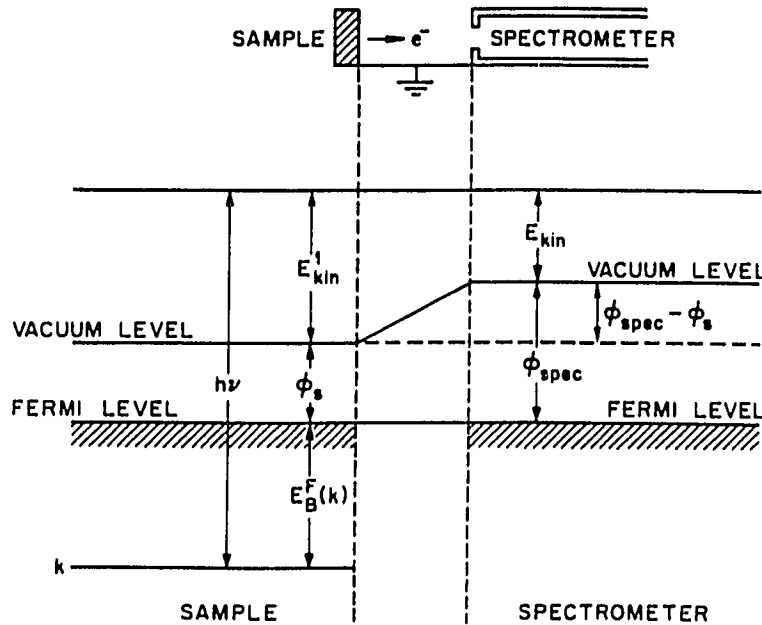


Figure 3.11: Schematic of the relevant energy levels for binding energy measurements.

3- Instrumentation:

Element identification is provided by the measurement of the energy of the electrons that escape from the sample without energy loss. As indicated in Figure 3.12, photoelectron spectroscopy requires both a source of monochromatic radiation and an electron spectrometer. As is common to all the electron spectroscopies where the escape depth 10-20 Å, careful sample preparation and clean vacuum systems are required. X-rays are produced at the Al anode by bombardment of electrons created at the filament. The x-rays impinge on a sample producing photoelectrons which are detected after analysis in the electron energy analyzer.

The energy of photoelectrons is determined by their dispersion in applied electrostatic or magnetic fields. There are two general operating modes for analyzers: Deflection (electrons travel along equipotential lines without any energy change, see Figure 3.12) and reflection (mirror) (electrons travel along equipotentials and are reflected away from the reflector electrode into the analyzer exit).

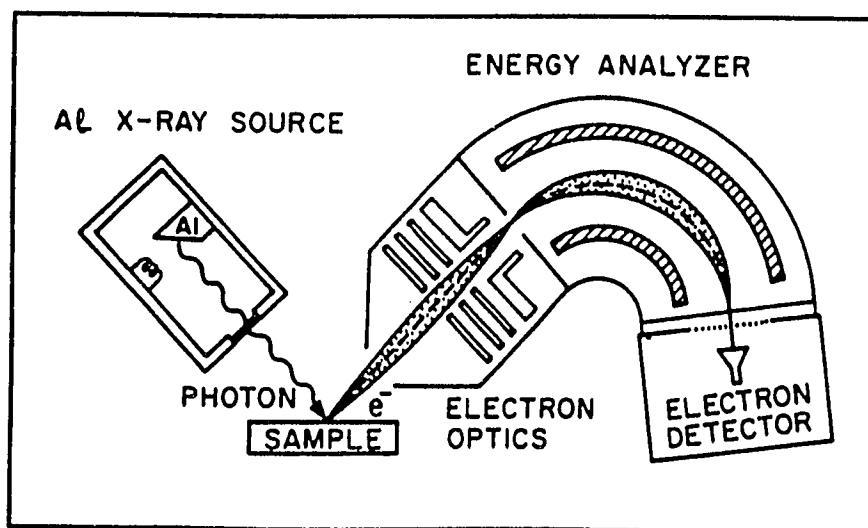


Figure 3.12: Schematic of the basic apparatus used in XPS.

A convenient source of characteristic x-rays (at fixed photon energies superimposed on a bremsstrahlung background) is provided by electron bombardment of Mg or Al targets where about one half of the x-rays produced are the $K\alpha$ rays ($K\alpha_1$ corresponding to $2p_{3/2} \rightarrow 1s$ and $K\alpha_2$ corresponding to $2p_{1/2} \rightarrow 1s$). For most applications, the spectrum is sufficiently clean for analysis purposes. If higher energy resolution is required in the photon source, a monochromator (narrows the excitation energy) must be used with a corresponding decrease in efficiency (lower x-ray intensity). Figure 3.13 shows a common type of mirror analyzer; a double pass cylindrical mirror analyzer (CMA) with angular entrance and exit slits. The deflection is caused by the potential difference (set by the analyzer control) between the inner and outer cylinder. The spherical retarding grids are used to scan the spectrum while the CMA is operated at a constant pass energy to maintain a constant energy resolution.

An electron multiplier of the channeltron type usually provides the gain for the detection of the energy-selected electrons. these channeltrons have a conelike opening and a continuous tube of high resistivity, semiconducting glass with a high secondary emission coefficient. A high electrical field is applied along the tube, and incident electrons create a shower of secondary electrons which in turn hit the tube walls and create further secondaries.

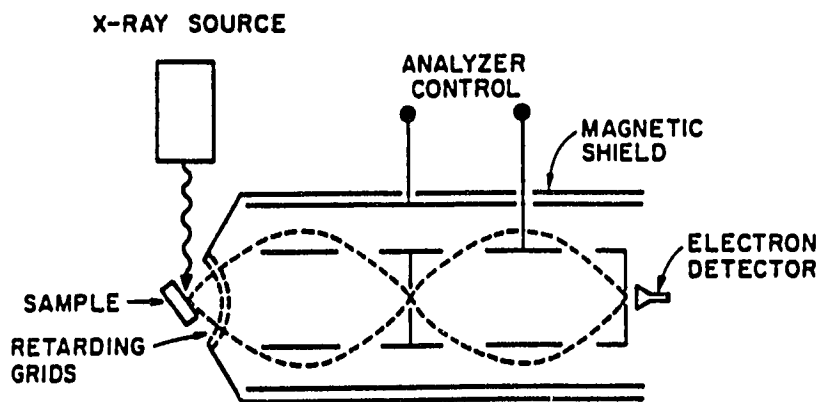


Figure 3.13: Schematic of a double pass cylindrical mirror analyzer used in photoelectron spectroscopy.

4- Binding Energy Shifts:

The exact binding energy for an electron in a given element depends on the chemical environment of that element. If a core level is considered, the energy of an electron in this core state is determined by the Coulomb interaction with the other electrons and the attractive potential of the nuclei. Any change in the chemical environment of the element will involve a spatial redistribution of the valence electron charges of this atom and the creation of a different potential as seen by a core electron. This redistribution affects the potential of the core electrons and results in a change in their binding energies.

Figure 3.14 [69] shows the binding energy shifts of the Al atoms in Al_2O_3 with respect to pure Al. The greater the electronegativity of the surrounding atoms, the more the displacement of electronic charge from the atom and the higher the observed binding energies of the core electrons. As the compound becomes richer in oxygen, the amount of Al atoms/ cm^2 contained within the escape depth for the

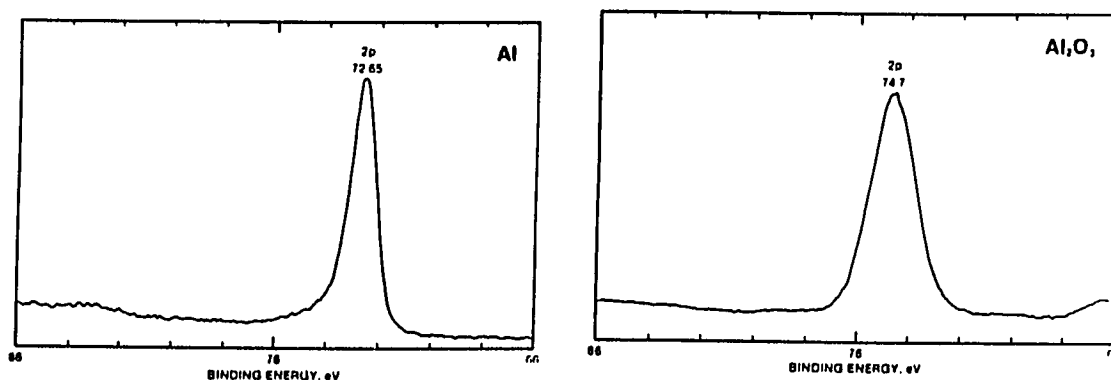


Figure 3.14: Al(2p) chemical shift in Al_2O_3 with respect to pure Al.

Al(2p) electrons decreases. This causes a lower peak intensity and in fact, this principle is used by the angle resolved XPS technique to determine the oxide thickness [32].

5- Quantitative Analysis:

The information to be extracted from an XPS spectrum concerns the energetic positions, intensities, and in certain cases, the shapes of the various peaks. The intensity of a given line (or the area of the photoelectron peaks) depends on a number of factors including the photoelectric cross section σ , the electron escape depth λ , the spectrometer transmission, surface roughness or inhomogeneities, as well as the presence of satellite structure which results in a decrease in the main peak intensities.

The flux of x-rays is essentially unattenuated over the depths from which XPS signal peaks originate because the absorption lengths of x-rays are orders of magnitude larger than the escape depth of the electrons. The probability, P , per incident photon for creating a photoelectron in a subshell k is [24]:

$$P = \sigma_k N t \quad (3.11)$$

where Nt is the number of atoms/ cm^2 in a layer of thickness t and σ_k is the cross section (ionization probability) for ejecting a photoelectron from a given orbital k .

The number of electrons that can escape from a solid without undergoing an elastic collision decreases with depth as $\exp(-x/\lambda)$, where λ is the mean free path. The number of atoms/ cm^2 that can produce a detectable photoelectron is then $N\lambda$ so that the probability per incident photon of creating a detectable photoelectron from a subshell k is given by :

$$P_d = \sigma_k N \lambda \quad (3.12)$$

Not all the photoelectrons from a given subshell contribute to the photopeak which corresponds to the ground state configuration for a single vacancy in an inner shell.

The influence of excited states (electron shakeup and shakeoff) is to decrease the intensity of the photopeak.

The photopeak signal production efficiency, Y (number of photoelectrons that contribute to the photopeak) can vary over values 0.7-0.8 for free atoms and, more importantly, can have a strong dependence on the chemical environment. The instrument's transmission efficiency, T , is a function of the electron kinetic energy and varies as E^{-1} .

In the quantitative analysis, one is generally interested in the relative concentration, $\frac{n_A}{n_B}$, of elements A and B in a sample, so that only the ratio of the areas of the lines (the intensity ratio $\frac{I_A}{I_B}$) is required. The composition ratio is given by :

$$\frac{n_A}{n_B} = \frac{I_A}{I_B} \cdot \frac{\sigma_B \lambda_B \cdot T_B \cdot Y_B}{\sigma_A \lambda_A \cdot T_A \cdot Y_A} \quad (3.13)$$

If the photopeaks are of close energies such that $\lambda_A \simeq \lambda_B$ and $T_A \simeq T_B$, and the photopeak efficiencies are about equal, then the composition ratio can be approximated by :

$$\frac{n_A}{n_B} \simeq \frac{I_A}{I_B} \cdot \frac{\sigma_B}{\sigma_A} \quad (3.14)$$

assuming that the sample is flat for maximum signal, homogeneous for representative surface sampling and has clean surface for better precision on composition calculation and chemical state determination.

The sensitivity to the detection of trace elements depends on the cross section of the element and on the background signal from other elements. Usually, elemental analysis in bulk samples can reach 1 part per 1000. XPS measurements are extremely sensitive to the presence of surface layers. One can detect as little as 0.01 monolayers of an element.

3.2.5 Summary

In this section, two of the most common techniques in surface analysis and thin film characterization were discussed. Based on the same principle, the use of low energy probes, they are both sensitive to the very first layers of the sample's surface. However the information given by each is different. AES is mostly sensitive to the intrinsic properties (energies) of the atom because it involves transition within the atom. The observable electron energy is the difference of level energies, therefore it carries information on atomic composition but very little information on the chemical states (bonds, electronegativity of the atom). XPS gives the binding energy of the electron and therefore, allows the determination of the exact chemical structure in which the observed atom exists. This relation of complementarity between the two techniques and their "simplicity" explains their popularity.

Chapter 4

Experimental Considerations

4.1 Anode Preparation

Heat treatment of UHV evaporated aluminum films on glass in an oxygen (dry O_2) atmosphere was unsatisfactory for producing good Al-oxide coatings for the purpose of PEC use. It is known that the formation of crystalline $\gamma-Al_2O_3$ begins at about 450°C-500°C at low humidity [35]. While in the presence of steam, $\gamma-Al_2O_3$ and rapid oxidation can be observed at 350°C. The temperature required for producing the desired thickness of oxide is very high, and the films thus produced are rough and non-uniform, resulting in a diffuse reflection. In addition, low temperature sputtered amorphous Al_2O_3 films (anodized Al like) were light absorbing ($n < 1.5$) and they become crystalline at 680°C showing the electron diffraction pattern of cubic $\gamma-Al_2O_3$ with negligible light absorption [35].

In the present case, the production of the oxides on Si requires low temperatures in order to avoid any Al-Si eutectic formation ($T_e = 577^\circ C$) or the diffusion of Si into Al (1.65 wt % (or 1.59 at %) Si dissolves in Al at T_e and 0.29 wt % (or 0.28 at %) Si dissolves in Al at 400°C) as it is noted in Figure 4.1 [67]. Al is, according to the lattice parameter measurements, insoluble in Si [61] and as the amount of Si in Al increases the electrical resistivity of the Al-Si alloy also increases. The oxide films were deposited on both Si and glass substrates by reactive evaporation technique as described below. The structure of the films mainly depends upon their formation temperatures and other deposition parameters coupled to the energetics of the oxide

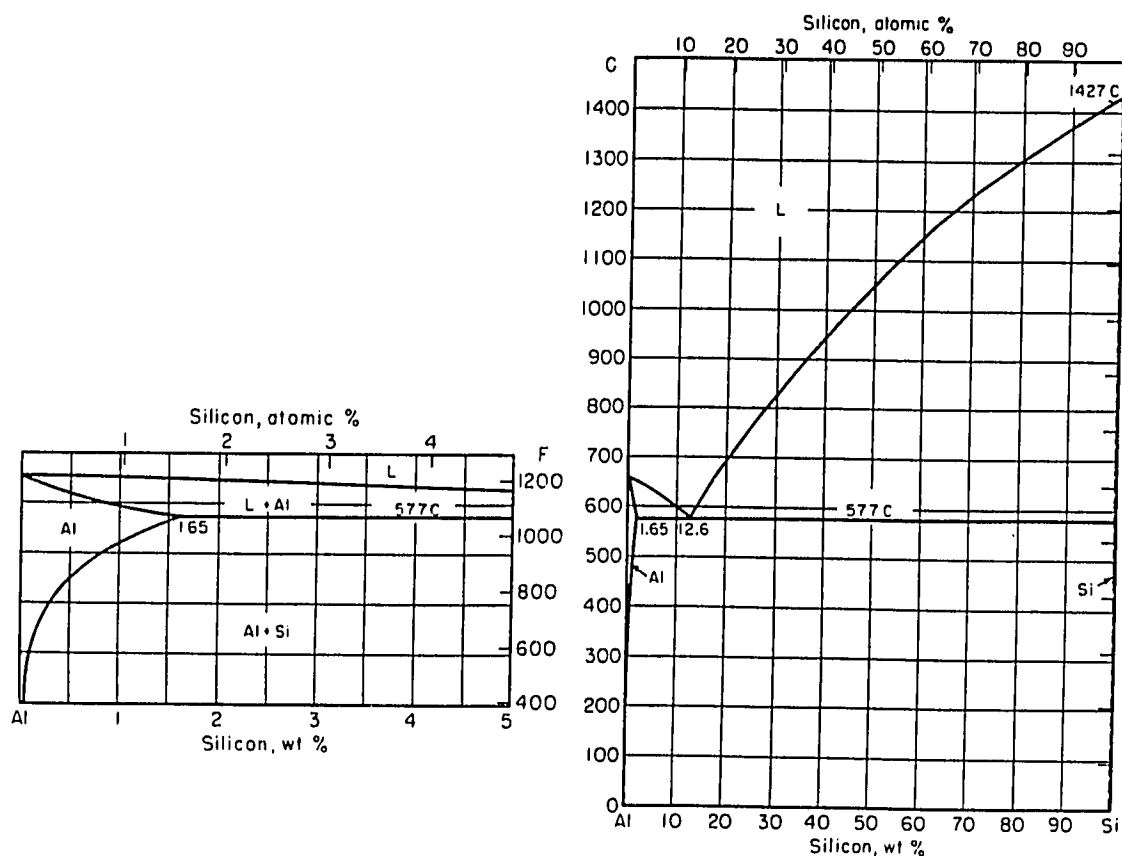


Figure 4.1: Al-Si phase diagram.

formation. A single crystal n-Si (P-doped) with (111) orientation, 5.08 cm diameter and 0.2-1.0 Ωcm resistivity was obtained from Silica-Source Technology Corp. (Tempe, AZ). After the wafers of 0.2-0.27 mm thickness were degreased and cleaned, the coatings were deposited onto silicon. The same film composition was also applied on quartz slides (type 1 or type 2, mainly differ in their UV-absorption characteristics) during the same run in UHV, for spectral normal absorbance (or transmittance) measurements. The slides (type 2) were 0.16 cm thick and supplied by F.J. Gray & Co. (Jamaica, NY).

The uniformity and composition of the oxide films deposited in UHV conditions were characterized by AES and XPS and their surface topography were revealed by SEM and electron microprobe (EPMA). The optical transmission spectra of the

films on glass slides were obtained by spectrophotometric means and the electrode performances for H_2 production were also tested by using a PEC cell.

4.1.1 Reactive Evaporation Technique

Thin films can be prepared by chemical methods (e.g. electrolytic deposition, anodic oxidation, and chemical vapor deposition (CVD)) or physical methods (e.g. vacuum evaporation, sputter plating, ion cleaning). Physical methods result in the formation of very pure and well-defined films. They are also applicable to many substances and to a great range of thicknesses [21].

Al_2O_3 with a melting point of $2052^\circ C$ [16] is very difficult to vaporize except by electron bombardment heating (also called electron-beam deposition). The vacuum evaporation method used in the photoelectrode coating process was reactive evaporation. Reactive evaporation, or evaporation in which a chemical reaction takes place, is most often used to produce oxidized coatings. The vacuum deposition method permits film thickness to be controlled with sufficient accuracy.

In general, the more thermally stable the substrate, the more readily it may be coated. Semiconductors and crystalline materials, unless they are water soluble, can be satisfactorily optically coated. As a rough approximation, the vapor or decomposition pressure at the surface of a substrate should be less than 10^{-3} Torr at $\sim 35^\circ C$ for a vacuum stable substrate. Si and quartz slides were successfully used in this work as stable substrates. Before the deposition of films, thick films usually, the substrates were preheated to ensure adhesion of the deposited layer without extensive reaction at the interface.

The evaporation process can be outlined as follows. Al vapor is generated by heating the material placed in an alumina crucible to a temperature such that the vapor pressure significantly exceeds the ambient chamber pressure and produces sufficient

vapor (from a liquid phase in many cases) for practical deposition. At the same time, oxygen gas is directed to the substrate surface to react chemically with the aluminum vapor on the surface. Direct resistance heating is used to produce deposits of high vapor pressure materials or to produce thin coatings. The evaporant is in the electrically neutral state and is expelled from the surface of the source at thermal energies of around 0.2 eV. The position of the substrates is important for uniform coatings, because the vapor flux from the source is localized and directional.

Evaporation is a surface phenomenon, and does not necessarily constitute boiling. Surface evaporation occurs from conduction (not from formation of subsurface vapor bubbles) if the liquid has sufficient thermal conductivity. The rate of arrival at the substrate, assuming that none of the vaporized material returns to the source, is given by the Langmuir equation [35]:

$$r = 0.0585P\left(\frac{1}{MT}\right)^{\frac{1}{2}} \quad g/cm^2s \quad (4.1)$$

where P is the evaporant's vapor pressure in Torr, M is the molecular weight of the evaporating material, and T is absolute temperature of the source. The evaporation rate for Al (e.g. sample B) can be calculated as $4.88 \times 10^{-10} g/cm^2s$ by taking $P_{Al} = 1.6 \times 10^{-6}$ Torr, $T_{Al} = 1090^\circ C$ in the equation above. The highest quality deposits are made on surfaces nearly normal to the vapor flux. Such deposits faithfully reproduce the substrate surface texture. The source and substrate configuration can be found in Appendix A.

Refractory crucibles used as the evaporation source accomplish heating through radiation and conduction. They are used for the metals that interact minimally with the evaporant. The use of alumina crucibles for Al evaporation contaminates the evaporant with oxygen [35], however, since the evaporant is to be intentionally exposed to oxygen, the use of alumina as the crucible material is acceptable. However, for pure Al deposition, boron nitride crucibles are preferred.

During reactive deposition, a careful balance must be maintained between metal vapor and oxygen arriving at the substrate at any given substrate temperature to ensure that repeatable stoichiometry in the films is achieved. The substrate temperature must be maintained high enough to ensure the desired degree of reaction, but not so high as to result in diffusion into the film during deposition.

4.1.2 System Description

Configuration of The Deposition System

An ultra high vacuum (UHV) deposition chamber (31 cm diameter, 1.4 m high) (Figure 4.2) was designed and built incorporating the usual gas leak facilities and a thickness monitor with controller. A sample holder (Figure 4.3) was designed to be able to resistively heat and degas the Si wafers (2.54 x 1.26 cm) before the deposition and to obtain temperatures up to 900°C before or during deposition. The substrate temperature was measured by use of a K type thermocouple whose wires were spot welded onto a 0.076 mm thick tantalum foil held between the wafers and a mica block. Ta was chosen because of its high melting temperature, low oxygen reactivity and lack of diffusion through silicon. The thermocouple feedthrough allowed both surface temperature measurement and substrate heating through two 0.6 cm diameter Cu rods screwed to the Cu blocks through Cu wires shown in Figure 4.3. A stainless steel rod was threaded on one end to be connected to the mica block, and the other end is fastened to the sample holder feedthrough.

The system allowed for sample rotation to face either the top window for observation or the Al source (25.4 cm from the sample surface) for deposition. It was designed such that two specimens could be produced in one vacuum run. The source was obtained by resistively melting 99.999 % pure Al metal in an alumina boat. In order to reduce the oxidization of the source, the majority of substrates were dosed

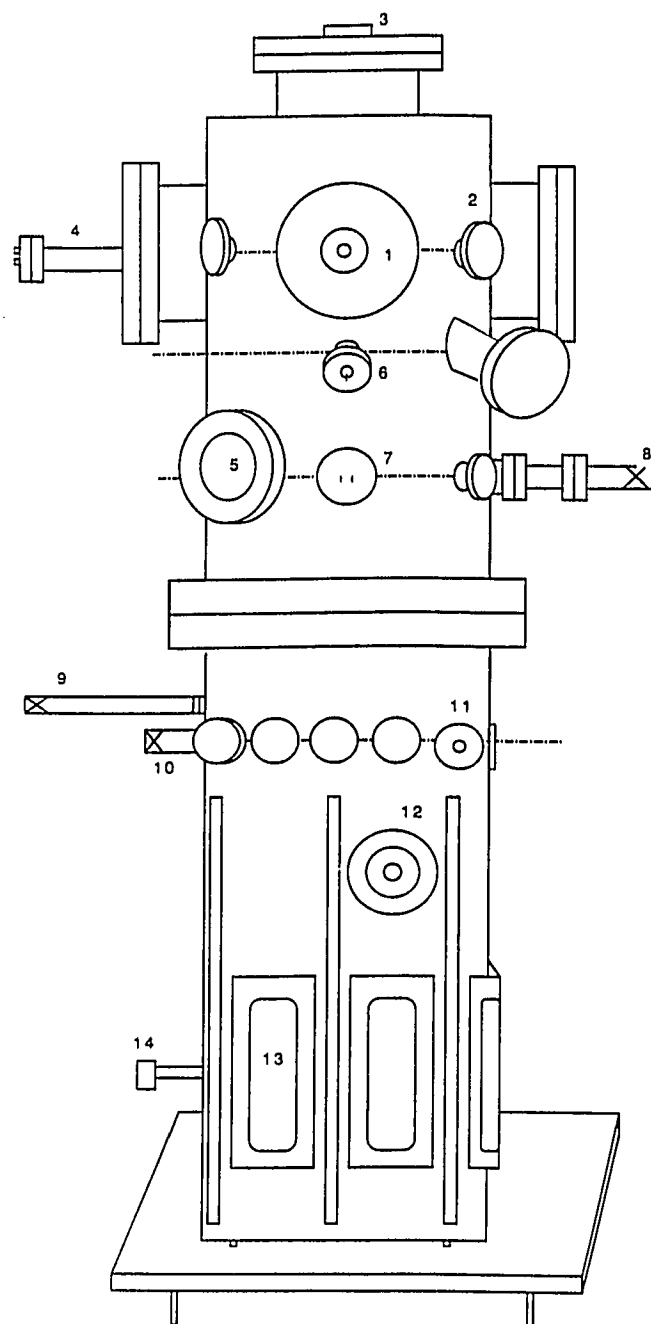


Figure 4.2: UHV chamber designed and built for the reactive evaporation process.

1- Sample holder. 2- Shutter, 3- Top window, 4- Quartz crystal holder, 5- Side window, 6- T/C feedthrough. 7- Source, 8- Oxygen leak, 9- Adsorption pumps, 10- (RGA), 11- Ionization gauge, 12- Poppet valve, 13- Ion pumps. 14- TSP.

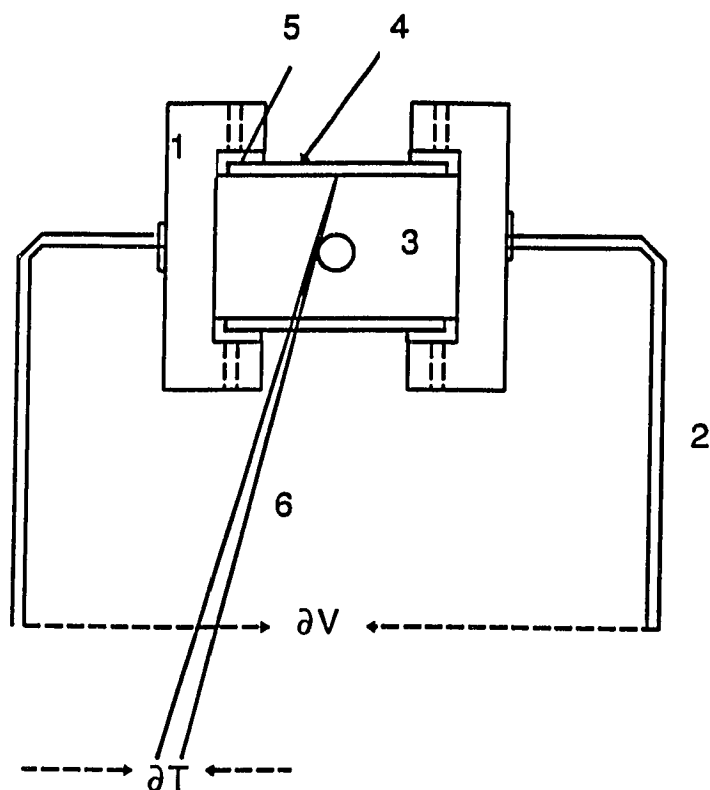


Figure 4.3: The apparatus for holding and resistively heating the substrates.

1-Cu blocks (grips), 2- Cu wires, 3- Mica block (insulation), 4- Substrate, 5- Ta foil (for sample heating), 6- T/C wires.

with oxygen during film deposition. This dosing process occurred through a 3.175 mm diameter stainless steel capillary tubing welded at one end to a blank flange between the chamber and the leak valve. A manifold (Figure 4.4) which achieved a reasonably high vacuum allowed the extra dry pure oxygen gas to be purged into the chamber through a Varian variable leak valve. The manifold was controlled by three other valves as also shown in the figure. The oxygen pressure at the level of the doser was also monitored by a thermocouple (T/C) gauge tube threaded to a blank flange.

An evaporation shield was included to control the deposition. The ion pump and titanium sublimation pump (TSP) system consistently achieved an indicated base

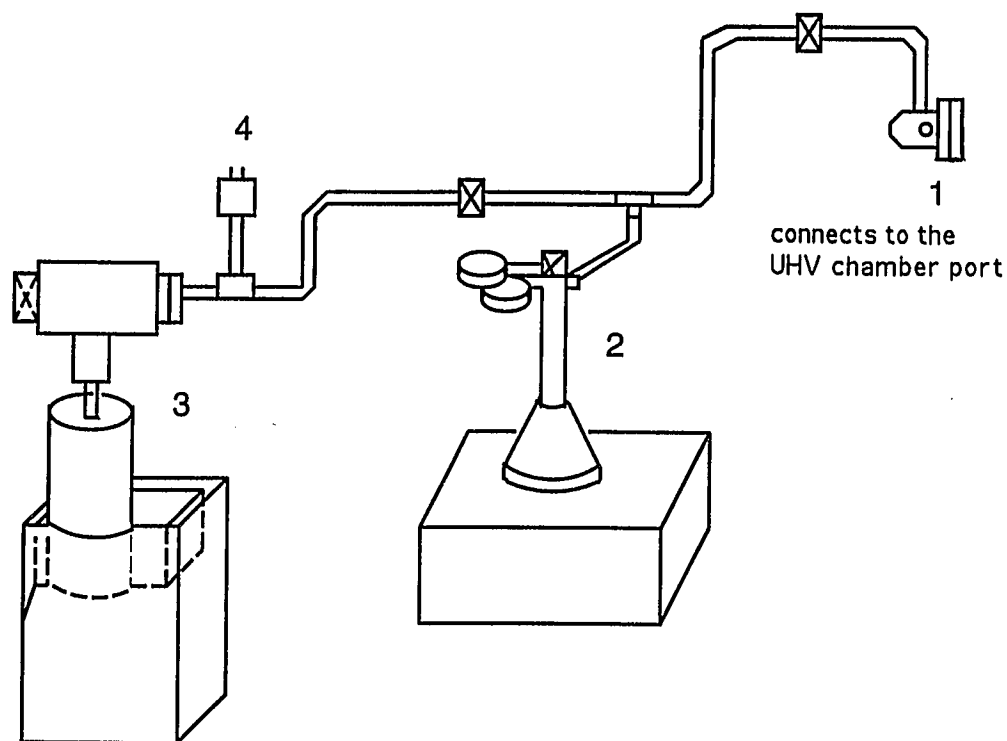


Figure 4.4: Oxygen leak manifold for reactive evaporation.

1- Variable leak valve, 2- Oxygen bottle, 3- Rough pump, 4- T/C gauge.

pressure of 1×10^{-9} Torr after thorough outgassing, measured by a dual range ionization gauge.

The film thicknesses were monitored with a Leybold-Inficon Inc. Model XTC Single Film Monitor and Controller. A thickness monitor, or quartz crystal oscillator, utilizes the piezoelectric properties of a quartz crystal, where an AC field induces oscillations in the crystal whose temperature-dependent resonant frequency changes with the deposited mass and its elastic properties. The surface of the quartz crystal wafer is plated with gold for electric field application and the sensor is water cooled.

4.1.3 Coating Process

Surface Preparation

Very smooth and clean substrates were required for good film transparency with optimal conductivity. n-Si substrates came in 5.08 cm diameter wafers packed under air, therefore a thick layer of oxide was present on the surface. n-Si(111) and p-Si(100) single crystal wafers were cut into 2.5 by 2.5 cm pieces cleaned by following the degreasing (A,B,C), oxidation (D) and oxide removal (E) steps repeated at least three times as shown in Table 4.1.

Quartz slides (2.5 x 1.25 x 0.16 cm) were ultrasonically cleaned in 50 % HNO_3 + 50 % HCl mixture for 20 minutes and then rinsed with acetone to be used as substrate materials for the optical measurements. Having rinsed with deionized water and air dried, they were placed in the chamber and annealed at temperatures above 540°C for 30 minutes in UHV (1×10^{-9} Torr background pressure obtained with the combination of ion pumps, baking and TSP) before any deposition. The temperature was then decreased at a rate of $20^\circ\text{C}/\text{min}$ to allow for surface stabilization and to reduce the chance of creation of thermal defects.

For the baking process, 2.54 cm wide 576 Watts fiberglass heating tapes were wrapped around the chamber and the chamber temperature was regulated around 120°C for 20 hours. After thorough degassing of the source and substrates, the substrates were brought to the temperature of deposition and the coating process was initiated.

Deposition Process in UHV

Heat treatment of UHV evaporated aluminum films on glass in an oxygen (dry O_2) atmosphere was unsatisfactory for producing good Al-oxide coatings for the purpose

Table 4.1: The Surface Cleaning Procedure Used For n-Si, p-Si Wafers

Chemical Used	Treatment
A <i>Trichloroethylene</i>	1 min boil, 5 min water rinse
B <i>Acetone</i>	1 min at RT, 5 min water rinse
C <i>Methanol</i>	1 min boil, 5 min water rinse
D $HNO_3 / H_2O / H_2O_2$ (5 : 1 : 1)	5 min boil, 5 min water rinse
E HF/H_2O (1:10)	1 min at RT, 5 min water rinse

of PEC use. For example, sample A, see Table 4.2, showed a granular layer on the glass substrate after it was treated in oxygen gas for 1 hour at 350°C. Therefore reactive evaporation was an appropriate method for electrode processing. The oxide coatings were deposited onto Si as well as on quartz slides during the same run in UHV. In the reactive evaporation method where the substrates were heated, the four predominant deposition parameters were thickness (t), oxygen pressure (P_{O_2}), deposition rate, and substrate temperature (T_s). The aluminum source was outgassed slowly (1 amp/min) by annealing in vacuum several times before deposition. The evaporation speed was controlled by the output voltage of an AC power supply that changes the temperature of the source. A pressure between 10^{-9} - 10^{-10} Torr was achieved prior to deposition following baking and degassing of the substrate and source. In order to reduce the formation of SiO_2 at the interface, 20 Å of Al was deposited onto the heated Si wafers before introducing any oxygen to the chamber. T_s was kept less than the temperature (577°C) necessary to prevent any possible Al-Si eutectic formation. Before oxygen was allowed to enter the system at various pressures 8×10^{-7} - 10^{-1} Torr, the poppet

valve between the working and pump chambers was throttled to control the vacuum level.

Al was evaporated at a rate of 0.1-2.5 Å/sec in O_2 atmosphere until the desired thickness was obtained. Deposition was terminated by shuttering the sample from the source. To obtain highly transparent films, it was necessary to purge the chamber with oxygen having a pressure greater than 10^{-6} Torr. This, however, resulted in the oxidation of the source aluminum in the alumina boat before it would evaporate onto the substrate (eg. sample 10, 14 as specified in Table 4.2). The remedy was to dose the substrate with oxygen instead of exposing the whole chamber to the oxygen gas. The dosing process was successfully applied for the oxygen pressures below 1×10^{-4} .

Care was taken to slow cool the sample after the deposition was complete in order to reduce the effect of residual stresses. The temperature was decreased in a progressive manner ($60^\circ\text{C}/\text{min}$) to stabilize the interface and minimize local stress. A series of specimens with differing deposition parameters, see Table 4.2, were made using the procedure outlined above. Then, their optical, surface morphological and chemical properties were characterized to relate the nature of the surface oxides to their performance in a PEC cell.

4.2 Surface Morphology

Scanning electron microscopy (SEM), another technique based on electron bombardment of specimens and collection of the outgoing electrons, was also used to look at the surface pinholes (if any) and film continuity during this study. The energy of the bombarding electrons is increased above that used for Auger analysis for deeper penetration. Micrographs from the photoelectrodes numbered as 8, 10, 11B, 12B, 20B and 21B were observed using a JEOL (JSM 5300) scanning electron microscope at 25 kV electron beam using normal incidence.

Table 4.2: Samples Processed by the Reactive Evaporation Technique in UHV.

sample	Ts (oC)	substrate	degas T (oC)	rate (Å/sec)	PO2 (Torr)	thickness (Å)	comments
A	RT	glass	–	1.00	3x10-8(Al)	1000.00	1 hr in O2 at 350 oC-pores
B	700	p-Si(111)	800	0.16	1x10-5	740.00	AES
C	450	p-Si(100)	800	0.16	1x10-5	740.00	AES
D	404	p-Si(100)	–	1.00	3x10-5	454.00	Ni-foil melts on Si, AES
E	472	p-Si(100)	–	0.50	1x10-5	502.00	Ni-foil melts on Si, AES
1	350	p-Si(100)	–	0.20	2x10-5	320.00	clear
2	430	p-Si(100)	–	1.00	4x10-6	477.00	brown, XPS
3	430	glass	–	1.00	2x10-5	480.00	clear
4	380	p-Si(100)	–	0.50	1x10-5	320.00	dark bluish
5	350	p-Si(100)	–	0.15	1x10-5	50.00	
6	310	p-Si(100)	740, 40 min	1.19	1x10-7	460.00	AESDP, purple
7	303	p-Si(100)	740, 40 min	0.89	8x10-7	450.00	black
8	350	p-Si(100)	860, 40 min	2.00	1x10-6	510.00	AESDP, black
9	453	n-Si(111)	860, 40 min	1.00	1x10-6	405.00	AESDP, purple
10	300	n-Si(111)	900, 1 hr	0.25	<1x10-4	30.00	Si cracked, mica erosion
11A	330	glass	540, 1 hr	0.55	2x10-6	400.00	yellow
11B	305	n-Si(111)	540, 1 hr	0.55	2x10-6	400.00	navy blue
12A	310	glass	570, 1 hr	0.20	4x10-5	400.00	~clear

Table 4.2 Samples Processed by the Reactive Evaporation Technique in UHV (cont.).

sample	T-sub(C)	substrate	degas T(oC)	rate(Å/sec)	P(Torr)	thickness(Å)	comments
12B	325	n-Si(111)	570, 1 hr	0.20	4x10-5	400.00	milky white
13A	55	glass	640, 1 hr	0.20	2x10-7	400.00	425 oC-14 hrs, brownish
13B	55	n-Si(111)	640, 1 hr	0.20	2x10-7	400.00	brown
14	400	n-Si(111)	575, 1 hr	0.10	<4x10-5	75.00	clear
15	300	n-Si(111)	550, 30 min	2.50	3x10-1	273.00	brown
16A	300	glass	740, 30 min	0.60	7x10-4	400.00	
16B	300	n-Si(111)	740, 30 min	0.60	1x10-4	400.00	yellow-green
17A	300	glass	600, 30 min	1.00	1x10-6	350.00	
17B	360	n-Si(111)	600, 30 min	1.00	1x10-6	25+325	dark blue
18	250	n-Si(111)	600, 30 min	1.00 - 0.20	1x10-4	314	dark blue
19A	300	glass	550 C, 1 hr	0.10	1x10-4	1015	low %T
19B	300	n-Si(111)	550 C, 1 hr	0.30	1x10-4	220	dark blue
20A	350	glass	600 C, 1 hr	0.50	9x10-5	265	
20B	350	n-Si(111)	600 C, 1 hr	0.60	9x10-5	50	yellow-green
21A	230	glass	600 C, 1 hr	0.30	1x10-4	120	clear
21B	230	n-Si(111)	600 C, 1 hr	0.30	1x10-4	100	clear
22A	300	n-Si(111)	600, 40 min	1.00	3x10-1	170	clear
22B	200	n-Si(111)	600, 40 min	0.50	1x10-0	33	clear

The electrodes 12B and 17B grown in UHV conditions and then tested in a PEC cell were also ex-situ observed with a Princeton Gamma-Tech SX50-Camica type electron microprobe microanalysis (EPMA) system. The micrographs after the surface had polarized potentiodynamically in the aqueous electrolyte under illumination were obtained using 10 kV beam at normal incidence.

4.3 Optical Measurements

Aluminum oxide films of different thicknesses (120-1015 Å range) were deposited onto quartz glass substrates for optical measurements and calculations. Spectral normal absorbance and/or transmittance was recorded on the films backed by quartz slides. A Hewlett Packard diode-array spectrophotometer was employed in the 0.19-0.80 μm (UV= 190-380 nm, Visible= 380-800 nm) wavelength range.

A schematic diagram of a diode-array (single-beam) spectrometer is shown in Figure 4.5. A diode-array consists of series of photodiode detectors positioned side-

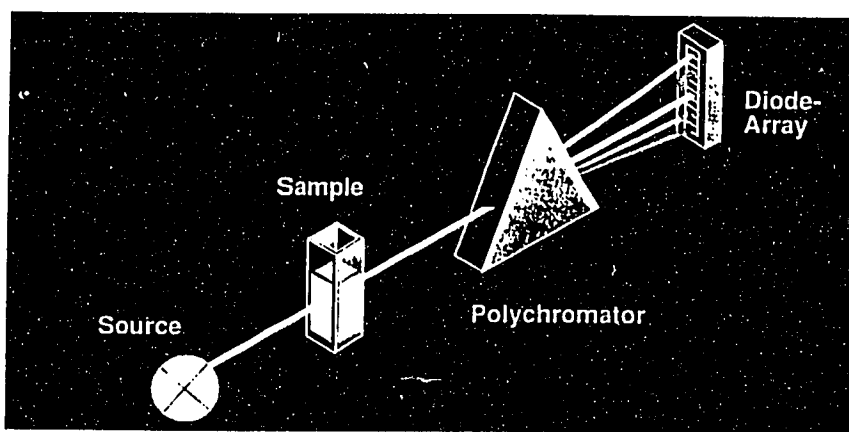


Figure 4.5: Schematic diagram of a diode-array spectrometer.

by-side on a silicon crystal. When photons penetrate into Si, free electrical charge carriers are generated to discharge the capacitor of each diode. The amount of charge needed to recharge the capacitors represents the number of photons detected by each diode, which is proportional to the light intensity. By measuring the variation in light intensity over the entire wavelength range, the spectrum is obtained. The polychromatic light source used is a deuterium lamp, and the sample is only illuminated during measurement to minimize the possible photoreactions.

Two types of glass substrates were used. Type 1 allowed 65 % or higher transmittance in 190-800 nm wavelength range and type 2 was the one with no transmittance for the wavelengths less than 300 nm. The incoming light first sees the film rather than the substrate so as to correspond to the real PEC configuration. The transmission spectra for both types of samples were taken separately. The films deposited on type 1 substrates were the ones numbered as 3, 12A, 13A in Table 4.2 and the ones on type 2 were 11A, 16A, 17A, 19A, 20A, 21A. Both substrates show almost the same (0.82 % difference) transmittance values for the wavelength range of 390-600 nm which will be used to compare the optical properties of all nine (9) films deposited onto glass slides.

4.4 Surface Chemical Analysis

The surface analysis of the oxides deposited in UHV was obtained with a Leybold-Heraeus XPS system. The XPS spectra were acquired on a spectrometer equipped with a hemispherical analyzer, using $\text{MgK}\alpha$ x-rays (2 kV, 20 mA). The pressure of the analyzing chamber was 1×10^{-9} Torr. Initially a survey scan was recorded for all films on Si to identify the elements present on the surface. Subsequently, the data was recorded over a narrow energy range to determine accurately the energy and shape of the strong lines (chemical states). The spectral acquisition and signal averaging were

recorded in a computer. Al(2p), C(1s), O(1s), and O(KLL) spectra were recorded. The peak position and full width at half maximum (FWHM) of the specific peaks were determined by a peak synthesis routine with Gaussian peaks. All peaks were referenced to the C(1s) peak at 286.4 eV for charging correction.

The samples were analyzed as-deposited in order to avoid any possible changes in surfaces. To ensure the accuracy of the data obtained, the calibration was checked by recording typically the Ag $3d_{3/2}$ and Ag $3d_{5/2}$ lines with a pass energy of 151 eV. The peaks are separated by 6 eV and the binding energies are different only by 0.03 eV from the data given in [69]. A Cu sample was also used in calibration of the peak energies and the results from the Ag standard were confirmed.

For the surface composition investigation, a broad survey spectrum was obtained first to identify the elements present and then the narrower detailed scans of selected peaks were used to identify the chemical states. Survey spectra were recorded with scan ranges of 0-1000 eV binding energy and analyzer pass energy of 100 eV to get an adequate resolution ($\Delta E \approx 2$ eV) with very high signal intensities, minimizing data acquisition time and maximizing elemental detectability. For the narrow scans, Al(2p), C(1s), and O(1s) lines were run in the respective order to minimize the charging effects on the spectra. XPS was run at Rice University (MEMS) for samples numbered as 8, 10, 11B, 12B, 13B, 14, 17B, 20B, 21B using MgK α radiation. However, the sputtering gun was not available at the time so only the elemental analysis was accomplished for the most part.

A synchrotron radiation study was also done on sample 12B at the National Synchrotron Light Source (NSLS) of Brookhaven National Laboratories, NY. The use of lower photon energy source (typically 120 eV vs 1253.6 eV Mg K α) pertain to a reduced number of accessible quantum energy levels, leading to shorter inelastic scattering mean free paths, thus enhancing surface sensitivity. Sample 12B was loaded

to the vacuum chamber and the surface was analyzed under 508 mA beam current in the ring. The as-deposited and corroded surface narrow scans, Al(2p) and Si(2p), were taken. Then the sample was sputtered for 5 minutes at 3 keV, 15 mA Ar ion beam with 5.5×10^{-5} Torr pressure. The sample current was measured to be $\sim 40 \mu\text{A}$.

AES was run for samples B, C, D, E, 6, 8, 9 at the Space Vacuum Epitaxy Center, SVEC of University of Houston. The AES chamber was equipped with an electron gun, a CMA assembly and a sputter ion gun. Also the depth profiles were obtained for samples 6, 8, 9. Samples were sputtered with Ar at the pressure of 2×10^{-4} Torr in the chamber. 3 keV beam energy, 26 mA beam current and 0.56 microampere sample current were typical. The ion beam was angled 45° to the sample surface. Immediately on completion of each sputtering period (~ 1 min), the chamber pressure was reduced to 10^{-8} Torr and survey data acquisitions were obtained and stored in the computer interfaced to the spectrometer.

4.5 PEC Measurements

Photoelectrochemical measurements combined cell photopotentials (E_{corr} vs time (t)) with cyclic polarization (I-V) and potentiostatic (I-t) techniques to evaluate the performance of the oxide films as protective coatings on narrow band gap semiconductor photoelectrodes. The data was first obtained for "naked" Si electrodes. Before each measurement, the uncoated electrodes were degreased and cleaned as explained in Table 4.1 and etched with HF for 10 minutes. Then they were rinsed for a minute with deionized water and air dried immediately before placing in the electrolyte. The electrode was placed on a copper disk (1.25 x 1.25 cm) soldered to a copper wire. The contact was provided to the back (unpolished side) of Si through conducting silver paint. Diffusion of Ag into Si at around 25°C was not expected.

Teflon was found to be one of the few materials that are compatible with H_2SO_4 . All surfaces exposed to the electrolyte were insulated with teflon (holder is shown in Figure 4.6) such that a Buna-O-ring (0.16 cm wall thickness and 0.95 cm OD) limited the active electrode surface to a circular area of 0.495 cm^2 which was exposed to the solution and light. The as-described arrangement was found to be leakproof. An aqueous solution of 1 N H_2SO_4 (13.36 ml acid/500 ml solution) was prepared with reagent grade H_2SO_4 and deionized water. Before and during the measurements, the solution was deoxygenized with Ar gas freed from oxygen and water by a gas purifier.

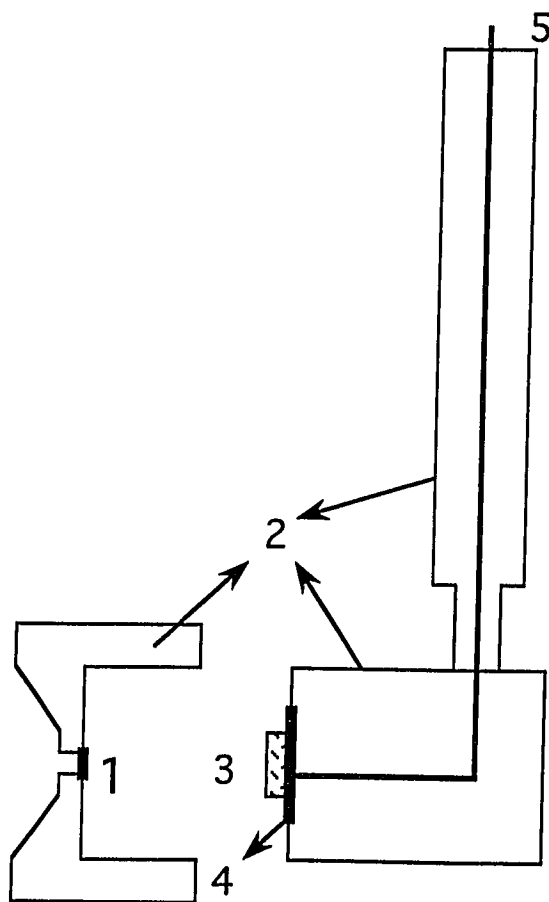


Figure 4.6: The holder for the photoelectrodes.

1- Buna O-ring placed in the cap, 2- Teflon cap and the holder, 3.81 cm dia cylinder,
3- Sample, 4- Cu disk, 5- Cu wire soldered to the disk.

All of the electrochemical experiments were conducted in a 1000 ml beaker which had a specially machined stopper (10.16 cm diameter) at the top to ensure accurate placement of the counter (wire-mesh Pt), the reference (SCE) and the working electrodes as well as the tubing through which the Ar gas was bubbled. The counter-electrode (cathode) was positioned as close as possible to the Si photoanode. Because of the small sample surface area and the configuration of the holder, some air was trapped between the electrode surface and the solution right after the electrode was placed into the solution. The remedy was found to syringe some amount of solution onto the electrode surface right before placing it into the solution. After the placement, the electrical continuity between the working electrode and the solution was checked. Each sample was immersed in 600 ml solution and a constant open-circuit potential was usually obtained within 30 minutes after the sample was immersed, and then the measurements were taken. For the reference experiments done on "naked" Si samples, stability and reproducibility in open-circuit potentials were achieved only when surface cleaning procedures, Ar bubbling, sample immersion time were tightly controlled.

Experimentally, potential is measured between the anode and a reference electrode and current between the anode and the cathode. The potential of the photoelectrode biased through the potentiostat was measured against a SCE ($E^\circ = 0.242$ V vs SHE for the reaction: $Hg_2Cl_2 + 2e^- \rightarrow 2Hg + 2Cl^-$). The photocurrent-voltage and the photocurrent-time data were taken using an EG&G Model 273 Potentiostat and the EG&G M342 software package. Cyclic polarization scans had a scan rate of 5 mV/s. The experimental arrangement is as shown in Figure 4.7. The electrodes were mounted on the holder and placed in the solution contained in the photoelectrolysis cell closely shown in Figure 4.8. The cell accepts the photons through an optically flat pyrex window placed on the face of the beaker. This leads to a reduced reflection

of the incoming monochromated light at the beaker surface and makes the focusing on the electrode surface easier.

The photoresponse of the samples B, 5, 7, 9 was measured using a 150 W Xe lamp light with an IR filter. The light for surface illumination was monochromated at 500 nm using a Pyrell Ash type monochromator. The rest of the samples were illuminated by a 3 mW/cm² He-Ne laser (10 mW max output) whose output light has a wavelength of 632.8 nm.

In this chapter the experimental considerations to produce a thin film coating were given to "protect" silicon electrodes from photocorrosion. The optical, chemical and PEC characterizations and discussions will follow next.

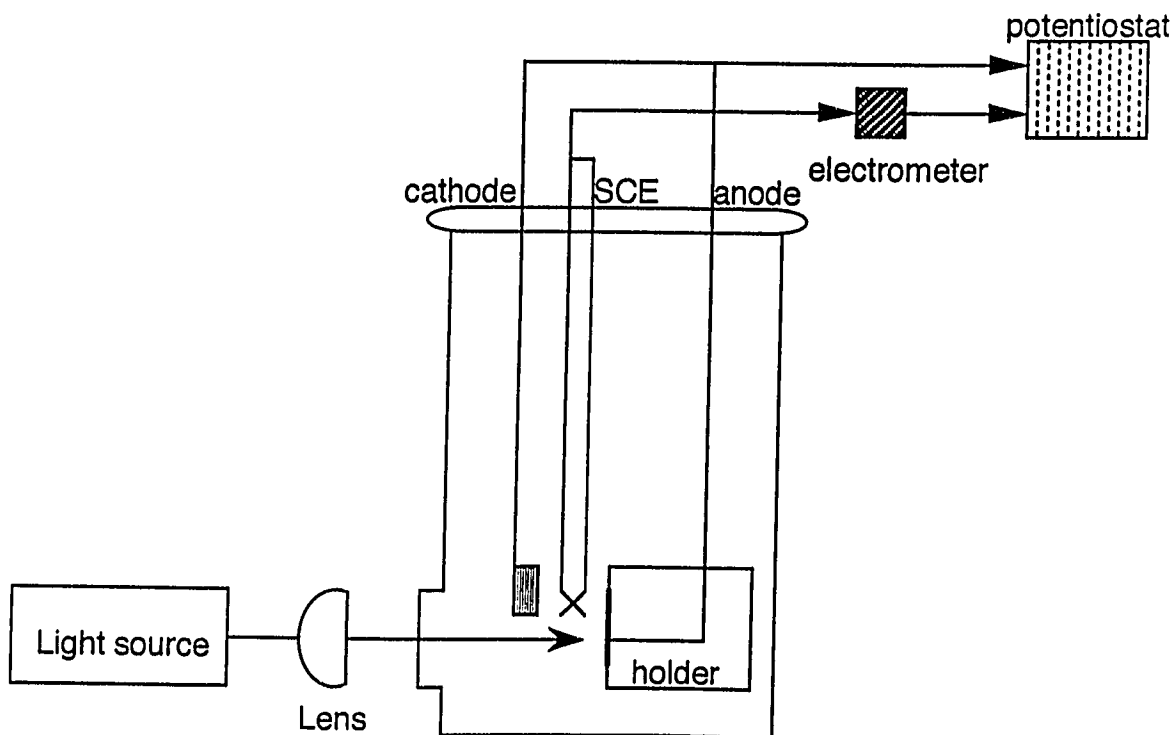


Figure 4.7: Experimental configuration for the PEC measurements.

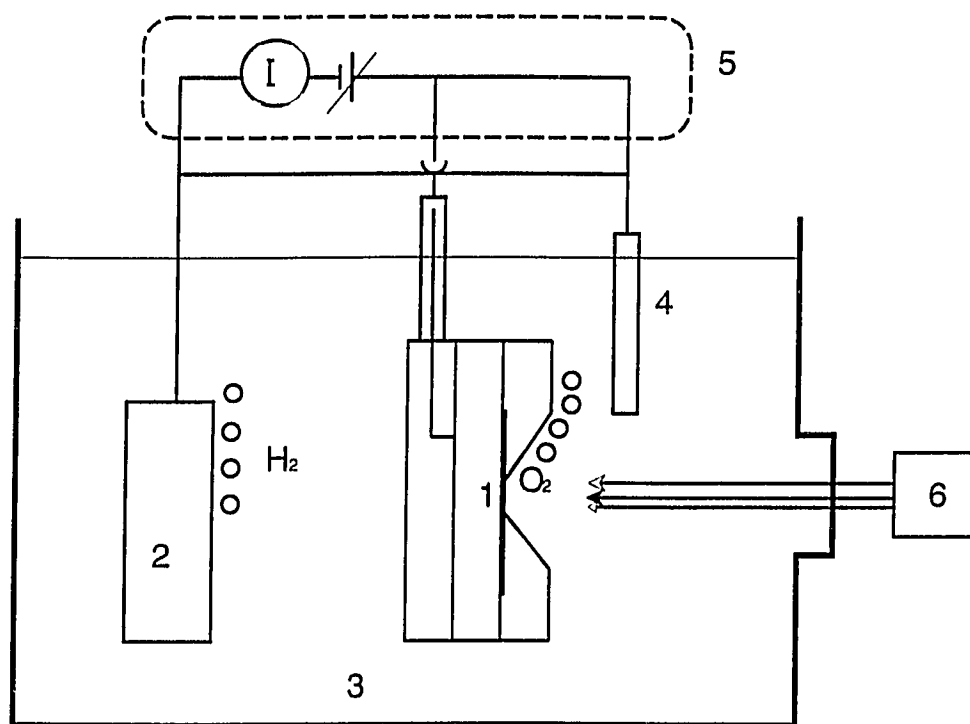


Figure 4.8: The photoelectrolysis cell to study the performance of the coatings in an illuminated aqueous solution.

1- Electrode (anode), 2- Pt electrode(cathode), 3- Electrolyte, 4- SCE, 5- Potentiostat, 6- Light source.

Chapter 5

Results And Discussions

5.1 Transmission Spectra of the Model Electrodes

The normal transmittance spectra of the aluminum oxide films backed by the glass slides are reported. Figure 5.1 shows the transmittance of the films on type 1 glass substrates. The spectrum numbered as 0 belongs to the naked type 1 glass (2.2 mm thick) slide and is given for the sake of comparison. Figure 5.2 gives the optical behavior of the model electrodes using type 2 glass (1.6 mm thick) which also allows UV light to pass through.

The two types of glass substrates can be considered having the same % transmittance values (~ 0.8 % difference) over the wavelength range of 390-600 nm so that the transmittance of the films can be compared. Figure 5.3 combines all nine spectra from the glass electrodes. It can easily be seen that samples 3, 11A, 12A, 16A, 17A, 21A are highly transparent in the UV-visible range and they can hardly be detected on the substrates by naked eye. For this group of samples, the films have transmittance values greater than 70 % over all the wavelength range.

The film specifications are given in Table 5.1 along with that of the glass slides for comparison. It also reports the normal optical transmittance of UV-visible light ($\lambda = 500 \text{ nm} = 50 \text{ \AA}$) which strikes the coating surface. % τ values were obtained by averaging over at least three measurements on each sample and % τ_n values were obtained by normalizing the transmittance values for the glass slides to 100. Therefore, % τ_n values reported may be taken as the transmittance of the films themselves.

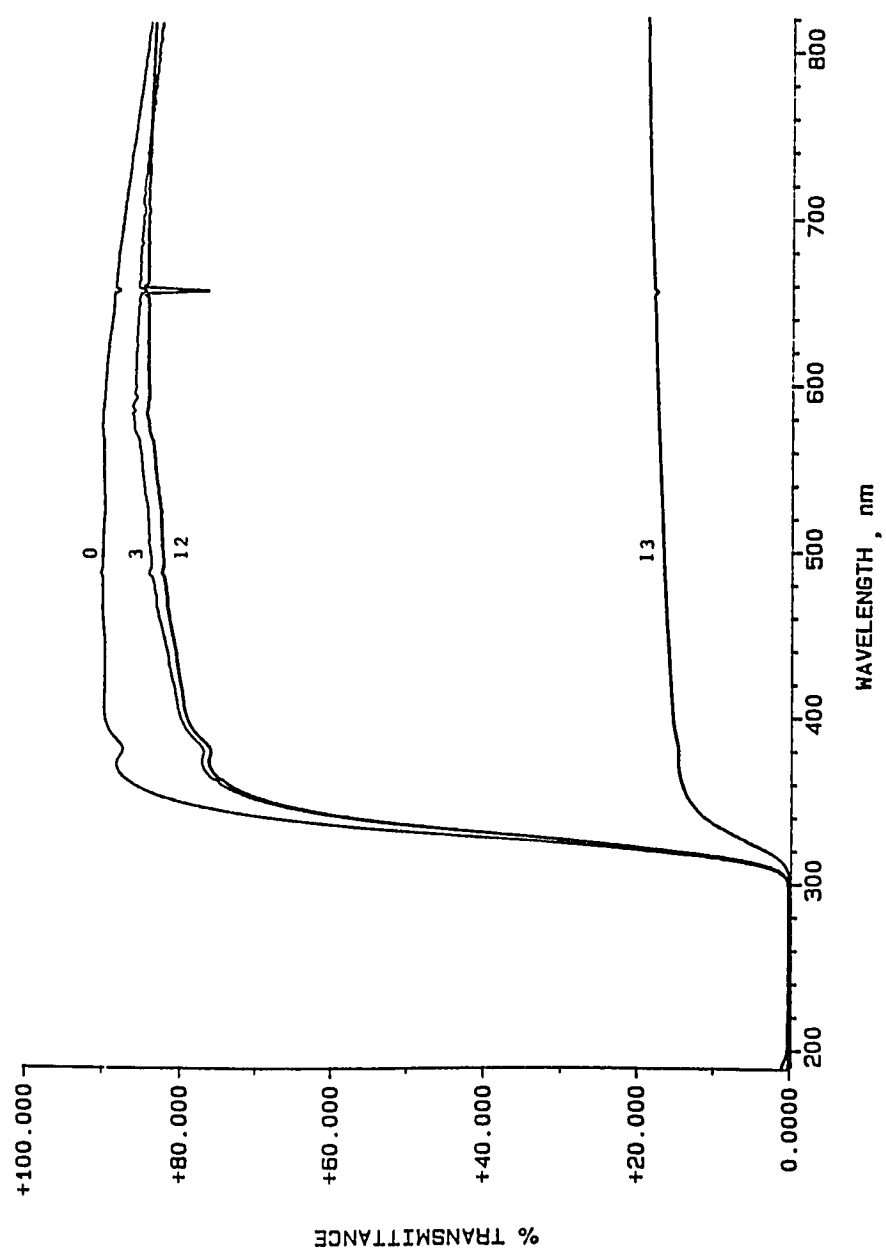


Figure 5.1: UV-visible transmittance of reactively evaporated Al-oxide coatings on glass slides- type 1.

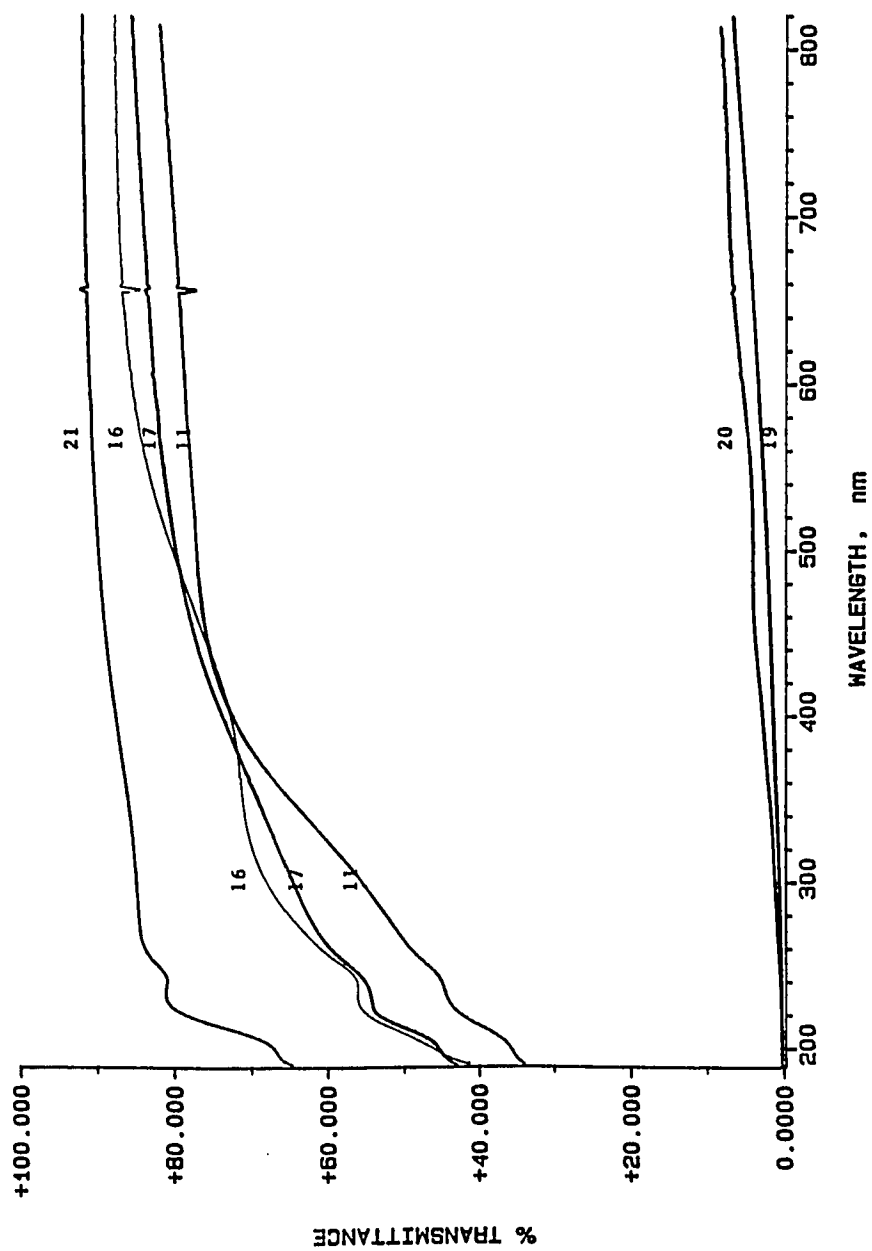


Figure 5.2: UV-visible transmittance of reactively evaporated Al-oxide coatings on glass slides- type 2.

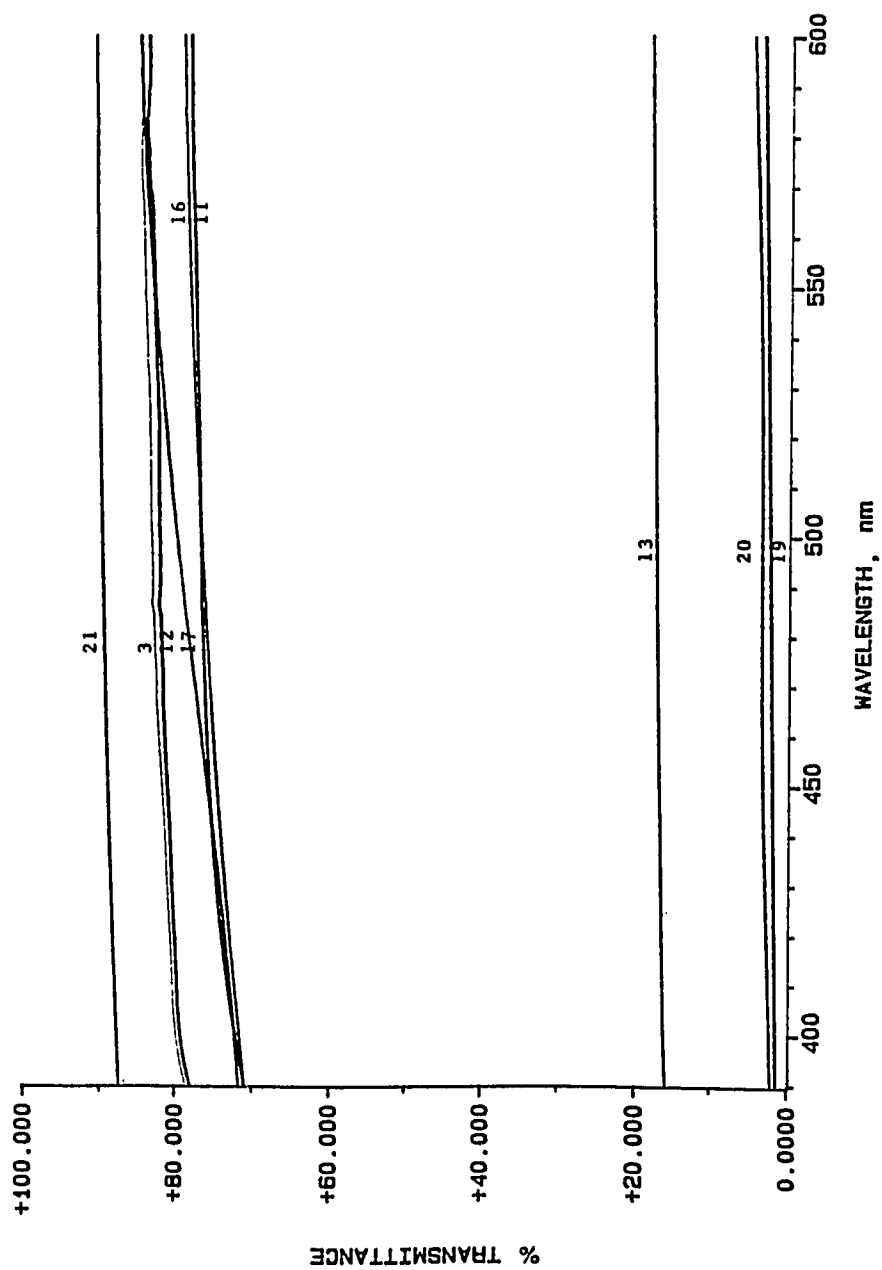


Figure 5.3: UV-visible transmittance of reactively evaporated Al-oxide thin films.

Table 5.1: Process Parameters and the Corresponding Optical Transmittance Values for the Model Electrodes

Sample	t (\AA)	P_{O_2} (T)	T_s ($^{\circ}\text{C}$)	r($\text{\AA}/\text{s}$)	% τ at 50 \AA	% τ_n	n
*3	480	2×10^{-5}	430	1.00	86.14	95.64	1.53
11A	400	2×10^{-6}	330	0.55	77.07	85.75	2.21
*12A	400	4×10^{-5}	310	0.20	82.86	92.36	1.76
*13A	400	2×10^{-7}	55	0.20	16.65	26.15	-
16A	400	7×10^{-4}	300	0.60	79.55	88.23	2.04
17A	350	1×10^{-6}	325	1.00	78.85	87.53	2.09
19A	1015	1×10^{-4}	300	0.10	2.34	11.02	-
20A	265	9×10^{-5}	350	0.50	4.15	12.83	-
21A	120	1×10^{-4}	230	0.30	90.12	98.80	1.25
*0(type1)	2.2mm	-	-	-	91.32	100.00	1.00
0(type2)	1.6mm	-	-	-	90.50	100.00	1.00

Inherently transparent materials often appear translucent (i.e. milky white in color) because they transmit light diffusely due to multiple internal reflections. It is known that conventionally sintered alumina is opaque, whereas porefree polycrystalline alumina is translucent, and even exhibits transparency if not too thick. Refractive index, n, of alumina is given between 1.63-1.80 for the region 0.27 - 1.5 μm [9]. For the six transparent films given above, if the absorption coefficient α is taken as zero and it is assumed that the light loss is due to the reflection at the

air-coating interface, the refractive indices can be calculated using Equation 3.3, as $n = 1.25-2.21$ for the visible light region.

The fraction of the incident radiation that is absorbed by the model electrodes is a function of the thickness of the material and the concentration of the absorbing species in it, according to Beer's law. It is observed that the transmittance values of the films are all functions of the four (4) main independent deposition parameters. Samples 12A and 13A have the same thicknesses and deposition rates. Therefore, much lower % τ observed for the sample 13A is likely to be due to either lower T_s or lower P_{O_2} level (in the order of 10^{-2}) or both. Films 11A and 16A which have similar thicknesses, rates and substrate temperatures differ in their P_{O_2} by $\sim 10^{-3}$ Torr and only show approximately 2.5 % difference in their transmittance in the t , r and P_{O_2} range specified.

These results were summarized in Figure 5.4 where the percent transmittance of the films (% τ_n) for 500 nm photons was plotted against one of the deposition parameters as the other three parameters were taken in a small range of values. Figure 5.4a, therefore, shows very little dependence of τ on the deposition rate, r , ranging between 0.2-1.0 Å/sec and the transmittance of the films tends to remain constant within the deposition rate range. As shown in Figure 5.4d, the optical transmittance increases logarithmically with substrate temperature (for $T_s = 50-350$ °C). Figure 5.4.c shows the tendency of the transmittance to decrease with the film thickness. Therefore, the dependence of τ on P_{O_2} may be plotted as shown in Figure 5.4b.

It should be noted that Figure 5.4 shows the effect of each deposition on transmittance for only three model samples. A deeper study in this area requires processing more samples to be able to conclude on the optimum conditions for transparent

films. However, the samples specified in Table 4.2 were processed such that they are expected to have enough transmissivity to work under PEC conditions.

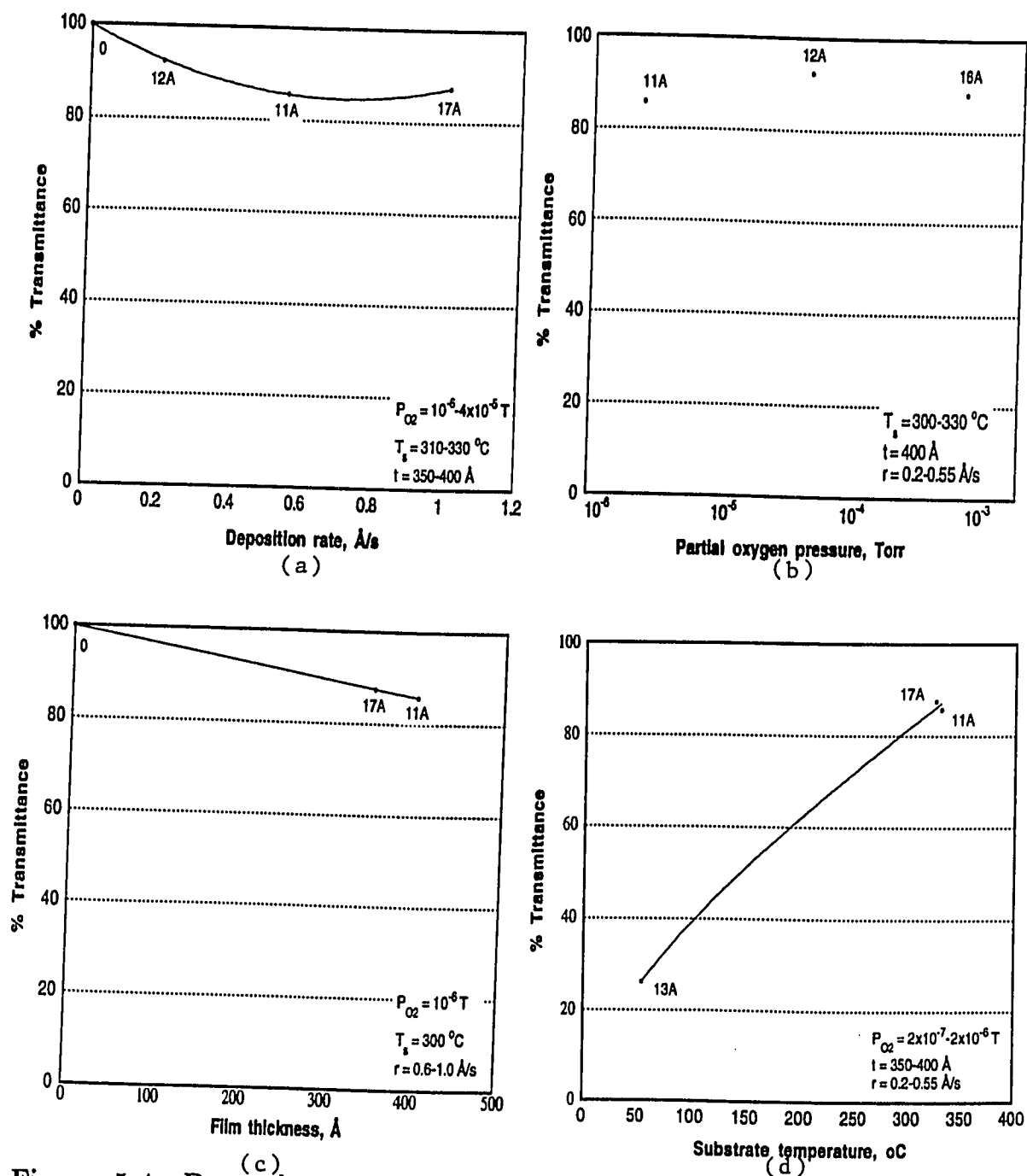


Figure 5.4: Dependence of the optical transmittance at 500 nm on the four main independent deposition parameters.

5.2 Surface Morphology of the Semiconductor Electrodes

Surface topography of the films was revealed by scanning electron microscopy. Several samples, namely 8, 10, 11B, 12B, 16B, 20B, 21B, were observed under SEM and the surface morphology is reported in this section.

Figure 5.5 compares two different surface points on sample 10. The film is only 30 Å thick. Figure 5.5a shows a collection of small and oriented ($\sim 10\ \mu\text{m}$) islands, whereas Figure 5.5b shows a relatively high density of oriented and smaller particles of $\sim 1\ \mu\text{m}$ diameter, separated by 1-10 μm . Such different morphologies suggest a temperature gradient along the sample.

According to Neugebauer [52], islands (planar growth) form on the substrate in the very first stages of growth, i.e the first few monolayers of the film material. Hart et al. [60] showed that crystalline aluminum oxide forms in the temperature range 350-540 °C with a low rate island formation in the pressure range of 10^{-5} - 5×10^{-8} Torr. Increasing the substrate temperature at a constant deposition rate will increase the size of the critical nucleus, therefore, the film will have an island character and will not be electrically continuous up to a much greater average film thickness. Micrograph "a" (islands) was taken on the middle of the sample and micrograph "b" (continuous film) was obtained from the edge of the sample. Then it may be concluded that the substrate temperatures are lower at the edges than at the center. Different morphologies on the same surface, however, were not observed on thicker samples. This observation means that the temperature gradient existing on the sample is very small and it loses its importance as the film grows thicker. Figure 5.6 illustrates 10 and 7.5 times higher magnifications from the same two points on sample 10, shown in Figure 5.5.

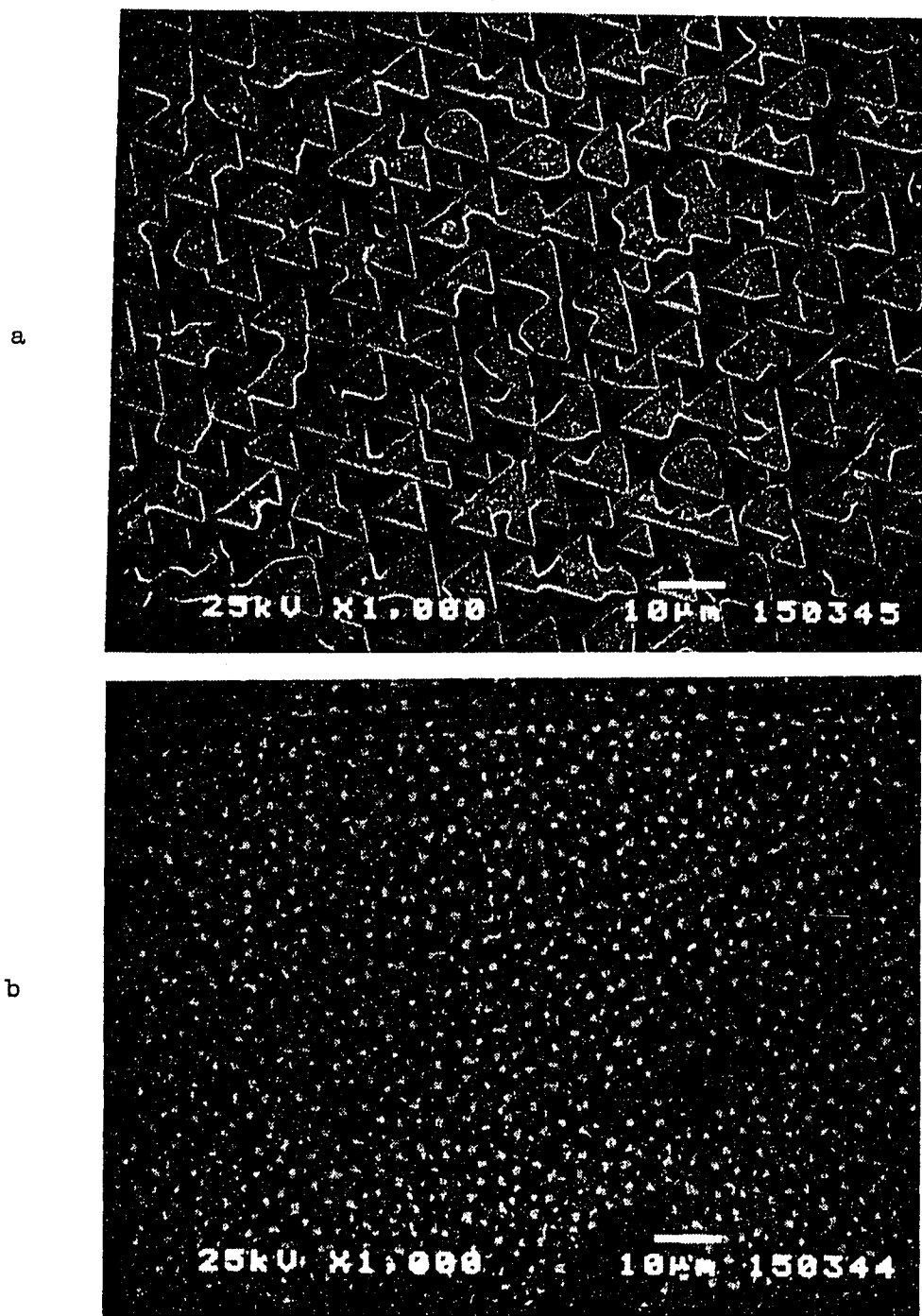
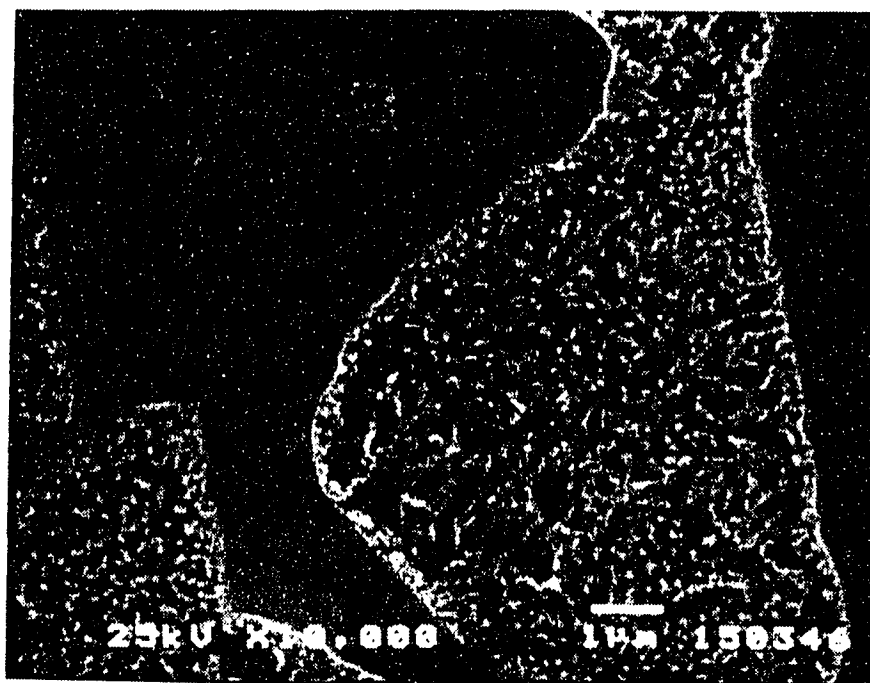


Figure 5.5: The first stages of the Al-oxide growth on an n-Si(111) surface, a) from the center, b) from the edge.

a



b

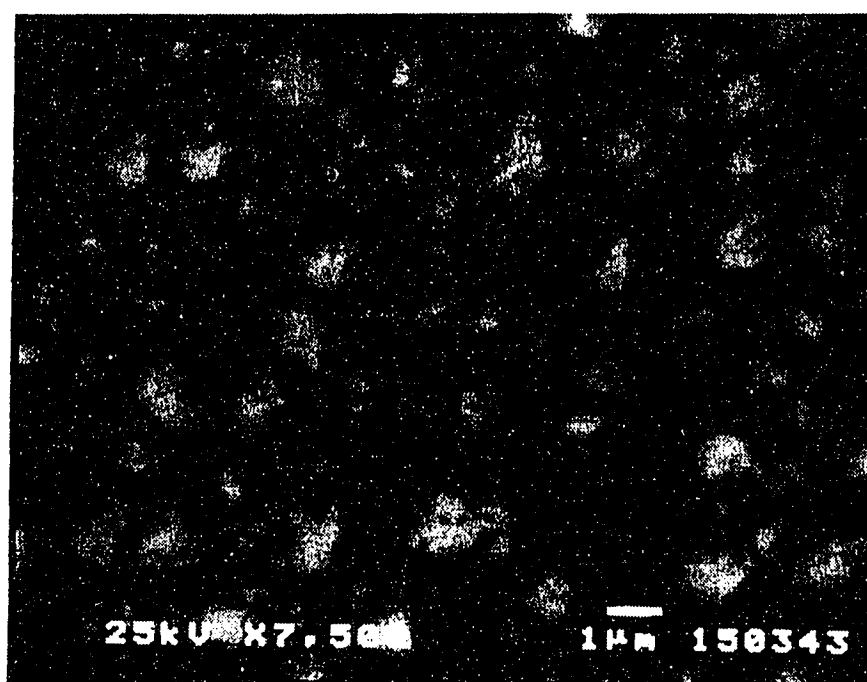


Figure 5.6: Two different morphologies magnified from the previous figure.

The tendency to form an island structure is increased by a high substrate temperature, with a low boiling point film material, a low deposition rate, a high surface energy of the film material and a low surface energy of the substrate [52]. Therefore, sapphire with a surface energy of 1.2 J/m^2 [20] is not likely to wet Si which has a surface energy of 0.87 J/m^2 [66].

The electrical resistivity of island films is dominated by the gaps between the islands across which the electrical charge must jump to generate current flow rather than the bulk resistance of each island itself. The resistivity of typical island films is perhaps 10^6 times that of the bulk. For the purposes of this work, as it was explained in Chapter 3, continuous films are preferred to the films with island structures. Figure 5.7 shows 100 \AA thick sample 21B deposited at 230°C at a low rate and a high oxygen pressure. The surface film has atomic clusters of different shapes and sizes (0.1-5.0

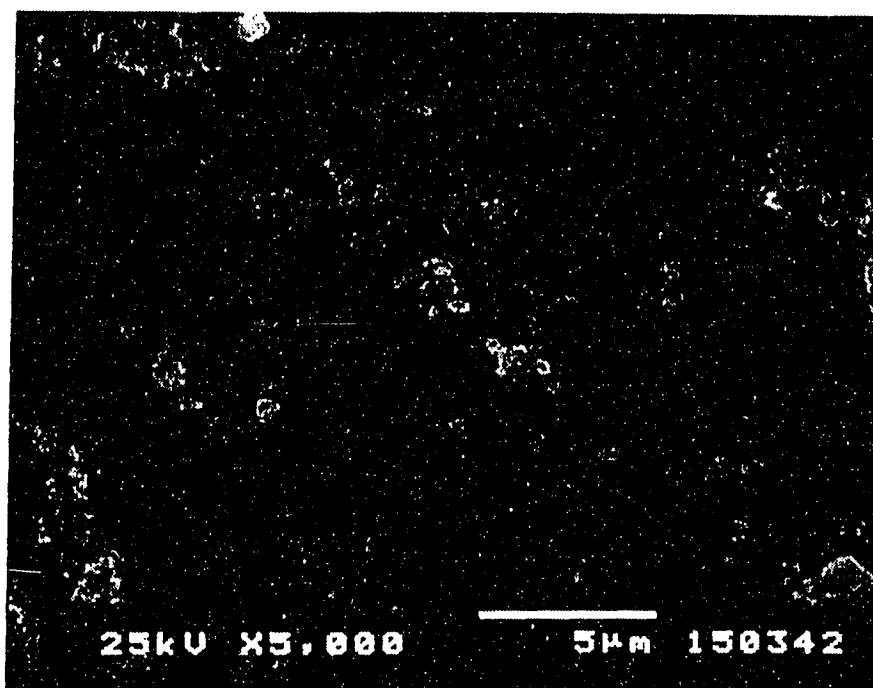


Figure 5.7: SEM micrograph of a 100 \AA thick oxide film.

$T_s = 230^\circ\text{C}$, $r = 0.3 \text{ \AA/s}$, $P_{O_2} = 10^{-4} \text{ Torr}$.

μm) growing on an underlying continuous film which is likely amorphous Al-oxide rather than Si.

Figure 5.8 compares samples 11B (b) and 12B (a) which have the same thicknesses of 400 \AA . However, sample 12B deposited at a higher substrate temperature, lower rate and higher oxygen pressure shows no obvious features and it is continuous all along the surface. Samples 16B and 20B do not have any apparent features, either. Sample 11B shows clusters which seem to be more spherical, much higher in density and bigger in size than the ones observed on sample 21B.

In Figure 5.9, the surface of sample 8 is seen. 510 \AA thick coating on p-Si(100) shows an incompleted coalescence situation. Very small clusters of $< 0.5 \mu\text{m}$ diameter tend to shrink into the growing film as the deposition continues. The coalescence of the clusters represent a lower energy state for the system and the small clusters combine to form bigger clusters and then probably a continuous film. No cracks were observed on these samples even at magnification of 10,000.

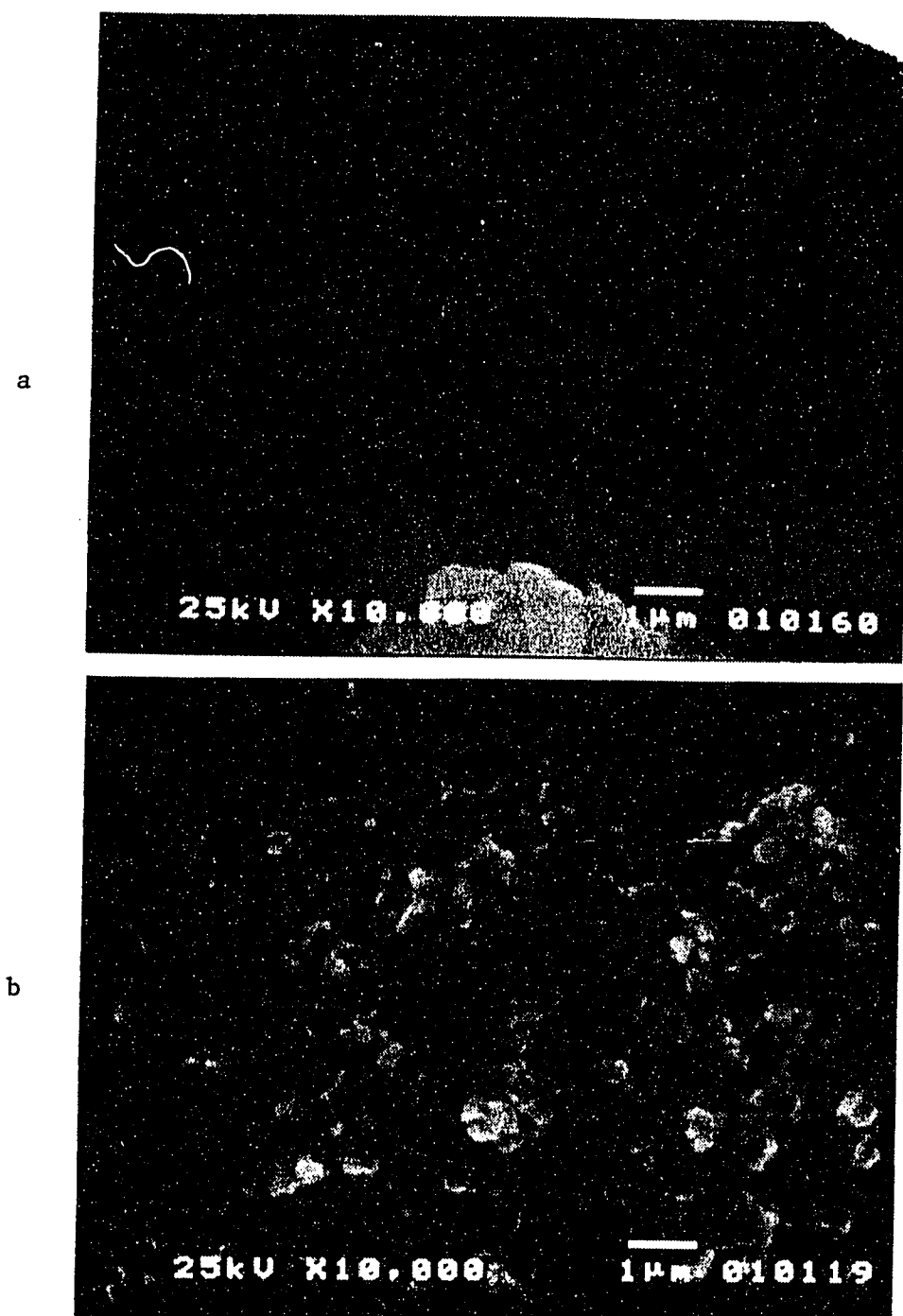


Figure 5.8: Structural dependence of the films on oxygen concentration.

a) 4×10^{-5} Torr, b) 2×10^{-6} Torr.

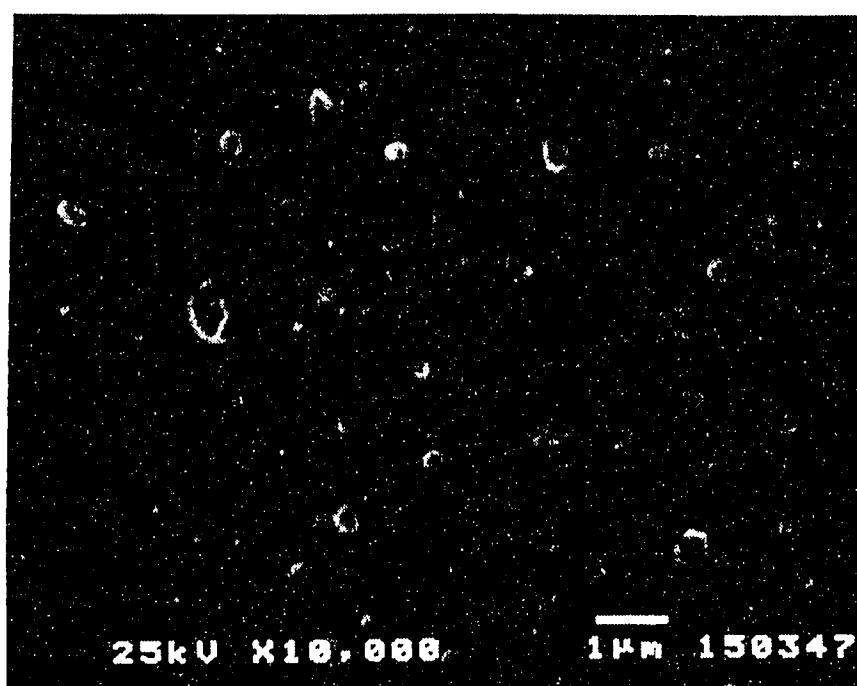


Figure 5.9: SEM micrograph of a 510 Å thick oxide film.
 $T_s = 350^\circ\text{C}$, $r = 2.00 \text{ Å/s}$, $P_{O_2} = 10^{-6} \text{ Torr}$.

5.3 Surface Chemistry of the Electrodes

AES and XPS results are reported in this section to obtain the identity of the electrode surfaces and the bulk coatings. Auger spectra from the samples B and E are shown in Figure 5.10 and Figure 5.11, respectively. The peaks of Al(LMM), O(KLL) and Al(KLL) are seen in both samples and their shapes are comparable with the aluminum oxide spectra shown in Figure 3.6. The spectrometer shifted the kinetic energies of the detected electrons by different amounts for different peaks, therefore the peak energies do not correspond to the exact handbook values. Figure 5.10 was obtained in-situ right after the film B was deposited. Therefore there is no carbon peak observed on the spectrum. Sample E shows some carbon on the surface associated with handling where the C peak disappears after ion sputtering of the surface.

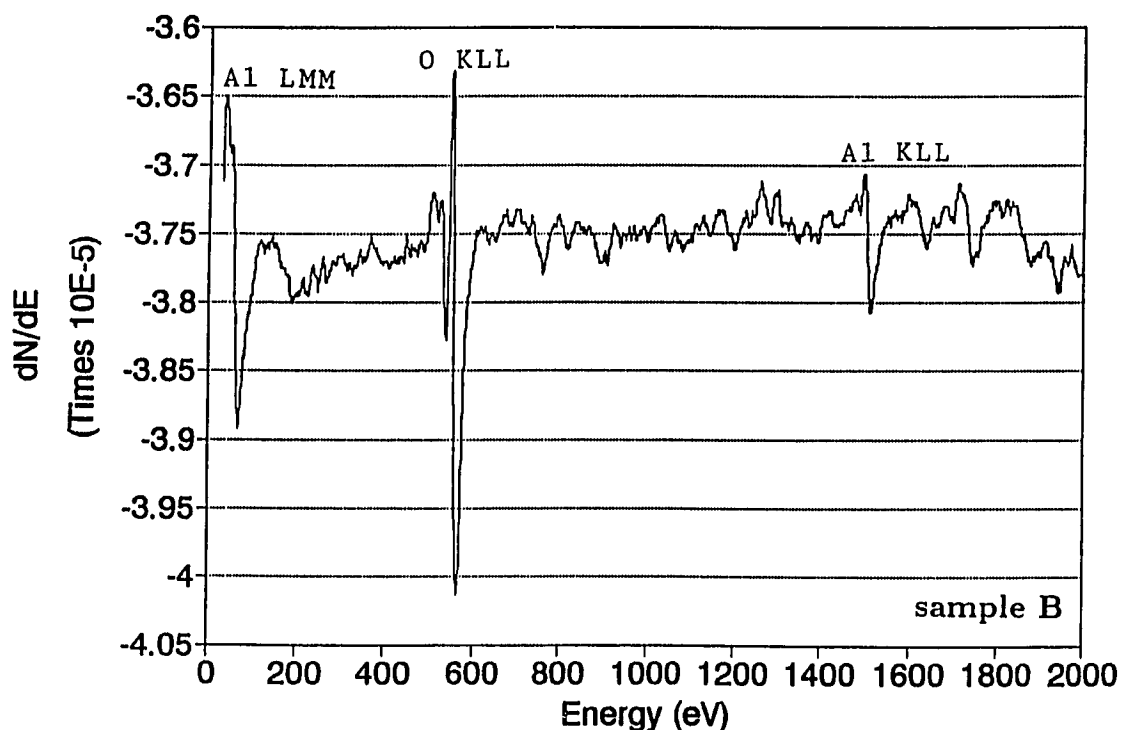


Figure 5.10: Auger electron spectrum taken in-situ.

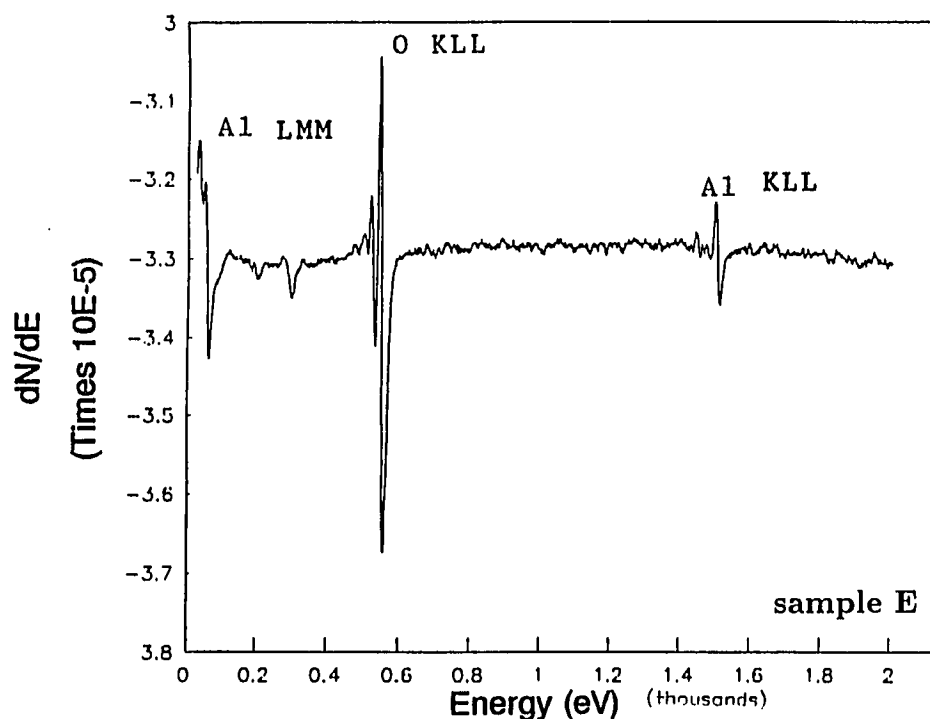


Figure 5.11: Auger electron spectrum taken ex-situ.

The relative surface concentrations for the samples can be calculated assuming all experimental parameters, such as the incidence angle of the primary electrons, primary beam energy, etc., were constant. By measuring the peak to peak heights from the spectrum and taking the Auger transition sensitivity factors as 0.11 for Al(KLL), 0.45 for O(KLL) and 0.22 for Si(KLL), the x/y ratio in the Al_xO_y samples can be calculated as 1.1 for sample B (Al_2O_2) and 0.85 for sample E (Al_8O_9 , assuming the peak heights are not affected by the small amount of carbon on the surface). Sample D was also analyzed by AES. Its surface does not show any carbon and the calculations result in a composition that is the same as sample E. These numbers are found to be reasonable for the surface oxide stoichiometries which can correspond to seven different compositions as reported in Table 5.2.

Table 5.2: Stoichiometries Reported For Aluminum-Oxide.

Al_xO_y	x/y
Al_2O	2.00
Al_4O_3	1.33
AlO	1.00
Al_2O_2	1.00
Al_8O_9	0.89
Al_3O_4	0.75
Al_2O_3	0.67

AES was also used to determine the composition of the films as a function of their depth. Sample 9 with 405 Å oxide film on its surface was Ar-ion beam sputtered for ~ 1 min and the spectrum was taken after each sputtering period. The results are reported in Figure 5.12 as peak to peak height (PPH) versus sputtering time. The sputtering rate can be calculated as ~ 0.1 Å/sec from the figure.

Figure 5.13 gives the elemental mole fractions in a direction normal to the surface as a function of sputtering time (or depth) for sample 9. All along the depth, the x/y ratio stays between 0.8-1.0 as seen from the Figure 5.14. This gives a composition between Al_8O_9 (or $Al_2O_{2.25}$) and Al_2O_2 to the film.

Auger depth profiles were also obtained for samples 6 and 8 and also reported in the Appendix. The composition of the films change between Al_8O_9 (or $Al_2O_{2.25}$) and Al_4O_3 (or $Al_2O_{1.5}$) for sample 6 and that for sample 8 is Al_3O_4 (or $Al_2O_{2.67}$). Therefore, it can be concluded that quantitative AES shows a uniform distribution of aluminum and oxygen throughout the film thickness.

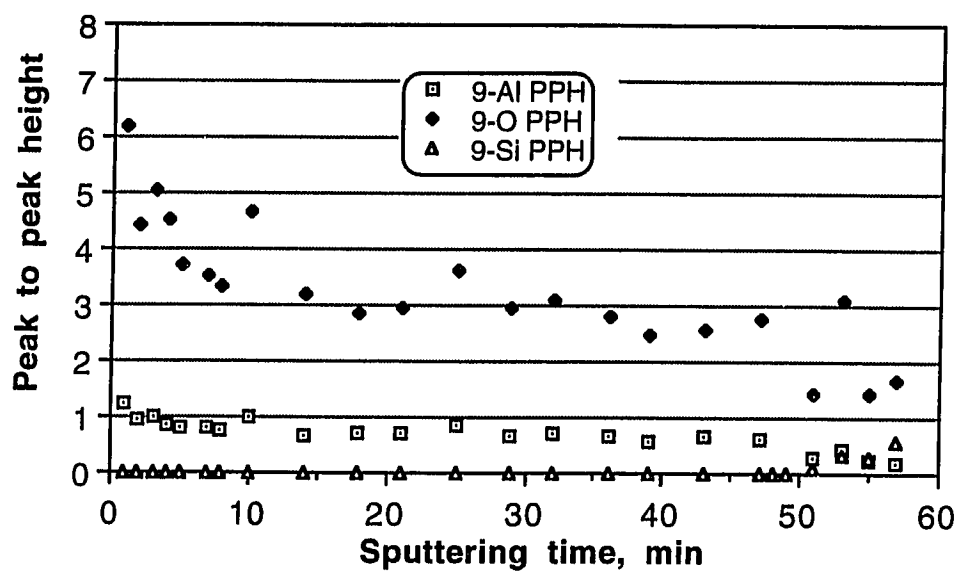


Figure 5.12: Auger electron depth profile (405 Å oxide on n-Si(111)).

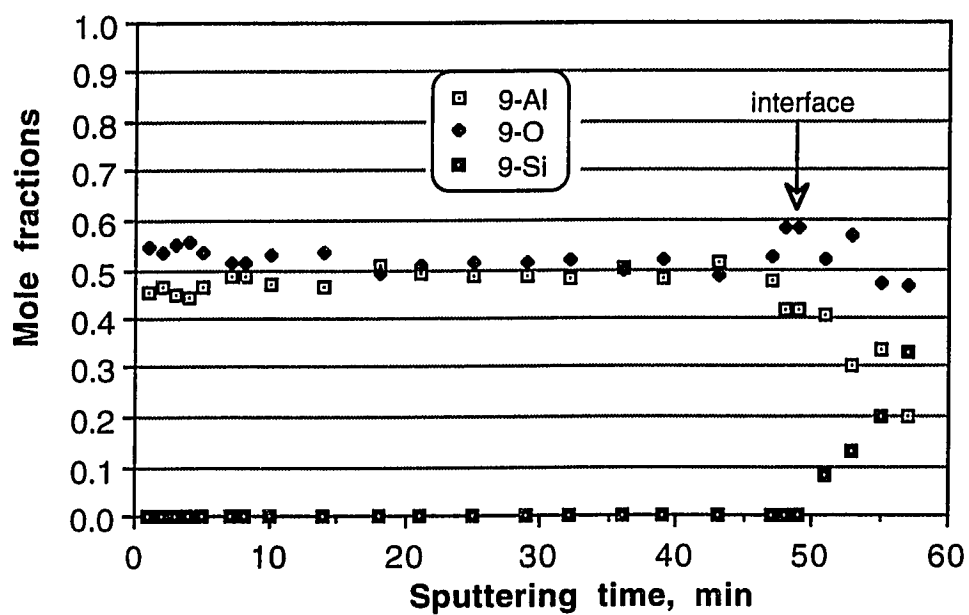


Figure 5.13: Relative film composition as a function of depth.

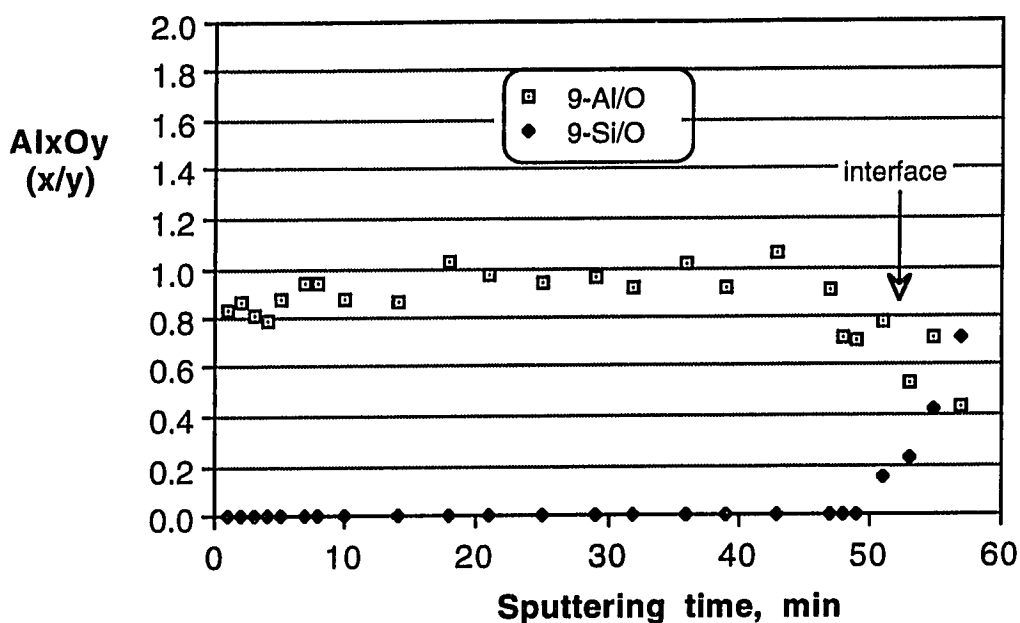


Figure 5.14: Stoichiometry of the film as a function of depth.

Wide scan XPS spectra from samples 8, 10, 11B, 12B, 13B, 14, 17B, 20B and 21B contained peaks from aluminum, oxygen and carbon. Samples which are not thicker than 50 Å also showed Si peaks from the substrate. The high carbon contents observed are due to sample handling and the time between the deposition and the measurements. The spectrum shown in Figure 5.15 for sample 21B (100 Å) is typical of the ones observed with the other as-deposited samples and it is comparable with the one shown in Figure 3.10. Figure 5.16 (sample 12B) can also be compared with the oxygen Auger peak shown as inset on Figure 3.10. It should be noted that the binding energy values on the XPS spectra, presented in the Figure 5.15 through Figure 5.18, correspond to the as-plotted, uncorrected values (for charging effects) obtained from the instrument. If C(1s) peak at 285.85 eV is referenced to 284.6 eV, O(KL_{2,3}L_{2,3}) peak energy is calculated as 745.74 eV, which is at 0.44 eV higher than the peak energy shown in the inset of Figure 3.10. Other peaks (O(KL₁L_{2,3}) and O(KL₁L₁)) are shifted to higher energies by 0.55 and 2.73 eV, respectively. The large surface

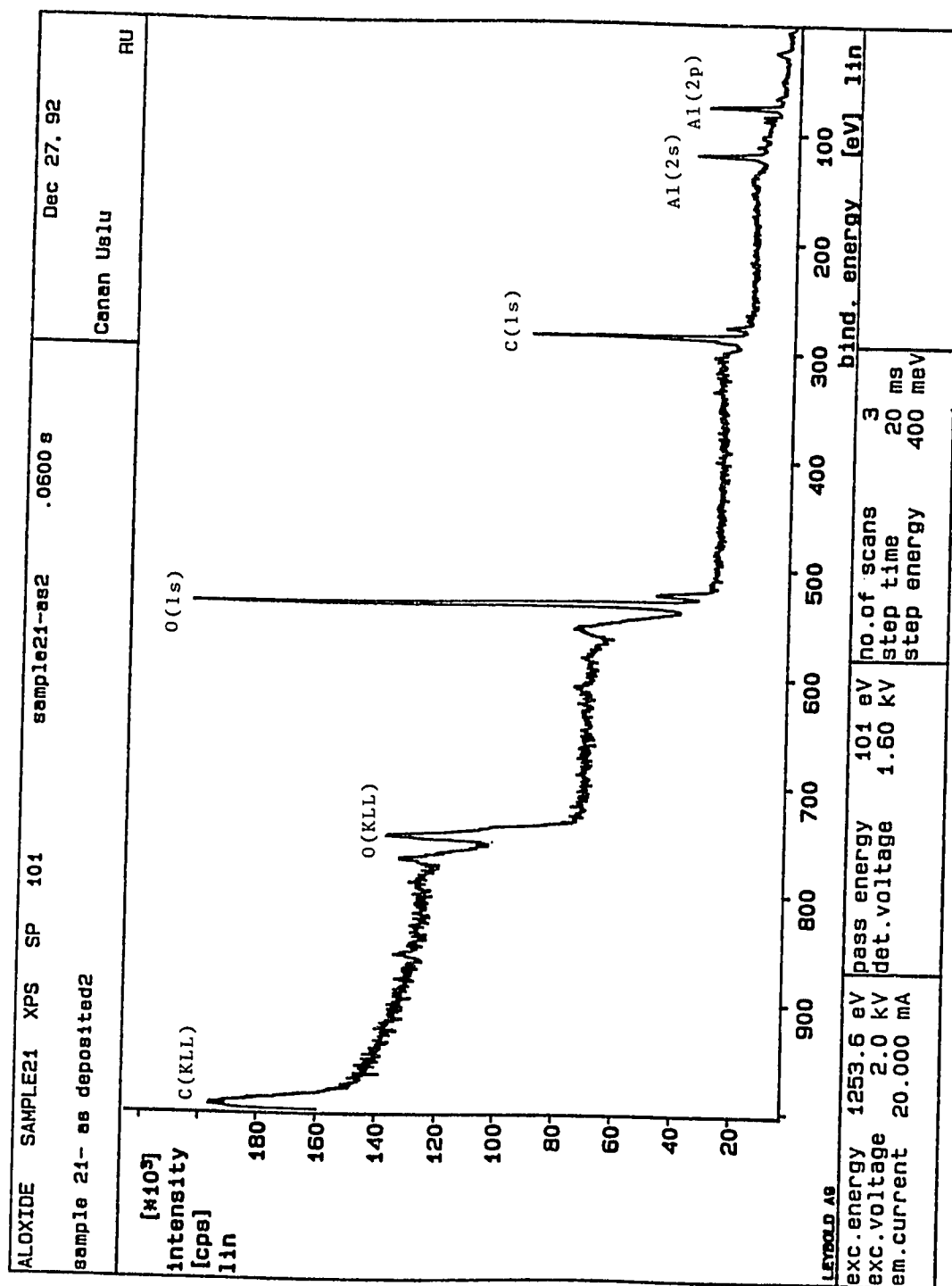


Figure 5.15: A typical wide-scan XPS spectrum from the electrode surfaces.

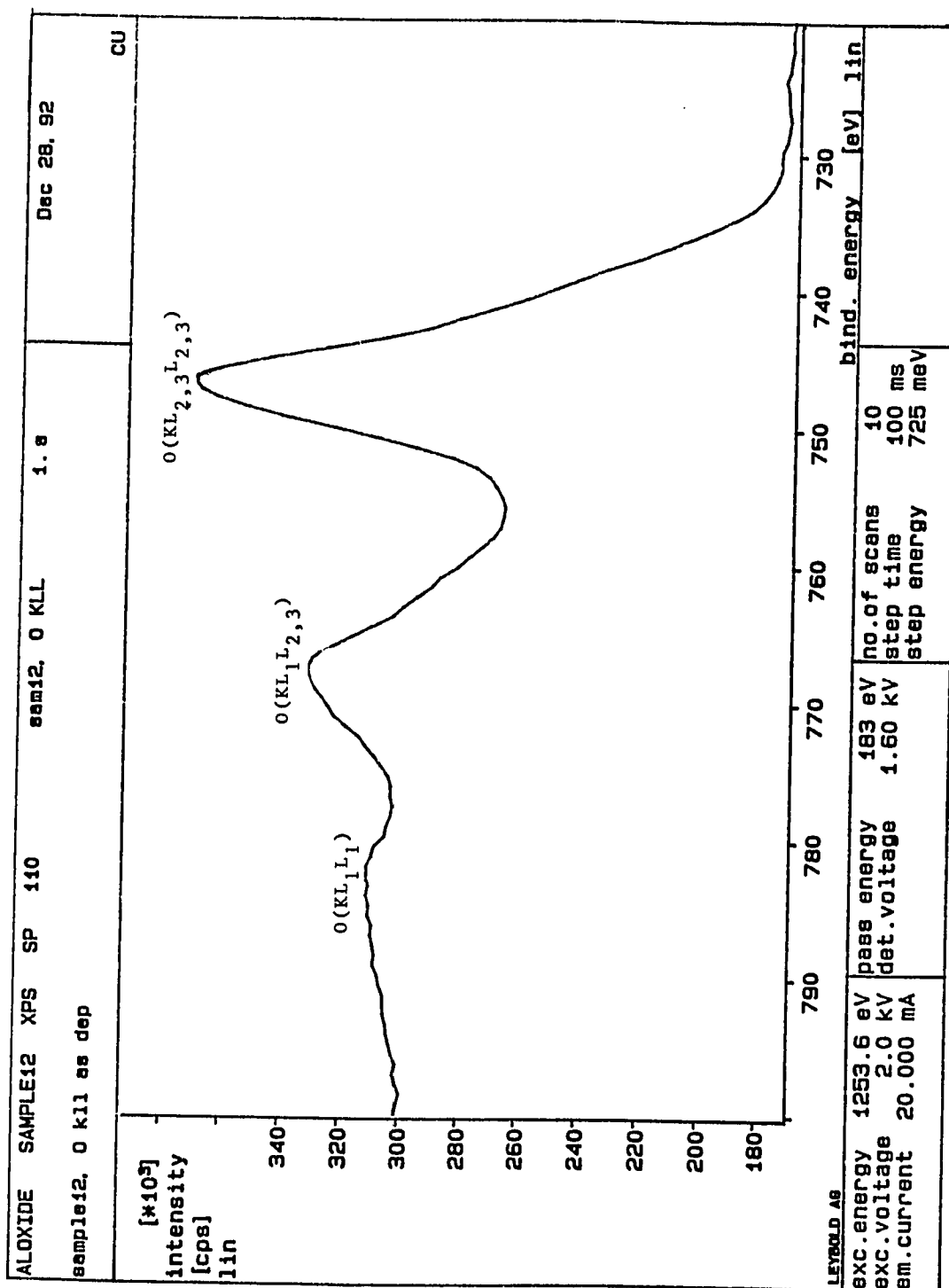


Figure 5.16: Short-scan XPS spectrum of O(KLL) Auger emission from the oxide film surfaces.

C(1s) peak which needs to be sputtered off to obtain the film stoichiometries and the oxidation states assuming the charging correction and the instrument calibrations are valid and the ion beam induced reduction phenomena of Al is negligible.

Characterization of the films by XPS can be continued by paying particular attention to the position of the Al(2p) line in the low scan spectra. C(1s) peak from the surface carbon was set to a binding energy of 284.6 eV to correct the binding energy values of Al(2p), Al(2s), O(KLL), C(KLL) and Si(2p) for electrical charging [69]. The results are summarized in Table 5.3 where the binding energies (in eV) measured for the peaks from each sample are listed. Included in this list are the values measured for the O(1s), Al(2p), Al(2s) and Si(2p) peaks and the x-ray induced O(KLL) and C(KLL) Auger transitions after the correction for charging. Each row of numbers represent different points on the surface and the highlighted numbers correspond to the binding energies from the narrow-scan XPS spectra. The mean binding energy of the Al(2s) peak (119.55 eV) in the spectra from the surfaces of samples 8, 10, 22B (see Table 5.3) is typical of the oxidized state of the metal [65]. As can be seen from the table, the binding energies for the O(1s) peak are around 531.6 ± 0.35 eV and that of Al(2p) is 74.41 ± 0.57 eV after the correction for surface charging (0.54 - 2.64 eV) of the as-grown films.

Figure 5.17 shows the characteristics of an Al(2p) peak for the oxide rather than elemental aluminum when compared with Figure 3.14. Figure 5.18 reports the Al(2p) peak from sample 12B studied under 120 eV synchrotron radiation. The lower photon energy used makes the results more surface sensitive. Here an as-deposited sample is compared with the 14 μm thick anodized aluminum sample which consisted of Al, O, and S in the ratio of 1.52 : 1.00 : 0.07, respectively as detected with the microprobe analysis. The stoichiometry of anodic aluminas corresponds to nearly perfect Al_2O_3 ,

Table 5.3: Summary of XPS binding energies (in eV) from all samples analyzed.

sample	C 1s	O 1s	Al 2p	Al 2s	OKLL	C KLL	Si2p
8	285.37	531.55	73.92	118.67	745.66		
	285.58	531.55	73.86	118.76		993.94	
	285.32	531.88	74.98	119.84	746.90	992.81	
	285.52	531.44	74.08	118.90	745.83		
	284.95	532.01	74.99	119.79	746.79	992.81	
10	285.37	531.63	74.26	119.13	745.21	993.56	100.61
	285.71	531.59	74.15	119.12	745.32	993.42	100.12
	285.63	531.63	74.41	119.42	745.15	992.37	100.18
	286.06	531.59	74.23	119.48	746.11	993.54	
	285.80	531.57	74.23	—	746.11	993.54	
11	286.95	532.32	74.72	119.54	746.61	993.57	
	287.01		73.71				
	286.94	531.32	73.79	118.62	746.61	993.57	
	287.16	531.32	73.84				
	287.55		74.06				
12	285.20	531.57	74.05	118.89	745.64	994.22	
	285.40	531.69	74.26	119.05	745.71	994.92	
	285.08	531.70	74.31	119.02	745.75	995.48	
	285.69	531.27	73.71	118.57	745.41	993.18	
	285.56	531.31	73.83	118.69	745.61	993.37	
	285.59	531.28	73.78	118.53	745.55	993.73	
	285.66	531.25	73.79	118.57	745.63	993.85	
	285.85	531.25	73.84		745.74		
13	285.89	531.49	74.20	118.95	745.88	993.21	
	285.37	531.85	74.69	119.55	746.09	994.78	
	284.83	532.54	75.73	120.59	747.57	995.63	
	284.56	532.69	75.73	120.59	747.57	995.63	

Table 5.3: XPS binding energies (in eV) from all samples analyzed (cont.).

sample	C 1s	O 1s	Al 2p	Al 2s	OKLL	C KLL	Si2p
14	285.58	531.43	74.03	118.88	745.62	993.91	
	285.73	531.44	74.03	118.85	745.50	993.73	
	285.81	531.39	73.95	118.81	745.64	993.72	
	285.85	531.35	74.00	118.80	745.64	993.49	
	285.95	531.39	74.14				
	285.56	531.48	74.56				
17	287.26	531.57	73.86	118.76	745.94	992.42	
	286.95	531.63	74.04	118.91	745.74		
	286.98	531.63	74.01	118.84			
	287.11	531.52	74.07		745.81		
20	286.55	531.47	74.04	118.82		993.46	98.42
	287.05	531.29			745.59	992.89	
	286.91	531.31	74.15		745.96		98.52
	286.84	531.36	74.43		746.21		99.70
	286.78	531.57	74.59	119.36	746.35		98.84
21	285.44	531.56	73.91	118.73	745.72	993.34	
	285.67	531.54	73.88	118.67		993.61	
	285.78	531.51	73.85	118.67		994.25	
	286.01	531.61	74.05		746.11		

although there are indications of both oxygen and aluminum deficiency [18]. The Al(2p) peak from as-deposited sample 12B is at 76.3 eV (1.11 eV higher than the value obtained at Rice) and it shifts by -0.8 eV with surface sputtering. The peak binding energy is 0.5 eV higher than the Al(2p) peak energy for the anodized aluminum sample and the difference decreases to 0.1 eV after sputtering. However, there is no

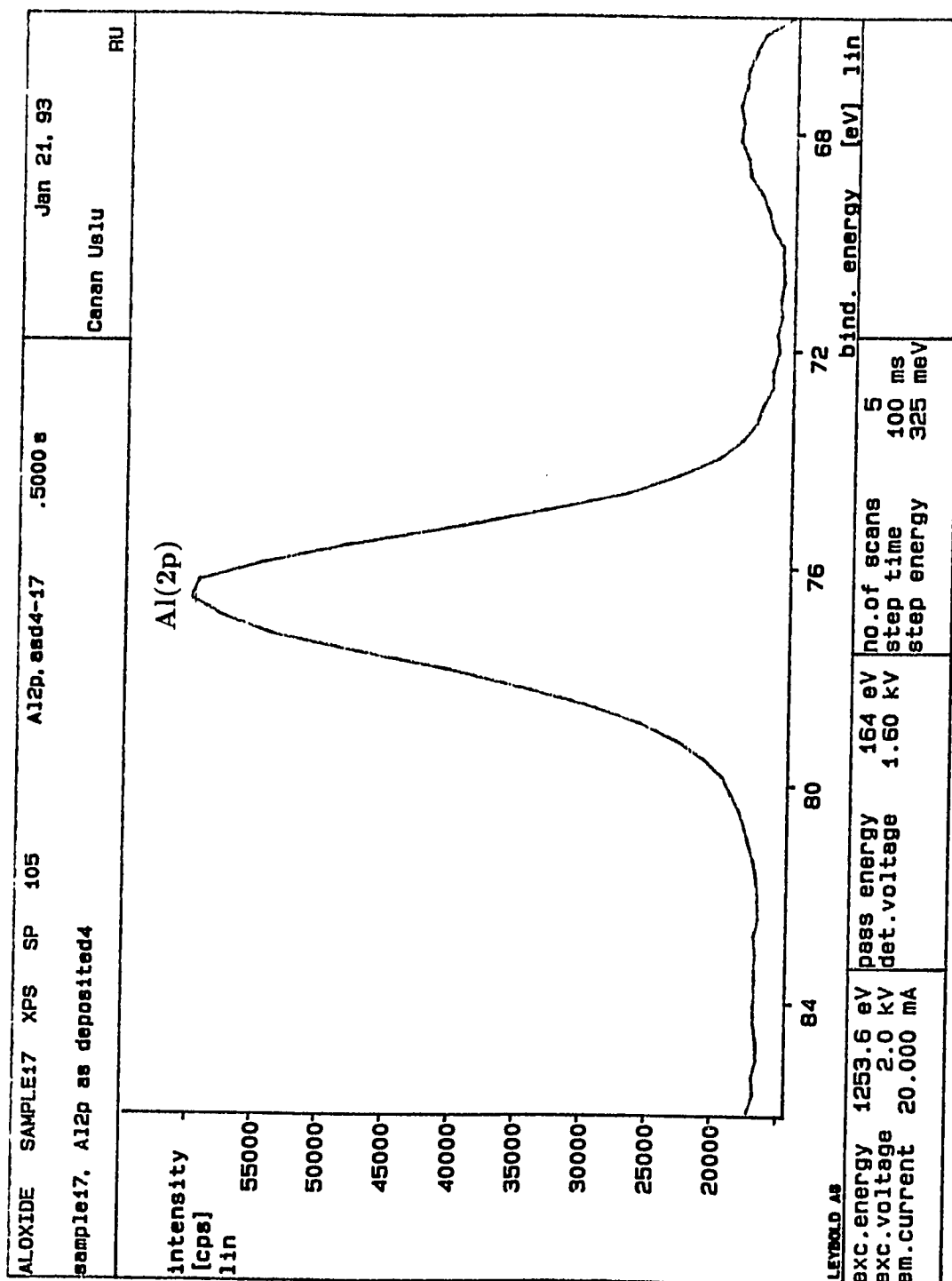


Figure 5.17: Typical shape of Al(2p) peak from the samples analyzed.

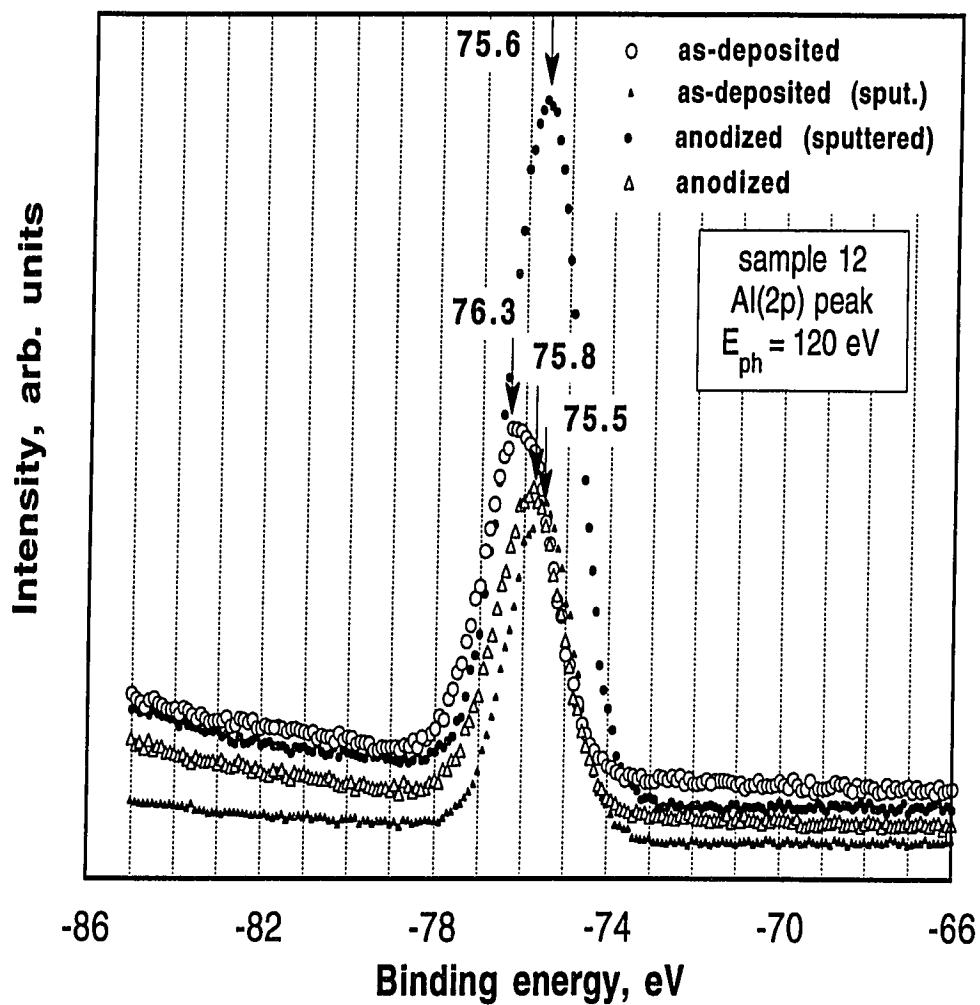


Figure 5.18: Narrow scan XPS peak studied under 120 eV synchrotron radiation.

charging information available on these samples. If, for example, 0.8 eV is allowed for charging and it is assumed that the oxidation state did not change upon sputtering, the film on 12B can be characterized as amorphous alumina according to Figure 3.14 and Halverson et al. [32].

5.4 PEC Measurements

5.4.1 Photopotentials in the Cell

Before evaluating the stability at the oxide-electrolyte interface, it is first necessary to characterize any photosensitivity present in the system. Upon illumination, the electrodes developed negative photopotentials except samples B, 1, 13B.

The open-circuit potentials for 21 samples analyzed ranged from 326 mV to -640 mV versus the SCE reference electrode (+242 mV vs SHE) under illumination. Oshe and Rozenfeld [56] proposed that the photopotential signs and magnitudes strictly reflect the deviation from stoichiometry, with negative potentials indicating oxygen vacancies and positive potentials indicating cation vacancies. This may be supported by the measurements done on sample 9 which is oxygen deficient as observed with AES (Figure 5.14) and has an open-circuit photopotential of -0.11 V.

The open-circuit potentials (E_{corr}) achieved between the electrolyte and the electrodes under either a Xe lamp light (at 500 nm) or He-Ne laser (632.8 nm) were summarized in Table 5.4. The photoresponses, $E_{photo} = ||E_{dark} - E_{light}||$, from the electrodes during E_{corr} -t behavior measurements are also given in the table. Under the Xe lamp illumination, E_{photo} for naked-n-Si is 50 mV. The lower photosensitivity of sample 9 (10 mV) may imply that the film partly absorbs and/or reflects the incoming light so that the photosensitivity of silicon decreases. The photo-responses from the naked-n-type Si cells under illumination are given in Figure 5.19, as well as

Table 5.4: Photopotentials and photosensitivities achieved in the PEC cell containing 1 N H_2SO_4 .

Illumination	Sample	E_{corr} , (or V_{oc})	E_{photo} , photoresponse
Xe lamp at 500 nm	7	-430	0
	5	-180	25
	9	-114	10
	n-Si(111)	-102	50
	B	10	-
He-Ne laser 632.8 nm	22B	-640	8
	12B	-625	10
	21B	-520	80
	14	-450	50
	22A	-420	60
	10	-390	15
	18	-390	30
	4	-310	90
	19B	-270	85
	20B	-265	80
	15	-256	130
	16B	-220	80
	17B	-210	85
	n-Si(111)	-200	70
	11B	-170	3
	2	-132	40
	13B	6	80
	p-Si(100)	50	50
	1	326	0

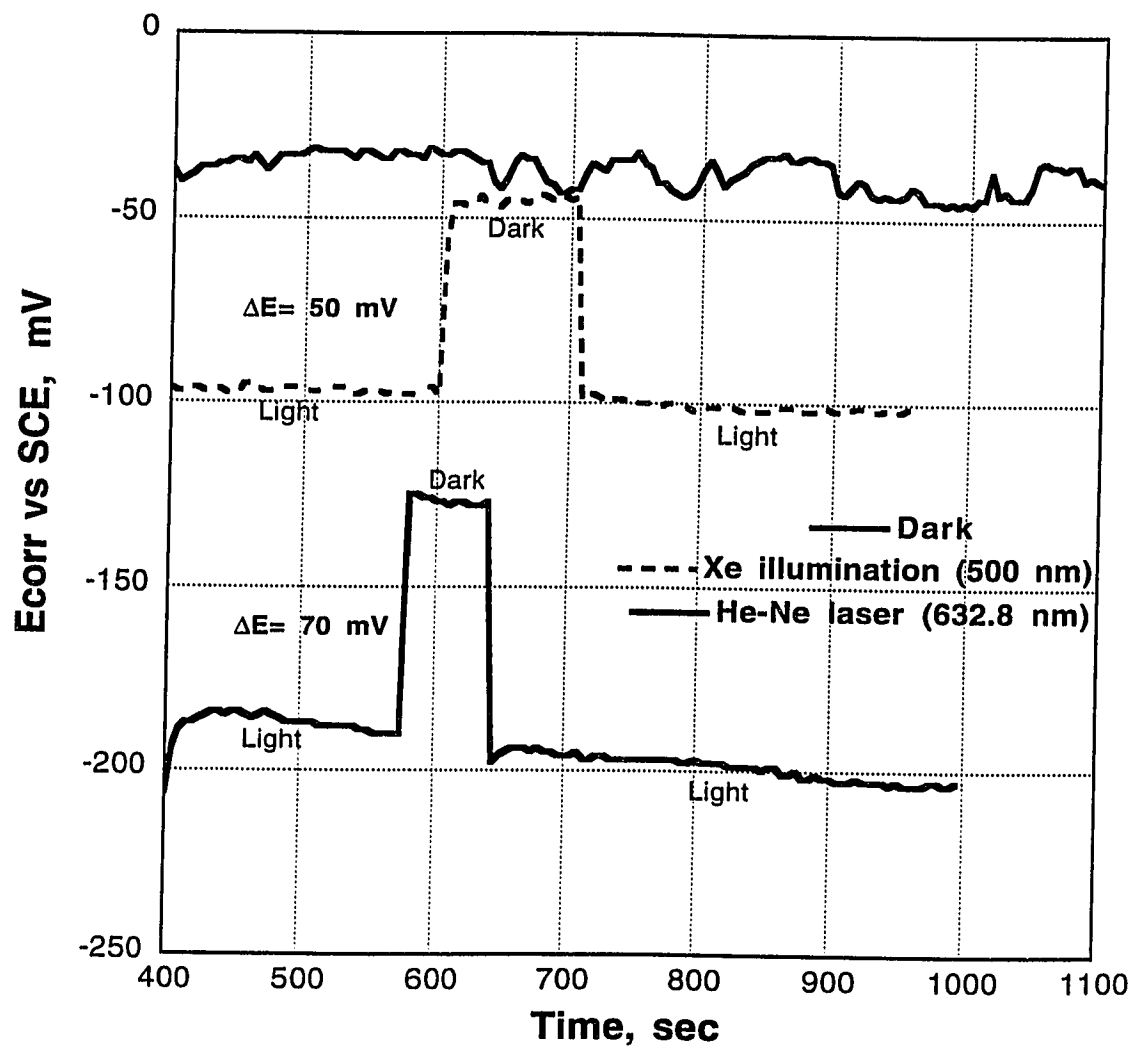


Figure 5.19: Dark- and photo-corrosion potentials in the naked-n-Si(111)/1 N H_2SO_4 electrolyte system.

the corrosion potential achieved under no irradiation. As it is illustrated, for n-type photoelectrodes, the potential in the cell increases in the negative direction with illumination. The photopotential in the cell is also affected by the intensity of the illumination and it increases in the cathodic direction with the increase in intensity. An opposite behavior is observed for the p-type Si cells where the surface-electrolyte interface reach a higher corrosion potential value in the anodic direction when illuminated.

The photosensitivities, E_{photo} , observed for the samples under 632.8 nm He-Ne laser illumination (3 mW/cm^2 , which is greater than the Xe lamp light intensity) are as follows. First, E_{photo} for naked n-Si under laser illumination is higher than that under Xe-lamp radiation. In addition, p-type and n-type bare electrodes under the same radiation differ in their photosensitivities by approximately 20 mV as can be seen from Table 5.3 (n-Si has a higher value). It is also seen that films 1 and 2 decrease the photosensitivity of p-Si, while film 4 increases it (see Figure 5.20). For the films on n-Si substrates, it is observed that samples 13B, 15, 16B, 17B, 19B, 20B, and 21B increase the photosensitivity of n-Si(111) under He-Ne laser illumination, while samples 10, 11B, 12B, 14, 18, 22A and 22B have a negative effect. It is likely that the former set of samples form a partial AR-coating on silicon.

Figure 5.21 plots the photovoltages obtained from the cells containing 12B, 16B, 19B and 20B electrodes. It is seen that the samples 16B, 19B and 20B all converge to similar equilibrium potentials even though their surface film thicknesses are quite different (ranging between 50-400 Å). However, sample 12B deposited at an order of lower oxygen pressure achieves more cathodic open circuit potentials under He-Ne illumination and lacks the property of being an AR-coating on silicon. Figure 5.22 can summarize the dependence of the open circuit potential in the PEC cell under

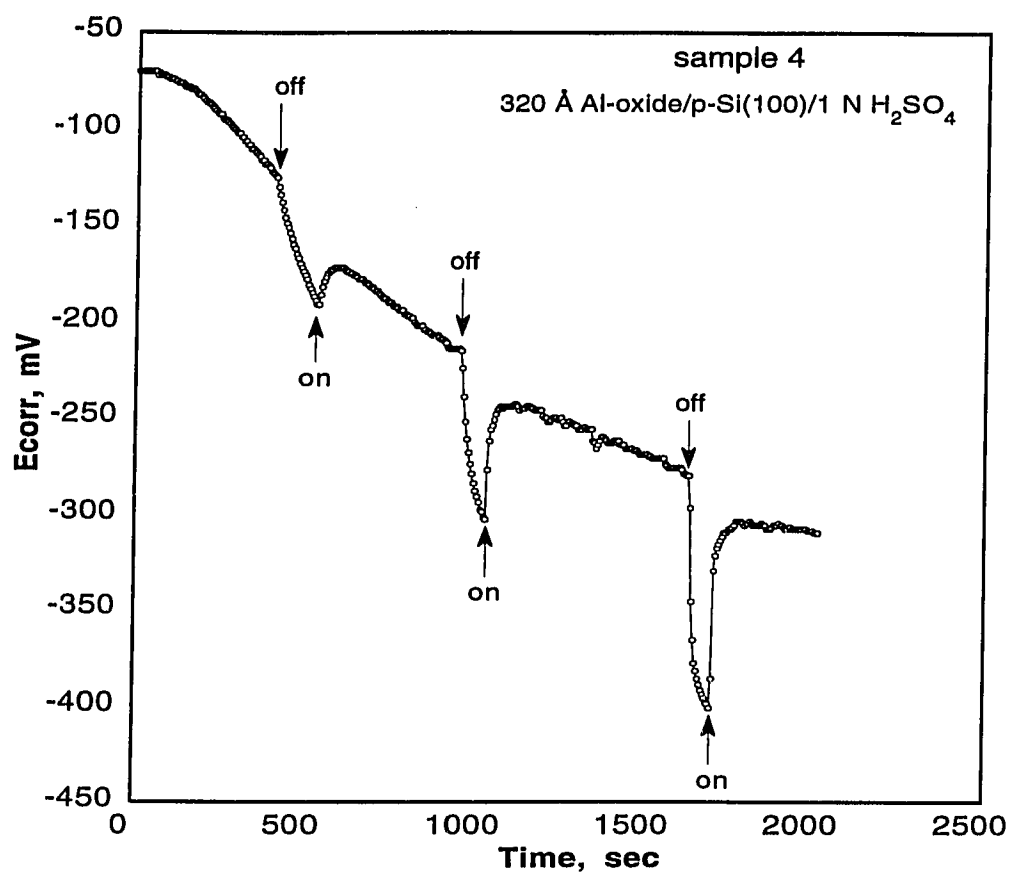


Figure 5.20: A typical photoresponse of an aluminum oxide coated p-type silicon PEC cell.

Electrolyte: 1 N aqueous H_2SO_4 , Illumination: 3 mW/cm² He-Ne laser.

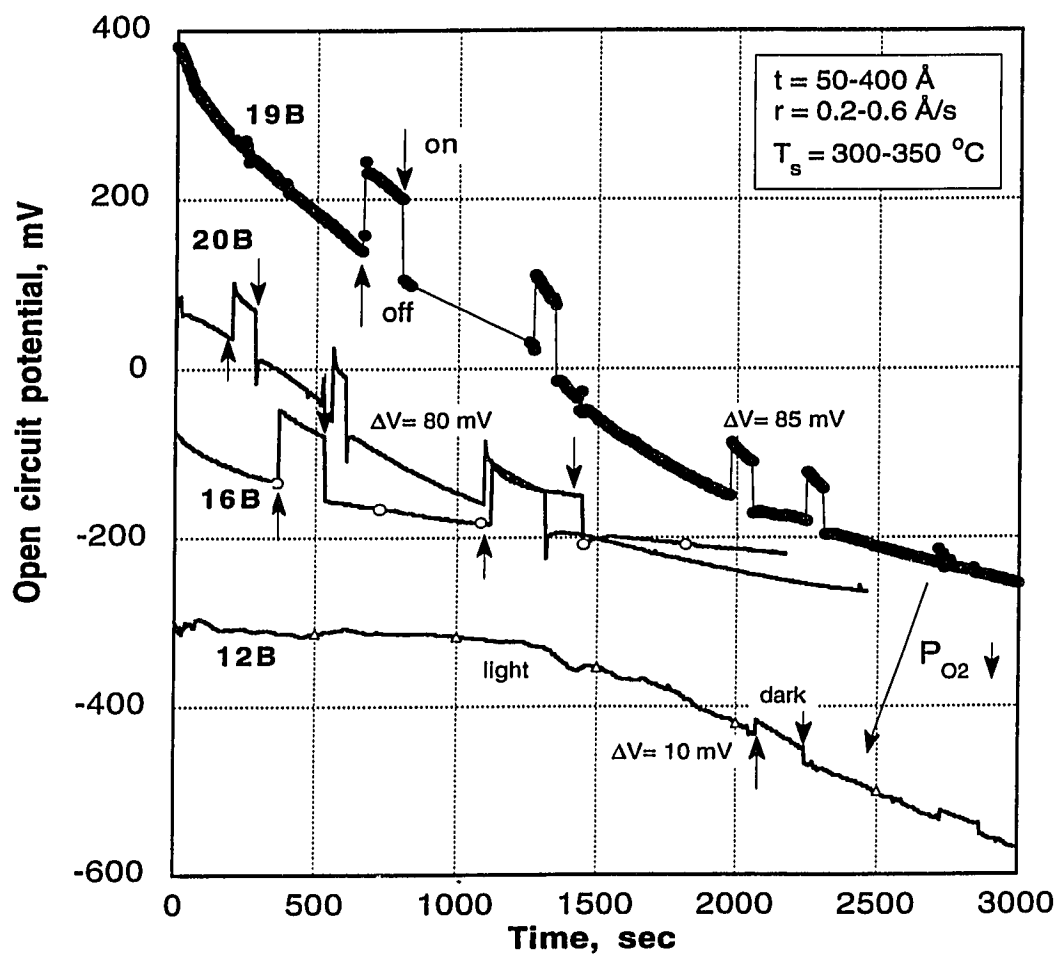


Figure 5.21: Dependence of photovoltage on the partial pressure of oxygen during film deposition.

He-Ne illumination on the sample deposition variables. $-V_{oc}$ seems to have a minimum at a deposition rate of around 0.55 \AA/s and increase with substrate temperature in the range of $305 - 400 \text{ }^\circ\text{C}$ and oxygen pressure in the range of $2 \times 10^{-6} - 10^{-4} \text{ Torr}$ and decrease with film thickness in the range of $50 - 400 \text{ \AA}$ (Figure 5.22a).

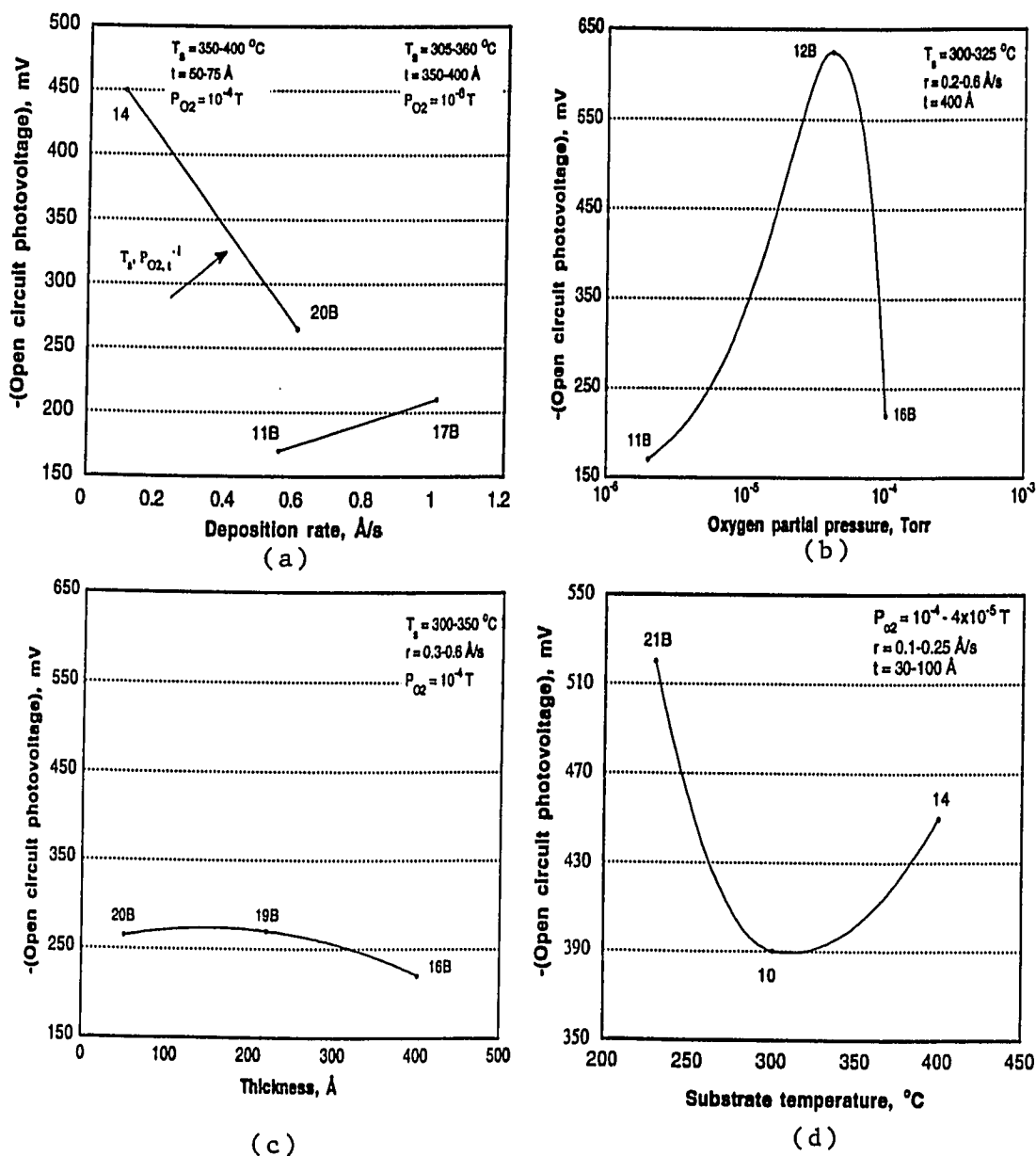


Figure 5.22: Open circuit photopotentials as functions of the deposition parameters.

5.4.2 Photoactivity of the Electrodes

Figure 5.23 shows typical plots of the current-voltage (I-V) characteristics measured at the naked ($0.2\text{--}1.0\ \Omega\text{cm}$) n-Si(111)-electrolyte interface at $0.5\ \text{M}\ \text{H}_2\text{SO}_4$ concentration. In the anodic region and under illumination, the current increases with the applied potential, reaches a maximum, and decreases at higher electrode potentials, increases again after a minimum and saturates at a certain current density. Sweeping across the potential range in the other direction (anodic to cathodic), the "current peak"

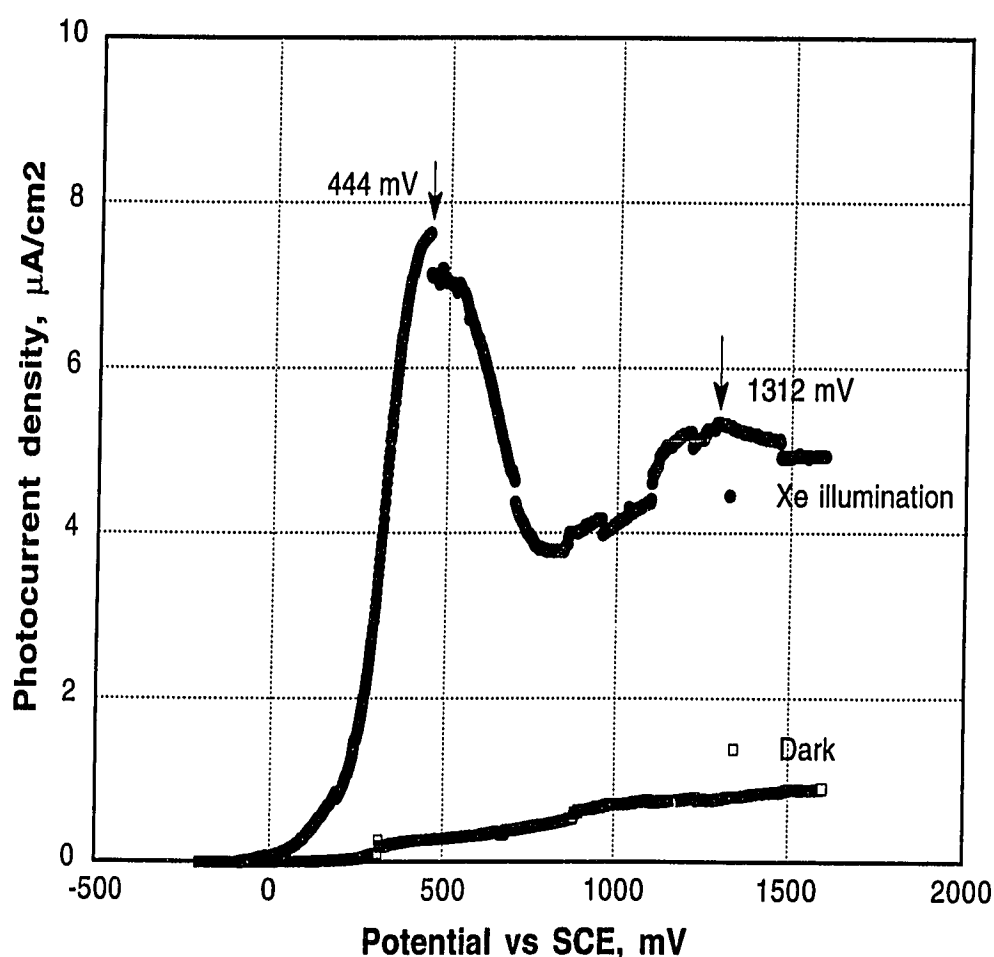


Figure 5.23: Current density vs electrode potential for an n-type "naked" silicon electrode in $1\ \text{N}\ \text{H}_2\text{SO}_4$ electrolyte.

does not show up at 5 mV/s scan rate. This anodic behavior is similar to the one reported for p-Si (1 Ω cm) electrodes in less than 1 N HF concentrations. Memming et al. [47] report that the reason for the increasing and decreasing current densities with potential is the dissolution of silicon in divalent and tetravalent states, respectively. H_2 evolves only during the increasing current step.

It is also clear that under dark conditions the current is negligible (about twenty five (25) times lower at the current peak as shown in Figure 5.22) compared to the current under illumination. Under Xe-lamp illumination, the onset of the anodic current occurs at -82 mV in 1 N H_2SO_4 solution. The photocurrents, as well as the photopotentials (see Figure 5.19) indicate that photoexcited charge carriers are produced in addition to the ions present under dark conditions.

All the cyclic I-V measurements were started at the corrosion potential reach point of each sample under radiation and the electrodes were polarized anodically. It should be noted that no pitting would be observed if the experiments were terminated before the onset of the passive region. Figures 5.24 and 5.25 show the I-V behavior of p-type silicon electrodes under two different illuminations: Xe lamp light (monochromated at 500 nm) and He-Ne laser (632.8 nm), respectively. In Figure 5.24, electrodes B and 5 differ mainly in their surface oxide film thicknesses, 740 and 50 Å oxide film/p-Si, respectively and their deposition temperatures 700 and 350 °C, respectively. The current from electrode B is almost negligible even at 3 V and this is likely due to the thick oxide layer and the formation of an Al-Si eutectic alloy at the interface due to the high substrate temperatures. Sample 5 behaves more like bare silicon.

Figure 5.25 compares the behavior from the samples 1, 2, 4 under 632.8 nm illumination. Samples 1 and 2 behave almost identical and similar to sample 5. However, the onset of the anodic current from sample 4 occurs at a higher photopotential and

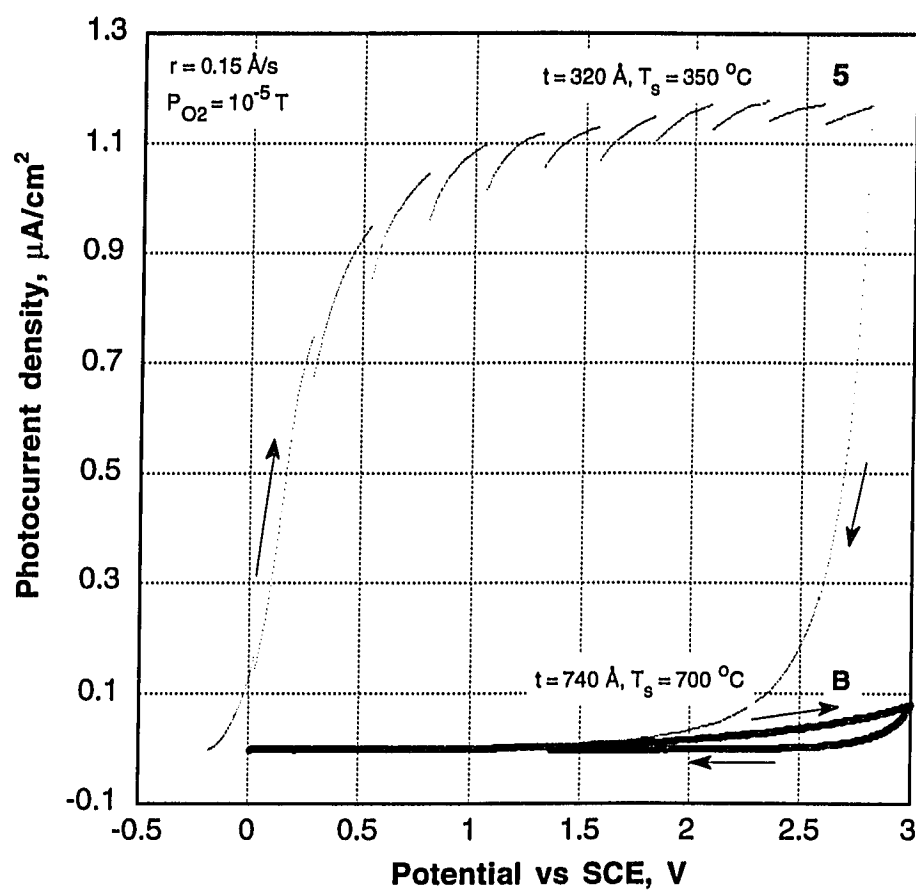


Figure 5.24: The comparison of the photocurrent-voltage behavior of p-type electrodes under Xe illumination.

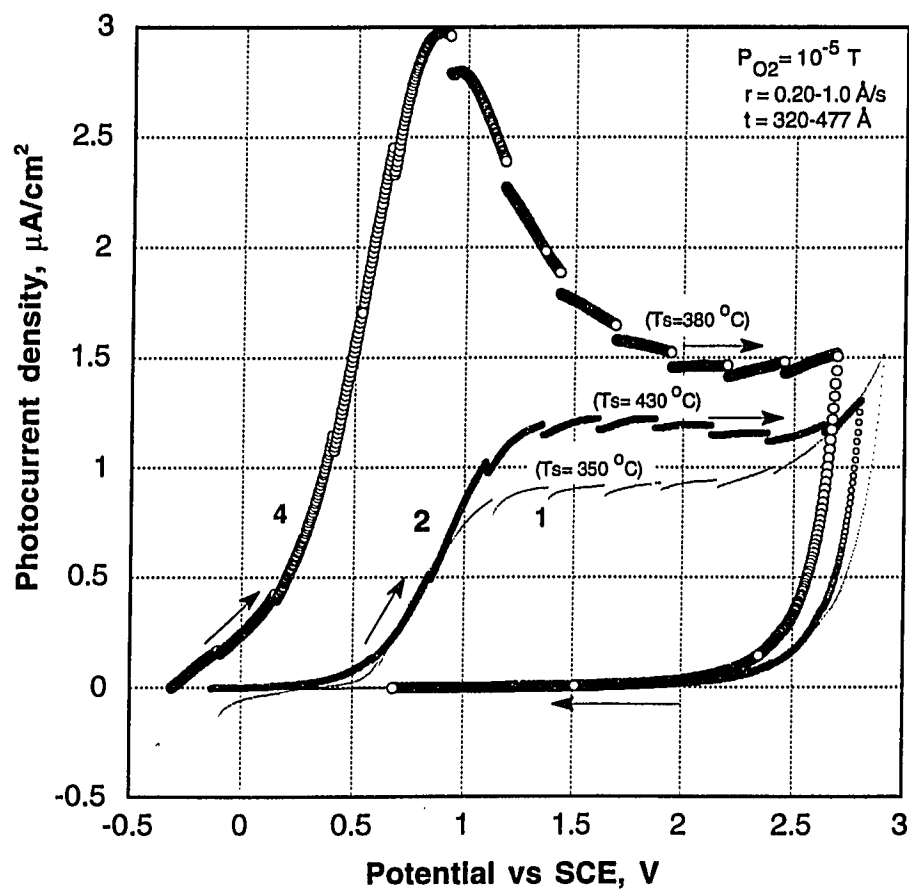


Figure 5.25: The photocurrent-voltage behavior of p-type electrodes under 632.8 nm illumination.

the coated electrode is more sensitive to visible light than naked p-Si(100) itself. Even though sample 1 and sample 4 had the same thicknesses, sample 4 was deposited at a higher temperature and its surface color differed from that of sample 1. Therefore the higher the deposition temperature the higher the photocurrent (Figure 5.22a and d) as explained by the higher amount of band bending in silicon.

Figure 5.26 through Figure 5.27 compare the I-V behavior of n-type samples 15, 16B, 17B, 19B and 20B (specified in Table 5.3) with that of an uncoated n-Si(111) electrode. Figure 5.26 compares a sample, namely 15, made at a high oxygen pressure (0.3 Torr) and deposition rate (2.5 \AA/s). Therefore on the silicon surface, there is a silicon oxide film which forms after 20 \AA Al deposition and is a better insulator than aluminum oxide. This might explain its photosensitivity being the highest of all samples. However even at 2.5 V potential application, there is no appreciable amount of photocurrent. Also the dark brown surface film remained intact after the application of potential and there was no obvious oxide dissolution on the surface. Figure 5.27 for samples 16B, 17B, 19B, 20B.

Figure 5.27 shows the potential dependence of the photocurrent for aluminum oxide films grown to different thicknesses. As shown, the electrodes need to be biased for the current to flow in the oxide film. With the application of potential, CB and VB in the semiconductor could be lowered with respect to the redox potential of the ions in the solution and then the holes can tunnel from the semiconductor surface (VB level) through the oxide to the solution (or the electrons can tunnel from the solution through the oxide into the CB of Si). The photocurrent increases with increasing film thickness up to some point and then starts decreasing, as illustrated in Figure 5.28. An explanation might be given, considering that the film thickness at the maximum corresponds to the diffusion length of the minority carriers. For thin films, all holes

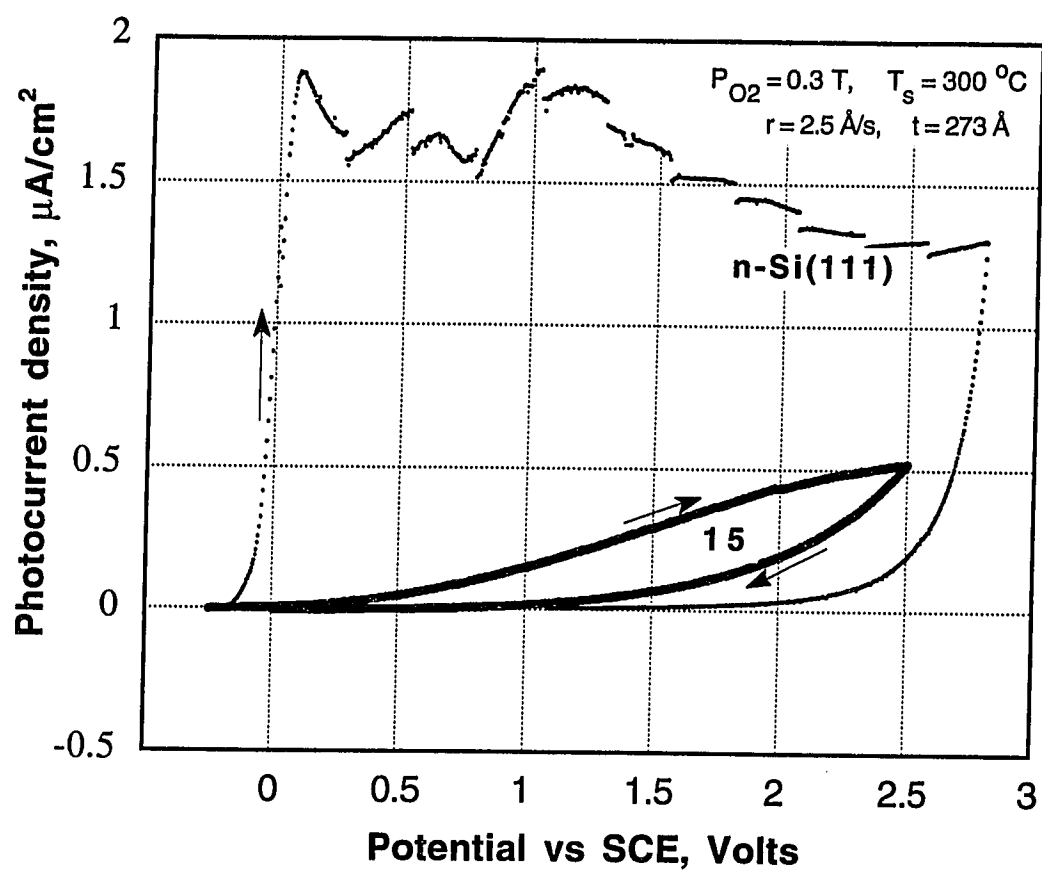


Figure 5.26: The effect of high oxygen pressure on the I-V behavior.

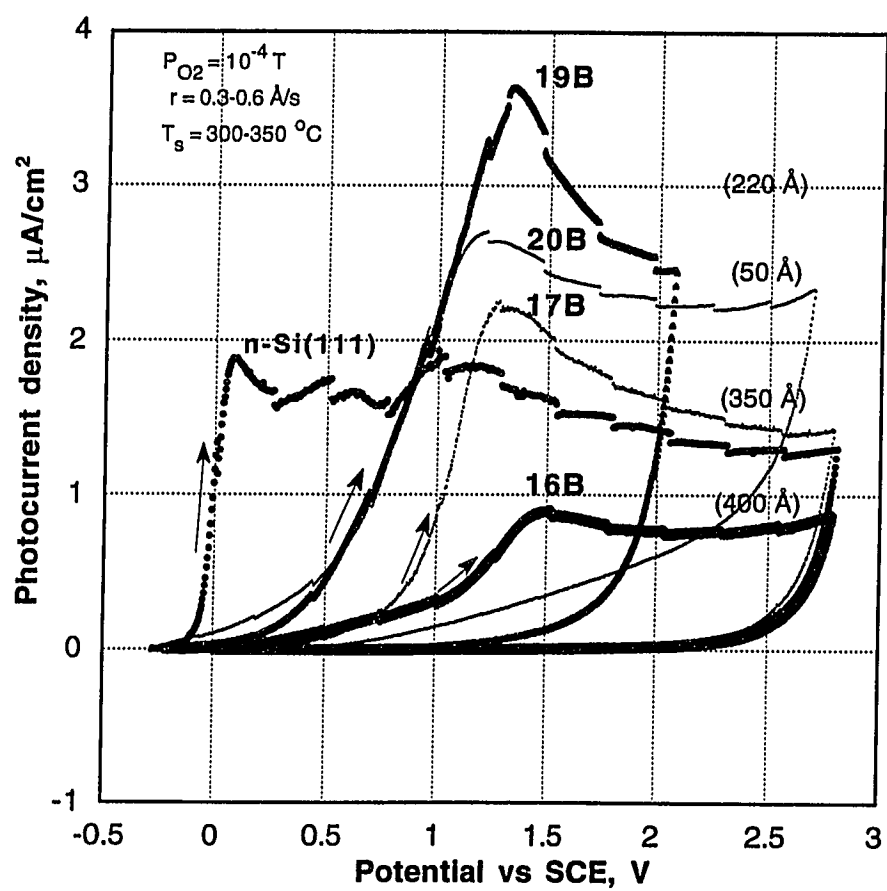


Figure 5.27: The effect of film thickness on the I-V behavior.

formed under illumination reach the surface. For thicker films, on the other hand, some holes do not reach the surface. They can, however, contribute to decrease the band bending and consequently, the measured photocurrent.

As it was seen earlier, XPS confirmed that Al is in its oxidized states in 17B and 20B. Samples 16B and 20B have continuous films on the surface as revealed by SEM. 19B and 17B had blue film on the as-deposited surface and 16B and 20B had a yellowish-green appearance. The films on 19B and 20B have higher onset photopotentials than Si (-0.25 V for the electrodes as compared to -0.18 V for naked Si). Also, all four (4) samples shown have higher photosensitivity than bare silicon.

In Figure 5.27, the maximum current peak potentials are between 1.2 - 1.5 V and at least eleven (11) times higher than uncoated Si. The formation of insulating products on the electrode surfaces prevent further increase in photocurrent and a rather flat wave is seen at increasing potentials. The photocurrents tend to saturate at $2.5 \mu\text{m}/\text{cm}^2$ for potentials anodic of 2 volts in 1 N H_2SO_4 for samples 19B and 20B. However the saturation current is about three (3) times less for sample 16B, around $0.8 \mu\text{m}/\text{cm}^2$. This current is also lower than the value for uncoated Si. The lower saturation current for sample 16B can not be attributed to absorption by the Al-oxide film on its surface, as the transmittance of the same composition film deposited on a quartz slide shows that the intensity of the light decreases by at most 30 % upon passing through the film. Therefore it seems that the main decrease in photocurrent is due to the presence of the interface states at the Al-oxide/Si interface or surface states at the oxide/electrolyte interface, which act as recombination centers and therefore reduce the photocurrent. Also the presence of the surface effects is confirmed by the decrease in the peak definition of 16B as compared to 19B. The presence of recombination centers may also explain the occurrence of a maximum in I-V plots.

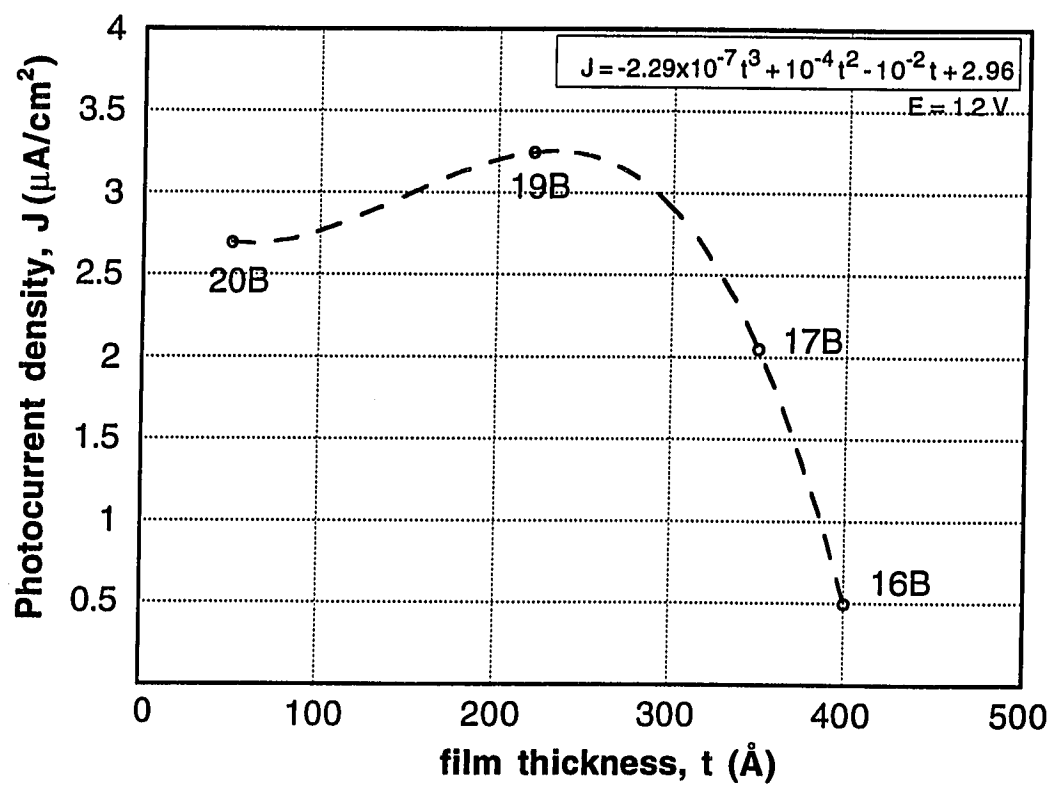


Figure 5.28: Photocurrent as a function of Al- oxide film thickness for n-type photoelectrodes.

The concentration of recombination centers increases with film thickness. This could also explain the decrease in photocurrents for thick films.

During the passage of anodic current through the electrode-electrolyte interface, color changes were observed on the electrode surface as the electrodes were polarized. This might be explained by the dissolution of the surface film and then the formation of silicon oxide on the surface as the applied potential reaches a value higher than the peak potential. Figure 5.29 shows the Si(2p) XPS spectrum of sample 12B after it was cycled up to 1 V in 1 N H_2SO_4 . The peak studied by 150 eV synchrotron radiation is at 104.5 eV and represents an oxidation state of silicon. Also SEM micrograph on the corroded surface shows some cracks on the oxide film.

The anions of SO_4 absorbed on particular surface locations may produce soluble complexes with the Al ions from the oxide and local thinning is then possible when these species leave the surface oxide. With the formation of the pits, the high electrical field strength accelerates dissolution of the film and leads to locally high current densities inside the pits. As the pit gets deeper, the solution reaches the substrate and Si oxide formation starts and the current density begins to decrease.

5.4.3 Long Term Stability of the Electrodes

The stability of the electrodes under the PEC conditions described is an important aspect for an efficient system. For this reason, the stability of the photocurrents under a potentiostatic condition should be observed. At the time there are no I-t curves available from the samples shown in Figure 5.27 as this requires more samples to be processed. The photocurrent stability of the electrodes should be studied at a potential smaller than their peak potentials (e.g. at 1.1 V). However, the stability behavior of electrode 19B at 2.5 V is illustrated in Figure 5.30 for an example. Its performance is compared to the bare n-Si. Here the current is measured when the electrode was

suddenly polarized to the potential in the passive region. The exponential decrease in the total current with time is characteristic of oxide growth [71] as observed by XPS.

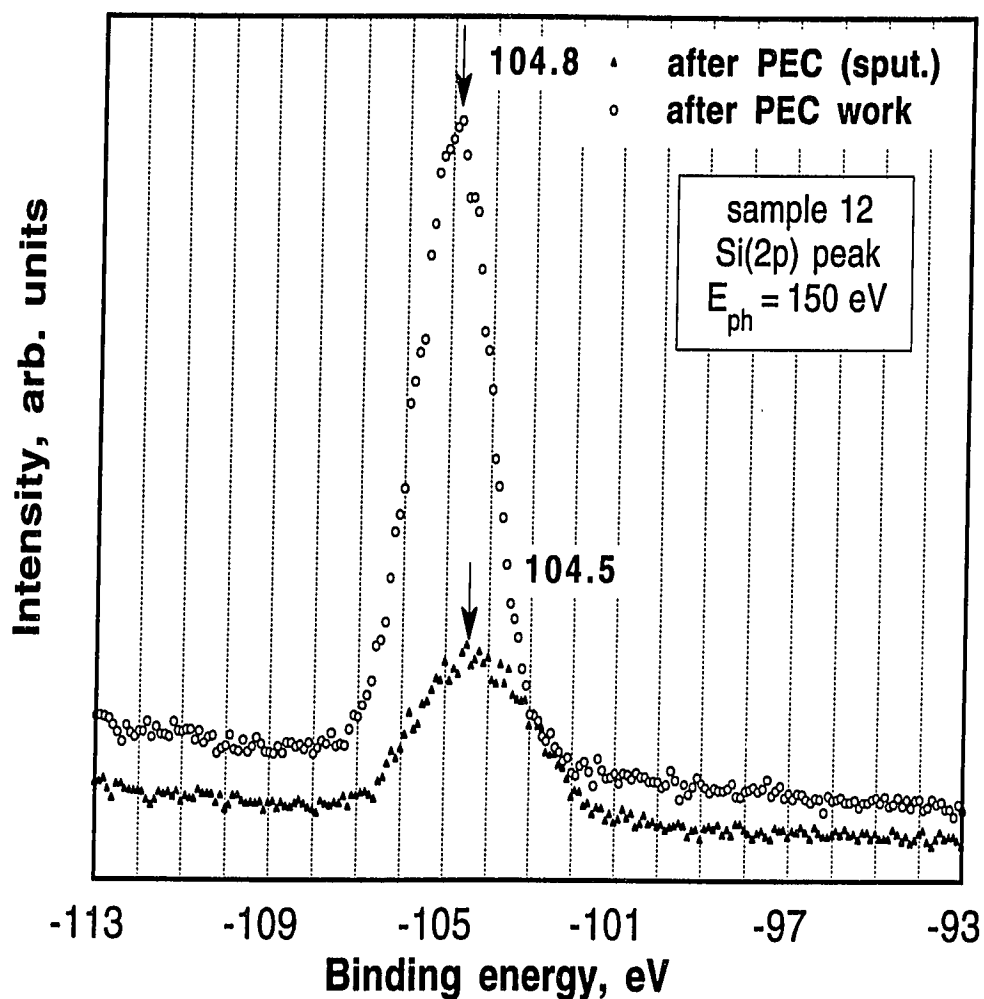


Figure 5.29: Narrow scan spectrum after a cyclic voltammogram of 1 V limit.

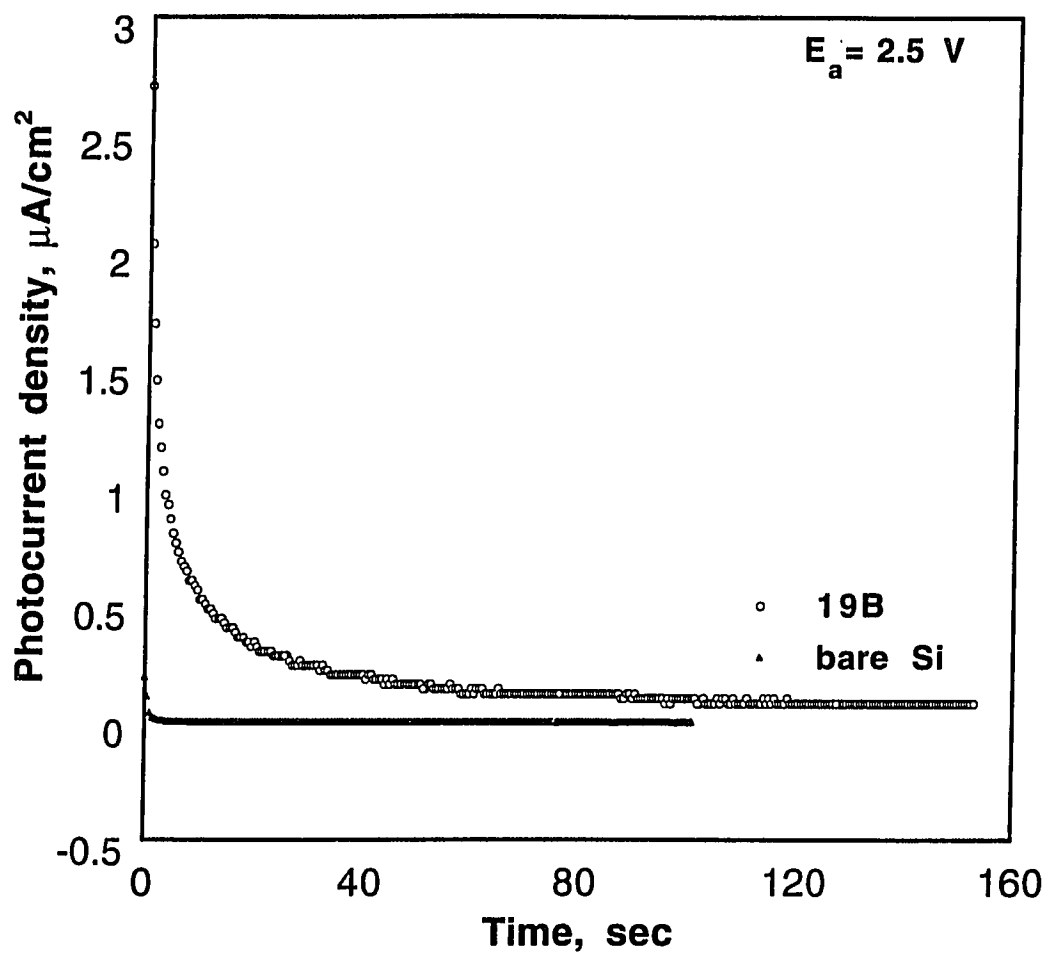


Figure 5.30: Potentiostatic oxidation photocurrent decay curve.

5.5 Summary of the Results

The photoelectrolysis of water is of potential importance as a one-step process for utilizing solar energy to produce gaseous hydrogen as a fuel. The development process for a PEC cell was shown to involve both theoretical steps and empirical experimentation. A deeper study on the optical transmittance, stoichiometry and photo-stability of the coatings requires processing more samples to be able to conclude on the optimum conditions for the production of "protective" films. However, the results suggest which material parameters need to be controlled in order to improve efficiency and stability.

In the reactive evaporation process, Al was vaporized at a rate of 0.1-2.5 Å/sec in O_2 atmosphere (6×10^{-7} - 1×10^{-4} Torr) with the typical substrate temperatures of 220-400 °C until the desired thickness 50-400 Å was obtained. High oxygen pressures and substrate temperatures were avoided since these help in forming a thick oxide layer on silicon substrate and an Al-Si alloy at the interface, respectively. No cracks were observed on these samples even at high SEM magnifications.

The oxide films deposited by ultra high vacuum (UHV) reactive evaporation technique possessed 70 - 90% transmittance in the UV-visible light range (190-800 nm). The optical transmittance (τ) and the negative of the open-circuit photopotentials ($-V_{oc}$) were found to depend on the film deposition variables. They both showed a minimum at around 0.6 Å/s deposition rate (0.0 - 1.0 Å/s range). τ and $-V_{oc}$ both increased with the oxygen partial pressure (10^{-5} - 10^{-6} range) in the deposition chamber during the deposition and both decreased with the film thickness in the 0 - 400 Å range. The transmittance increased and $-V_{oc}$ decreased with the substrate temperature in 55 - 300 °C range.

The films appeared to grow on single crystal Si wafers from initially oriented islands and clusters, to a coalesced film as the atomic coverage increased.

The surface compositions and depth profiles showed clean and uniform films. It was found that the oxide films can improve the open-circuit photovoltage of silicon and also act as anti-reflection (AR) coatings on Si. By doing extensive XPS measurements, the relationship between the photovoltage (which is affected by the intensity of the illumination) and the film stoichiometry may be obtained.

In general, the onset of the anodic current from the coated electrodes started at a higher photopotential in the cathodic direction and the oxide film was more sensitive to visible light than naked p-Si(100). For the I-V measurements, it should be noted that no pitting would be observed if the experiments were terminated before the onset of the passive region. For naked silicon, an anodic behavior similar to the one reported by Memming et al. [47] for p-Si ($1\ \Omega\text{cm}$) electrodes in less than 1 N HF concentrations was observed, where the change in photocurrent was explained by the dissolution of silicon in different oxidation states. During the PEC measurements, stability and reproducibility in open-circuit potentials were achieved only when surface cleaning procedures, Ar bubbling, sample immersion time were tightly controlled.

The photocurrent in the cell was obtained by quantum tunneling as it increased with the applied potential. It had a maximum at around 1.2 V (eleven times higher than uncoated Si). The external bias required, however, can be reduced by depositing thin layers of electrocatalysts on the electrode surface [12]. The photocurrent increased with increasing film thickness up to around 250 Å and then decreased due to the increase in the diffusion length of the minority carriers. It seems that the main reason for the decrease in photocurrent density is the presence of the interface or surface states which act as recombination centers. Therefore the achievable operating currents can be increased by preventing recombination losses at the interfaces. During the passage of anodic current through the electrode-electrolyte interface as the elec-

trodes were polarized further than the peak potential, color changes were observed on the electrode surface as the surface film dissolved.

The stability of the electrodes under the PEC conditions described is an important aspect for an efficient system. Although the total current decreased with time as observed for only 3 minutes at a passive potential region, the electrode was observed to serve better than Si. However, the stability at the semiconductor-electrolyte interface needs to be evaluated at a voltage lower than the current peak.

The accuracy and reproducibility of the current measurements are expected to improve significantly with the use of larger active electrode surface areas. It is hoped that more work on the optimization of the electrode properties may aid for future practical applications.

Chapter 6

Conclusions

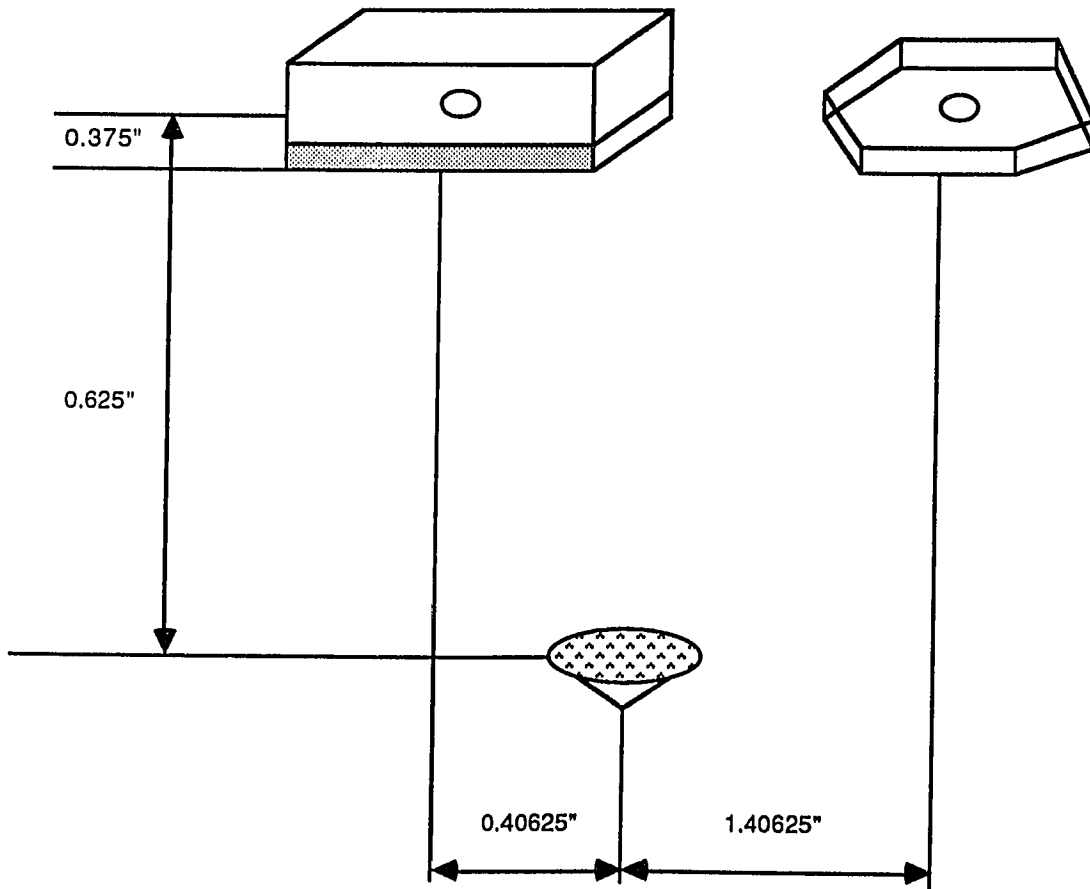
1. The development process for a PEC cell involves both theoretical steps and empirical experimentation.
2. The oxide films deposited by ultra high vacuum (UHV) reactive evaporation technique possessed 70 - 90% transmittance in the UV-visible light range (190-800 nm).
3. The surface compositions and depth profiles showed clean and uniform films.
4. The films appear to grow on single crystal Si wafers from initially oriented islands and clusters, to a coalesced film as the atomic coverage increased.
5. The optical transmittance (τ) and the negative of the open-circuit photopotentials ($-V_{oc}$) were found to depend on the film deposition variables.
6. The photocurrent in the cell is obtained by quantum tunneling through the continuous oxides as it increased with the applied potential and shows a maximum around 250 Å.
7. Interface and/or surface states are present and act as recombination centers.
8. The aluminum oxide films can improve the open-circuit photovoltage of silicon and also act as anti-reflection (AR) coatings on Si.
9. A deeper study on the optical transmittance, stoichiometry and photo-stability needs to be done to conclude on the optimum conditions for the production of "protective" films.
10. The stability at the semiconductor-electrolyte interface needs to be evaluated at a voltage lower than the current peak.

11. The accuracy and reproducibility of the current measurements are expected to improve significantly with the use of larger active electrode surface areas.

Appendix A

Appendix A

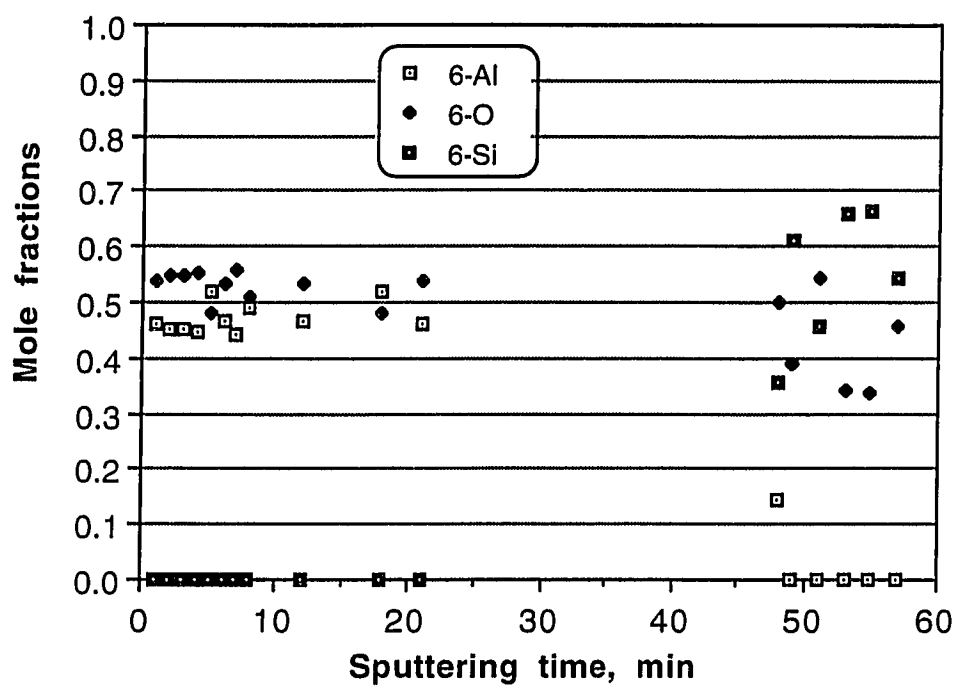
A.1 Deposition Configuration



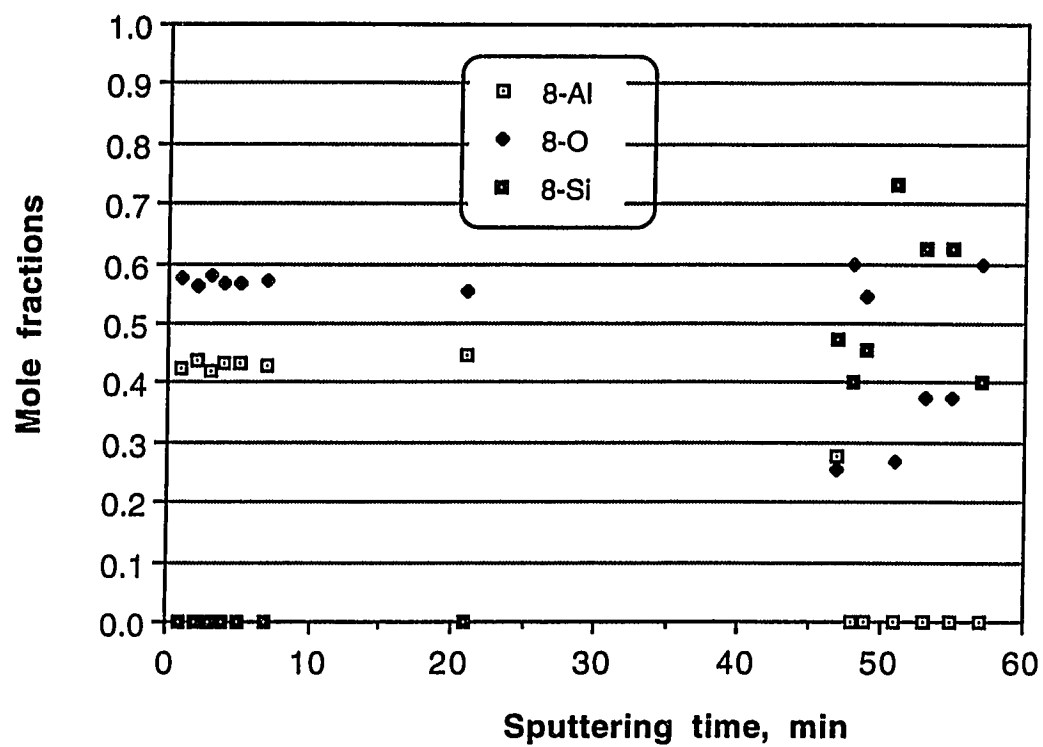
Appendix B

AES Depth Profiles

B.1 Al-oxide film on sample 6



B.2 Al-oxide film on sample 8



Bibliography

- [1] A.K. Abass, A.K. Hason, and R.H. Misho. Investigation of optically allowed transitions of α -sulphur thin films. *J. Appl. Phys.*, 58:1640, 1985.
- [2] A. Abragam. *The Principles of Nuclear Magnetism*. Oxford University Press, 1961.
- [3] G.F. Amelio. Band structure of Si by characteristic Auger electron spectrum analysis. *Surf. Sci.*, 22:301, 1970.
- [4] P.G.P. Ang and A.F. Sammels. Photoeffects on solid state photoelectrochemical cells. In A.J. Nozik, editor, *Photoeffects at Semiconductor-Electrolyte Interfaces*, *ACS Symposium Series 146*, pages 387–399. American Chemical Society, Washington, D.C., 1981.
- [5] C.R. Baker and L.C. Matsch. *Production and Distribution of Liquid Hydrogen*, volume 78, pages 37–81. Interscience, New York, 1965.
- [6] N.M. Bashara. A survey of conduction in very thin films. *IEEE Trans.*, CP-11(1):4–8, 1964.
- [7] A. Bensaoula. Molecular beam epitaxy as a growth technique for high temperature superconductors. Master's thesis, University of Houston, 1991.
- [8] I. Bergstrom and C. Nordling. *Alpha, Beta and Gamma Ray Spectroscopy*, volume 2. Amsterdam, North-Holland Pub. Co., 1965.

- [9] B.H. Billings, editor. *American Institute of Physics Handbook, second edition*. McGraw Hill Book Co. Inc., 1963.
- [10] E. Bishop and J.C. Riviere. Characteristic ionization losses observed in Auger emission spectroscopy. *Appl. Phys. Lett.*, 16:21, 1970.
- [11] J.O'M. Bockris. *Energy: The Solar-Hydrogen Alternative*. John Wiley and Sons, 1975.
- [12] J.O'M. Bockris and R.C. Kainthla. The conversion of light and water to hydrogen and electric power. *Int. J. Hyd. En.*, 13:375–383, 1988.
- [13] A.Q. Contractor and J.O'M. Bockris. Investigation of a protective conducting silica film on n-silicon. *Electrochim. Acta*, 29:1427, 1984.
- [14] R.L. Costa and P.G. Grimes. Electrolysis as a source of hydrogen and oxygen. *Chemical Engineering Progress*, 63:56–58, 1967.
- [15] D.R. Crow. *Principles and Applications of Electrochemistry*. Chapman and Hall Ltd., NY, 1982.
- [16] T.E. Daubert and R.P. Danner. *Physical and Thermodynamic Properties of Pure Chemicals, Data Compilation*, volume 1. Hemisphere Pub. Corp., NY, 1989.
- [17] L.E. Davis and et al. *Handbook of Auger Electron Spectroscopy*. Perkin Elmer Corp., 1978.
- [18] A. Despic and V.P. Parkhutić. Electrochemistry of aluminum in aqueous solutions and physics of its anodic oxide. In *Modern Aspects of Electrochemistry*, volume 20, page 450. Academic Press, 1989.
- [19] J.W. Diggle, editor. *The Anodic Behavior of Metals and Semiconductor Series*, volume 2. M. Dekker, NY, 1973.

- [20] E. Dorre and H. Hubner. *Alumina: Processing, properties and applications*. Springer-Verlag Berlin, Heidelberg, 1984.
- [21] L. Eckertova. *Physics of Thin Films*, chapter 1, 7, pages 17, 295, 300. Plenum Press, 1986.
- [22] G. Ertl and J. Kupperts. *Low Energy Electrons and Surface Chemistry*. VCH, Weinheim, 1985.
- [23] F.R.F. Fan, R.G. Keil, and A.J. Bard. Semiconducting electrodes. 48. photooxidation of halides and water on n-Si protected with silicide layers. *J. Am. Chem. Soc.*, 105:220, 1983.
- [24] L.C. Feldman and J.W. Mayer. *Fundamentals of Surface and Thin Film Analysis*. North-Holland, 1986.
- [25] J.C. Fisher and I. Giaever. Tunneling through thin insulating layers. *J. Appl. Phys.*, 32:172–177, 1961.
- [26] K.W.Jr. Frese, M.J. Madou, and S.R. Morrison. Investigation of photoelectrochemical corrosion of semiconductors. *J. Electrochem. Soc.*, 128:1939, 1981.
- [27] S. Ghosh, Á. Sarkar, S. Chaudhuri, and A.K. Pal. Optical properties of ZnO:Al films prepared by reactive dc magnetron sputtering. *Vacuum*, 42(10-11):645–648, 1991.
- [28] D.S. Ginley, M.A. Butler, and C.H. Seager. The optimization of solar conversion devices. In L.E. Murr, editor, *Solar Materials Science*, chapter 18, pages 619–664. Academic Press, 1980.
- [29] W. Grasse and F. Oster. Hysolar: Solar hydrogen energy. *Results and Achievements 1985-89*, pages 16–19, 1990.

- [30] A.J. Griffin. *Impedance Spectroscopy Response of Aluminum-Copper-Silicon Alloys*. PhD thesis, Rice University, 1991.
- [31] H.L. Hagedoorn and A.H. Wapstra. Measurements of the fluorescent yield of the k-shell with a proportional counter. *Nucl. Phys.*, 15:146, 1960.
- [32] D.E. Halverson and D.L. Cocke. Ruthenium impregnation of plasma grown alumina films. *J. Vac. Sci. Technol. A*, 7(1):40–48, 1989.
- [33] L.A. Harris. Analysis of materials by electron excited Auger electrons. *J. Appl. Phys.*, 39:1419–1428, 1968.
- [34] G. Hodes, L. Thompson, J. DuBow, and K. Rajeshwar. Heterojunction silicon/indium tin oxide photoelectrodes. *J. Am. Chem. Soc.*, 105:324–330, 1983.
- [35] L. Holland. *Vacuum Deposition of Thin Films*, chapter 4, 11, 16, pages 129, 355, 465. Chapman and Hall Ltd., 1956.
- [36] K. Honda, A. Fujishima, and T. Watanabe. Photoelectrochemical hydrogen production. In T. Ohta, editor, *Solar Hydrogen Energy Systems*, chapter 7, pages 137–170. Pergamon Press, 1979.
- [37] A.F. Janzen. Photoelectrochemistry I- photoelectrolysis. In A.E. Dixon and J.D. Leslie, editors, *Solar Energy Conversion*, chapter 30, pages 905–921. Pergamon Press, 1978.
- [38] E.W. Justi. Leitungmechanismus und energiewandlung in festkörpern. *Vandenhoeck und Ruprecht*, 1965.
- [39] R.C. Kainthla, B. Zelenay, and J.O'M. Bockris. Protection of n-Si photoanode against photocorrosion in photoelectrochemical cell for water electrolysis. *J. Electrochem. Soc.*, 133:248, 1986.

- [40] L. Kazmerski. Introduction to photovoltaics, research and device problems in photovoltaics. In L.E. Murr, editor, *Solar Materials Science*, chapter 15, 16, pages 505, 555–556. Academic Press, 1980.
 - [41] J.J. Lander. Auger peaks in the energy spectra of secondary electrons from various materials. *Phys. Rev.*, 91:1382, 1953.
 - [42] J.M. Lehn. Photoinduced generation of hydrogen and oxygen from water. In J.S. Connolly, editor, *Photochemical Conversion and Storage of Solar Energy*, chapter 6, page 186. Academic Press, NY, 1981.
 - [43] G.H. Lin, M. Kapur, R.C. Kainthla, and J.O'M. Bockris. One step method to produce hydrogen by a triple stack amorphous silicon solar cell. *Appl. Phys. Lett.*, 55:386, 1989.
 - [44] M.J. Madou, F. Cardon, and W.P. Gomes. Impedance measurements at the n- and p-type GaP single crystal electrode. *J. Electrochem. Soc.*, 124:1623, 1977.
 - [45] J.G. Mavroides, J.A. Kafalas, and D.F. Kolesar. Photoelectrolysis of water in cells with SrTiO_3 anodes- quantum efficiency measurement. *Appl. Phys. Lett.*, 128(5):pages, 1976.
 - [46] C.A. Mead. Electron transport mechanisms in thin insulating films. *Phys. Rev.*, 128(5):2088–2093, 1962.
 - [47] R. Memming and E. Schwandt. Anodic dissolution of silicon in hydrofluoric acid solutions. *Surface Science*, 4:109–124, 1966.
 - [48] D. Meyerhofer and S.A. Ochs. Current flow in very thin films of Al_2O_3 and BeO . *J. Appl. Phys.*, 34(9):2535–2543, 1963.
-

- [49] S.R. Morrison. *Electrochemistry at Semiconductor and Oxidized Metal Electrodes*. Plenum Press, 1980.
- [50] Y. Nakato and et al. A new photovoltaic effect observed for metal-coated semiconductor electrodes and its utilization for the photolysis of water. *Berichte der Bunsen-Gesellschaft*, 80(10):1002–1007, 1976.
- [51] J.A. Nesbitt, N.S. Jacobson, and R.A. Miller. Protective coatings for high temperature technology. In R. Kossowsky, editor, *Surface Modification Engineering*, volume 11, chapter 2, pages 25–66. CRC Press, 1989.
- [52] C.A. Neugebauer. Structural disorder phenomena in thin metal films. In *Physics of Thin Films*, volume 2, page 14. Academic Press, 1964.
- [53] A.J. Nozik. Electrode materials for PEC devices. *J. Crystal Growth*, 39:200–209, 1977.
- [54] J.M. Ogden and R.H. Williams. Solar hydrogen moving beyond fossil fuels. *World Resources Institute, Washington, D.C.*, 1989.
- [55] T. Osaka, E. Ejiri, and N. Hirota. Photoelectrochemical behavior of iron oxide/n-Si heterojunction electrodes with an outer Pd layer. *J. Electrochem. Soc.*, 131:1571, 1984.
- [56] E.K. Oshe and I.L. Rozenfeld. Investigation of anodic oxidation passivation of silver in basic solutions by photoelectric polarization. *Elektrokhimiya*, 7:1415, 1971.
- [57] S.R. Pollack. Schottky field emission through insulating layers. *J. Appl. Phys.*, 34(4):877–880, 1963.

- [58] K. Rajeshwar. Materials aspects of photoelectrochemical energy conversion. *J. Appl. Electrochem.*, 15:1–22, 1985.
- [59] E.H. Rhoderick. *Metal-Semiconductor Contacts*. Clarendon Press, Oxford, 1982.
- [60] Hart R.K. and J.K. Maurin. The nucleation and growth of oxide islands on aluminum. *Surf. Sci.*, 20:285–303, 1970.
- [61] K. Schroder. *Handbook of Electrical Resistivities of Binary Metallic Alloys*. CRC, 1983.
- [62] R.E. Schwerzel and K.B. Spahr. Production with photoactive catalysts stabilized by metallized plasma polymer coatings. *BATTELLE*, 1989.
- [63] K. Siegbahn and C.N. Nordling. *ESCA, Atomic, Molecular and Solid State Structure Studied by Means of Electron Spectroscopy*. Almqvist and Wiksells (Upsala, Sweden), Sweden, 1967.
- [64] J.G. Simmons. Potential barriers and emission- limited current flow between closely spaced parallel metal electrodes, 1964 and generalized formula for the electric tunnel effect between similar electrodes separated by a thin insulating film 1963. *J. Appl. Phys.*, 34, 35:1793, 2472, 1963, 1964.
- [65] J.A. Treverton, et al. SSIMS, XPS and microstructural studies of ac- phosphoric acid anodic films on aluminum. *Surface and Interface Analysis*, 15:369–376, 1990.
- [66] K.N. Tu, J.W. Mayer, and L.C. Feldman. *Electronic Thin Film Science for Electrical Engineers and Material Scientists*. Macmillan Publishing Co., 1992.
- [67] K.R. Van Horn, editor. *Aluminum*, volume 1, pages 362–363, 378. ASM, 1967.
- [68] J.L. Vossen. Transparent conducting films. In G. Hass, editor, *Physics of Thin Films*, volume 9, pages 1–71. Plenum Press, 1977.

- [69] C.D Wagner, et al., editor. *Handbook of X-Ray Photoelectron Spectroscopy*. Perkin Elmer Corp., 1979.
- [70] R.E. Weber and A.C. Johnson. Determination of surface structures using LEED and energy analysis of scattered electrons. *J. Appl. Phys.*, 40:314, 1969.
- [71] S.M Wilhelm and N. Hackerman. Photoelectrochemical characterization of the passive films on iron and nickel. *Corrosion Science*, 128(8):1668–1674, 1963.
- [72] D.P. Woodruff and T.A. Delchar. *Modern Techniques of Surface Science*. Cambridge University Press, NY, 1986.
- [73] C.R. Worthington and S.G. Tomlin. The intensity of emission of characteristic x-radiation. *Proc. Phys. Soc.*, A69:401, 1956.